

**Local- to Micro-Scale Structural Controls on Shear-Zone-Hosted  
Gold Mineralisation, Ngubevu Area, Natal Thrust Front, Tugela  
Terrane, South Africa**

By

**Onele Chagi**

**Submitted in fulfilment of the academic requirements for the degree of  
Master of Science in Geology**

**Discipline of Geology**

**School of Agricultural, Earth and Environmental Sciences**

**College of Agriculture, Engineering and Science**

**University of KwaZulu-Natal**

**Durban**

**South Africa**

**October 2021**

As the candidate's supervisors, we have approved this version of corrected thesis.

Signature:



Date: 03/01/2022

Name: Prof. E.J.M. Carranza (Supervisor)

Signature:

Date:

Name: Dr. L. Hoyer (Co-supervisor)

Countersigned by SAEES Academic Leader – Research

Signature:

Date:

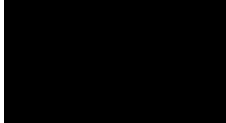
Name: Prof T R Hill, SAEES Academic Leader – Research

## PREFACE

The research work described in this dissertation was carried out in the Discipline of Geology, School of Agricultural, Earth and Environmental Sciences, University of KwaZulu-Natal, Westville, Durban, from March 2019 to September 2021, under the supervision of Professor Emmanuel John M. Carranza and co-supervision of Dr. Lauren Hoyer.

This dissertation represents original work carried out by the author and it has not been submitted in any form, for any degree or diploma to any tertiary institution. Where use has been made of the work of others it is duly acknowledged in the text and included in the reference list.

Signature:



Date: 03/01/2022

Name: Onele Chagi (Candidate)

Signature:



Date: 03/01/2022

Name: Prof. E.J.M. Carranza (Supervisor)

Signature:

Date:

Name: Dr. L. Hoyer (Co-supervisor)

## DECLARATION BY SUPERVISORS

We hereby declare that we supervised this MSc candidate:

**Full Name:** Onele Chagi

**Student Number:** 214502317

**Thesis Title:** Local- to Micro-Scale Structural Controls on Shear-Zone-Hosted Gold Mineralisation, Ngubevu Area, Natal Thrust Front, Tugela Terrane, South Africa.

There was regular consultation between the candidate and us for the duration of this research. We advised the candidate to the best of our abilities and approved the final dissertation for submission to the Higher Degrees Office of the College of Agriculture, Engineering and Science for examination by university appointed examiners.

Signature:



Date: 03/01/2022

Name: Prof. E.J.M. Carranza (Supervisor)

Signature:

Date:

Name: Dr. L. Hoyer (Co-supervisor)

## DECLARATION 1 – PLAGIARISM

I, Onele Chagi, declare that:

1. The research reported in this dissertation, except where otherwise indicated and acknowledged, is my original research.
2. This dissertation has not been submitted for any degree or examination at any other university.
3. This dissertation does not contain other persons' data, pictures, graphs, or other information, unless specifically acknowledged as being sourced from other persons.
4. This dissertation does not contain other persons' writing, unless specifically acknowledged as being sourced from other researchers. Where other written sources have been quoted, then:
  - a. Their words have been re-written, but the general information attributed to them has been referenced.
  - b. Where their exact words have been used, their writing has been italicised inside quotation marks and suitably referenced.
5. This dissertation does not contain text, graphics or tables copied and pasted from the internet, unless specifically acknowledged, and the source being detailed in the text and in the references section.

Signature:

A solid black rectangular box used to redact the signature of the author.

Date: 03/01/2022

Name: Onele Chagi

## ABSTRACT

The research described in this dissertation focused on shear-zone-hosted precious and base metal mineralisation in the Ngubevu area, in the Natal Thrust Front of the Tugela Terrane in the Natal Metamorphic Province of South Africa. This province forms part of a 400-km-wide metamorphic belt referred to as the Namaqua-Natal Metamorphic Province, which stretches from the Northern Cape on the west coast to KwaZulu-Natal on the east coast of the country. Unlike the western Namaqualand Metamorphic Province, which is well-explored and well-exploited for several mineral deposits, the Natal Metamorphic Province is relatively poorly explored. One reason for this is that the nature of structural controls on mineralisation in the Natal Metamorphic Province is poorly understood. In the research described in this dissertation, known occurrences of shear-zone-hosted precious and base metal deposits in the Golden Eagle and Champion Mines in the Ngubevu area, which have been described in the literature, were studied in the micro-scale, and the findings obtained were integrated with existing knowledge of regional- to local-scale deformation in the Tugela Terrane, in order to deduce the structural controls of such mineralisation in the area. The micro-scale data, studied by spatial analytical methods (i.e., point pattern analysis, Fry analysis, fractal analysis and shape analysis) show that the mineralisation in the area operated in at least two spatial scales, within each thin section sample, of at most  $0.005\ \mu\text{m}$  and at least  $0.002\ \mu\text{m}$  and that, within each thin section sample, the occurrence of shear-zone-hosted precious and base metal deposits is non-random as they exhibit clustered and/or regular spatial distributions. Micro-fractures in the area generally show major northerly trends in their alignments. Likewise, micro-scale mineral distributions show NNE–SSW and NNW–SSE trends in their orientations. These findings suggest that N–NE-directed compression controlled the occurrence and distribution of shear-zone-hosted precious and base metal mineralisation in the Ngubevu area. This N–NE-directed compression and thrusting during deformation ( $D_1$ ) controlled the circulation and concentration of mineralising hydrothermal fluids in the Natal Thrust Front. These hydrothermal fluids formed quartz veins along nearly E–W-trending foliations resulting in mineralisation in the clustered and regular spatial patterns observed in the micro-scale.

## ACKNOWLEDGEMENTS

Nothing is possible in this world without God, and I just want to thank Him for keeping me this far and allowing me to see this research project to completion. I also want to thank my ancestors, my guides, who walk with me and have walked the way before me. Thank you for being a beaming light of hope in my life as I continue to navigate the world.

This research project is the culmination of a lot of hard work, not just by me but with the assistance, guidance, and motivation of others. And I would like to thank everyone involved in its completion.

To my supervisor, Prof. John Carranza, I want to thank you for your guidance and support throughout. You have helped me to become a better scientist and writer by always questioning me in ways that made me improve the quality of the work and always encouraging me to think about how I write and how I want to phrase my interpretations of the data. I also want to thank you for your kindness and generosity. This project would not have been complete without you.

To my co-supervisor, Dr. Lauren Hoyer, thank you for your suggestions and edits, which helped to improve the work described and presented in this dissertation not just technically but also stylistically. Dr. Hoyer and Mr. Philani Mavimbela, who has sadly left the university to pursue greener pastures, put my name forward for this research when Prof. Carranza was looking for students and I would like to express my gratitude to them for that.

I would also like to thank the field guides, who so graciously showed us around the mining sites during field work in Ngubevu in 2019. And to the people of Ngubevu, for welcoming us into their neighbourhood and sometimes allowing us to cross through their yards to get to some of the sampling locations.

This research benefitted financial support from the National Research Foundation (NRF) in the form of grantholder-linked student support to Prof. Carranza (NRF Grant No. 116311). Therefore, the financial assistance of the NRF towards this research is hereby acknowledged. The opinions expressed and conclusions arrived at in this dissertation, are those of the author and are not necessarily to be attributed to the NRF.

To my office mates, Sino and Jamie, and friends in the department, thank you for everything. The laughter and joy kept me sane during the course of this research and will stay with me forever.

Lastly, I want to thank my family for their support. Especially my mother, Sizani, who has always supported me in everything I do and encouraged me to pursue my dreams even in times when she did not understand them. Thank you for everything. I love you.

<b>TABLE OF CONTENTS</b>	<b>PAGE</b>
PREFACE	i
DECLARATION BY SUPERVISORS	ii
DECLARATION 1 – PLAGIARISM	iii
ABSTRACT	iv
ACKNOWLEDGEMENTS	v
LIST OF FIGURES	x
LIST OF TABLES	xv
CHAPTER 1: INTRODUCTION	1
1.1. BACKGROUND	1
1.2. RESEARCH AIMS AND OBJECTIVES	3
CHAPTER 2: LITERATURE REVIEW	5
2.1. REGIONAL GEOLOGY	5
2.2. TUGELA TERRANE	8
2.2.1. NATAL NAPPE COMPLEX	10
2.2.2. NATAL THRUST FRONT	12
2.2.2.1. <i>Ngubevu Area</i>	14
2.2.2.2. <i>Mfongosi Area</i>	15
2.2.2.3. <i>Manyane Thrust</i>	15
2.3. LOCAL GEOLOGY	16
2.3.1. GEOLOGY	17
2.3.2. STRUCTURE AND DEFORMATION	18
2.4. MINERALISATION	22
2.4.1. <i>Ngubevu Area</i>	23
2.5. CONCLUDING REMARKS	24
CHAPTER 3: RESEARCH METHODOLOGY	25
3.1. LOCAL-SCALE DATABASE COMPILATION	25
3.2. SAMPLE COLLECTION AND LABORATORY PREPARATION	25
3.3. MICRO-SCALE MAPPING OF FRACTURES AND ORE MINERAL CENTROIDS	28
3.4. DIGITISATION OF MICRO-FRACTURES AND ORE MINERALS	29
3.5. SPATIAL ANALYSES	31

3.5.1. <i>Point Pattern Analysis</i>	31
3.5.2. <i>Fry Analysis</i>	31
3.5.3. <i>Fractal Analysis</i>	32
3.5.4. <i>Shape Analysis</i>	33
<b>3.6. CONCLUDING REMARKS</b>	<b>34</b>
<b>CHAPTER 4: ANALYSIS OF MICRO-FRACTURES</b>	<b>37</b>
<b>4.1. RESULTS</b>	<b>38</b>
4.1.1. <i>Golden Eagle</i>	38
4.1.2. <i>Champion Mine</i>	41
<b>4.2. DISCUSSION AND CONCLUSION</b>	<b>43</b>
<b>CHAPTER 5: POINT PATTERN ANALYSIS OF MICRO-SCALE MINERAL DISTRIBUTION</b>	<b>47</b>
<b>5.1. RESULTS</b>	<b>49</b>
5.1.1. <i>Golden Eagle</i>	49
5.1.2. <i>Champion Mine</i>	51
<b>5.2. DISCUSSION AND CONCLUSION</b>	<b>52</b>
<b>CHAPTER 6: FRY ANALYSIS OF MICRO-SCALE MINERAL DISTRIBUTION</b>	<b>55</b>
<b>6.1. RESULTS</b>	<b>57</b>
6.1.1. <i>Golden Eagle</i>	57
6.1.2. <i>Champion Mine</i>	59
<b>6.2. DISCUSSION AND CONCLUSION</b>	<b>60</b>
<b>CHAPTER 7: FRACTAL ANALYSIS OF MICRO-SCALE MINERAL DISTRIBUTION</b>	<b>61</b>
<b>7.1. BOX-COUNTING FRACTAL DIMENSION</b>	<b>61</b>
<b>7.2. RESULTS</b>	<b>62</b>
7.2.1. <i>Golden Eagle</i>	63
7.2.2. <i>Champion Mine</i>	64
<b>7.3. DISCUSSION AND CONCLUSION</b>	<b>66</b>
<b>CHAPTER 8: SHAPE ANALYSIS OF MICRO-SCALE MINERAL DISTRIBUTION</b>	<b>67</b>
<b>8.1. RESULTS</b>	<b>68</b>
8.1.1. <i>Golden Eagle</i>	68
8.1.2. <i>Champion Mine</i>	68
<b>8.2. DISCUSSION AND CONCLUSION</b>	<b>72</b>

<b>CHAPTER 9: DISCUSSION</b>	<b>73</b>
<b>9.1. MICRO-SCALE STUDY OF MINERAL DEPOSIT DISTRIBUTION</b>	<b>73</b>
<b>9.2. MICRO- TO LOCAL-SCALE STRUCTURAL CONTROLS ON PRECIOUS AND BASE METAL MINERALISATION IN THE NGUBEVU AREA</b>	<b>74</b>
<b>9.3. SHORTCOMINGS OF THIS RESEARCH</b>	<b>77</b>
<b>9.4. DELINEATING POTENTIAL EXPLORATION TARGETS</b>	<b>78</b>
<b>CHAPTER 10: CONCLUSIONS AND RECOMMENDATIONS</b>	<b>79</b>
<b>10.1. CONCLUSIONS</b>	<b>79</b>
<b>10.2. RECOMMENDATIONS</b>	<b>80</b>
<b>REFERENCES</b>	<b>83</b>
<b>APPENDIX A: SPATIAL DISTRIBUTION OF CENTROIDS OF SPHALERITE GRAINS IN THIN SECTIONS OF SAMPLES FROM THE STUDY AREA</b>	<b>93</b>
<b>APPENDIX B: SPATIAL DISTRIBUTION OF FRY POINTS PLOTTED FOR THIN SECTIONS OF SAMPLES FROM THE STUDY AREA</b>	<b>95</b>
<b>APPENDIX C: ORIENTED PHOTOMICROGRAPHS OF THIN SECTIONS OF SAMPLES FROM THE STUDY AREA</b>	<b>97</b>
<b>APPENDIX D: BINARY IMAGES OF SPHALERITE GRAINS IN ORIENTED THIN SECTIONS OF SAMPLES FROM THE STUDY AREA FITTED WITH BEST-FIT ELLIPSES</b>	<b>101</b>

## LIST OF FIGURES

*Figure 2.1: Geology and distribution of terranes and lithologies of the Natal Metamorphic Province (modified after Sharib et al. (2021)). The extent of the Namaqua-Natal Metamorphic Province beneath rocks of the Karoo Supergroup is indicated by the inset map. Also shown is the Namaqua Province on the west coast. GB = Gariiep Belt and KB = Kheis Belt. The Ngubevu area is indicated by the rectangular box along the Natal Thrust Front. The approximate location of the Ngubevu area is indicated by a star on the Natal Thrust Front; more precise location is indicated in Figures 2.3 and 2.4.*

*Figure 2.2: Idealised S-N cross-section along the Natal Metamorphic Province indicating the three tectonostratigraphic terranes and their related structures (modified from Mendonidis and Thomas, 2019).*

*Figure 2.3: Geological map of the Tugela Terrane indicating the Nappe Complex/Zone and related intrusions and the Ntingwe and Mfongosi Groups of the Natal Thrust Front (modified from McCourt et al. (2006)). The Ngubevu area is indicated by the rectangular box in the NW quadrant of the map.*

*Figure 2.4: Geology and distribution of rocks of the Natal Thrust Front (modified from Basson and Watkeys (2003)). The rectangular box denotes the study area, which continues towards the left out of this map*

*Figure 2.5: S–N cross-section along the western end of the Tugela Terrane, indicating the relationship between rocks of the Natal Nappe Complex (Tugela Nappe) and the Natal Thrust Front (modified from Basson et al., 2005).*

*Figure 2.6: Map showing the geology of the Ngubevu area (modified from Basson, 2000). Locations at/around the Golden Eagle and Champion Mines in the western portion of the Ngubevu area were the focus of this study.*

*Figure 2.7: Lithological map of the Ngubevu West Area (modified from Basson, 2000), displaying the locations of mines according to local guides and to regional Geological Map Sheet 2830DA of Collessie. Abbreviations: qtz – quartz, ab – albite, tour – tourmaline, kfs – K-Feldspar.*

*Figure 2.8: Equal area stereonet plots of  $S_1$  planar foliations in the Ngubevu West Area for (A) Golden Eagle Mine area, (B) Champion Mine area, (C)  $V_1$  veins in the Golden Eagle mine area and (D)  $V_1$  veins in the*

*Champion Mine area. These data were digitised from maps in Basson (2000). The beta planes in (A) and (B) represent foliation planes while the crosses represent poles to the foliation planes. The beta planes in (C) and (D) represent veins while the crosses represent poles to the veins.*

*Figure 3.1: Oriented samples measured from an outcrop before extraction. Measurements of planar surface attitudes are marked on (A) top foliation surface and (B) bottom foliation surface.*

*Figure 3.2: Procedure for reorienting a sample in the laboratory. (A) A sample is placed in a sandbox filled with fine beach sand. (B) The sample is oriented to its original dip. (C) The sand surface is ensured to be horizontal, and a rubber band is wrapped around the sample parallel to the horizontal sand surface; this marks the line of zero dip. (D) A line following the rubber band is marked with an indelible marker to prevent it from being washed away to the cutting process.*

*Figure 3.3: Rock chips permanently oriented and prepared for thin sectioning. (A) Top surface of the thin section and (B) mounting/cut surface of the thin section.*

*Figure 3.4: The Georeference editing window in ILWIS 3.3 showing the northing and easting coordinates of (A) sample CM-15B with micro-fractures and (B) sample CM-15B with ore mineral centroids.*

*Figure 3.5: The workflow procedure for obtaining the trends in the shapes of ore minerals. (A) Original image captured with a camera attached to a Leica microscope under reflected light. (B) Binary image of ore minerals (sphalerite) in the image obtained using ImageJ. (C) Ellipses fitted automatically to selected ore minerals in EllipseFit. Only minerals with unequal axes were selected and fitted with ellipses as equal sided shapes would produce circles. (D) Rose diagram plotted with GeoRose for trends of major axes of ellipses fitted to ore mineral shapes. All the images above are from sample CM-04.*

*Figure 4.1: Equal area stereonet plots of deposit-scale field structural measurements collected at (A) Golden Eagle Mine area and prospect site and (B) Champion Mine area and prospect site. The beta planes represent foliations and crosses represent poles to the foliation.*

*Figure 5.1: The three principal types of spatial point pattern occurrences; random, clustered, and regular (modified from Carranza, 2009). The unknown pattern represents centroids of sphalerite grains in thin section of sample CM-15B of this research.*

Figure 6.1: Schematic diagram illustrating the procedure for the construction of a Fry plot (modified from Sun et al., 2018). (A) Original point pattern. (B) One of the points in the original pattern is used as the diagram centre/origin. (C) Fry distribution according to points in (B). (D) and (E) Other points are selected and used as the diagram centre. (F) Fry distribution according to points in (B), (D), and (E). (G) Fry plot obtained when all points in (A) have been used as the diagram centre. For the translations shown in the above diagram, “C” indicates the points used as the diagram centre.

Figure 6.2: Trends of Fry points of centroids of sphalerite grains in oriented thin sections of samples collected from the Golden Eagle Mine area and prospect site. (a) GE-01, (b) G-E02, (c) GE-04, (d) GE-09, (e) GE-10.

Figure 6.3: Trends of Fry points of centroids of sphalerite grains in oriented thin sections of samples collected from the Champion Mine area and prospect site. (a) CM-15B, (b) CM-19, (c) CM-24.

Figure 7.1: Schematic diagram illustrating the procedure for obtaining the fractal dimension of a pattern of points using the box-counting method (modified from Carranza, 2009). Grids of square cells with side lengths,  $\delta$ , are overlain over the point pattern. After each iteration, the number of square cells containing at least one point,  $n(\delta)$ , is counted. The dummy resulting plot on the right-hand side for the three iterations completed in this figure indicates a bifractal pattern with box-counting fractal dimensions of 0.825 and 1.384 based on the power functions of the equations. Because the dimensions of the thin sections in this study were exaggerated to facilitate viewing on a scale suitable for a laptop computer (see Chapter 3), the dimensions depicted in this log-log plot should be divided by 100 to obtain the correct micro-scale value.

Figure 7.2: Log  $n(\delta)$  vs log  $\delta$  plots indicating fractal dimensions of patterns of sphalerite grains in thin sections of oriented samples from the Golden Eagle mine and prospect site: (A) GE-01, (B) GE-02, (C) GE-04, (D) GE-09, and (D) GE-10. The difference in colour of the points indicates a change in fractal dimension. Because the dimensions of the thin sections in this study were exaggerated to facilitate viewing on a scale suitable for a laptop computer (see Chapter 3), the dimensions depicted in these log-log plots should be divided by 100 to obtain the correct micro-scale value.

Figure 7.3: Log  $n(\delta)$  vs log  $\delta$  plots indicating fractal dimensions of patterns of sphalerite grains in thin sections of oriented samples from the Champion Mine and prospect site: (A) CM-15B, (B) CM-19, and (C)

CM-24. The difference in colour of the points indicates a change in fractal dimension. Because the dimensions of the thin sections in this study were exaggerated to facilitate viewing on a scale suitable for a laptop computer (see Chapter 3), the dimensions depicted in these log-log plots should be divided by 100 to obtain the correct micro-scale value.

Figure 8.1: Trends in the orientations of ellipses that best-fit sphalerite grains in oriented images of thin sections of samples collected from the Golden Eagle Mine and prospect site. (a) GE-01,  $n = 69$ ; (b) GE-02,  $n = 765$ ; (c) GE-03,  $n = 242$ ; (d) GE-04,  $n = 88$ ; (e) GE-09,  $n = 100$ ; and (f) GE-10,  $n=42$ .

Figure 8.2: Trends in the orientations of ellipses that best-fit sphalerite grains in oriented images of thin sections of samples collected from the Champion Mine and prospect site. (a) CM-04,  $n = 320$ ; (b) CM-15B,  $n = 48$ ; (c) CM-19,  $n = 130$ ; and (d) CM-24,  $n = 59$ .

Figure 9.1: Lithological map of the Ngubevu West Area (modified from Basson, 2000) displaying a fracture mesh model of regularly spaced NE-SW- and NW-SE-trending sets of posited macro-scale fractures around the Golden Eagle and Champion Mine areas and prospect sites. Regularly spaced mineral deposits were plausibly formed along the fractures while deposit clusters were plausibly formed along the intersections of these fractures. The  $S_1$  foliation in the Ngubevu area has a nearly E-W trend. The model presented on the right-hand panel of the map indicates N–NE-directed compression which resulted in the formation of the fractures (dashed lines indicate the orientation of the foliation). This model is constructed only for the two mines of interest and not the whole area because of a lack of data between the two mines (i.e., samples were only collected at the mines of interest).

Figure 9.2: Micro-maps of sample CM-24 indicating (A) the micro-fracture pattern, (B) the micro-scale spatial pattern of centroids of sphalerite grains and (C) the postulated spatial association between micro-fractures and mineral deposits in the study area.

Figure A.1: Spatial distribution of centroids of sphalerite grains in thin sections of samples from the Golden Eagle mine area and prospect site.

Figure A.2: Spatial distribution of centroids of sphalerite grains in thin sections of samples from the Champion Mine and prospect site.

*Figure B.1. Spatial distribution of Fry points plotted for thin sections of samples from the Golden Eagle mine and prospect site. (A) GE-01, (B) GE-02, (C) GE-04, (D) GE-09 and (E) GE-10.*

*Figure B.1. Spatial distribution of Fry points plotted for thin sections of samples from the Champion Mine and prospect site. (A) CM-15B, (B) CM-19, (C) CM-24.*

*Figure C.1: Oriented photomicrographs of thin sections of samples from the Golden Eagle mine area and prospect site. The light grey areas are occupied by sphalerite grains while the darker grey areas are occupied by gangue minerals comprising quartz, plagioclase feldspar, and minor biotite. North is parallel to the long edge of the page border all in images.*

*Figure C.2: Oriented photomicrographs of thin sections of samples from the Golden Eagle mine area and prospect site. The light grey areas are occupied by sphalerite grains while the darker grey areas are occupied by gangue minerals comprising quartz, plagioclase feldspar, and minor biotite. North is parallel to the long edge of the page border in all images.*

*Figure C.3: Oriented photomicrographs of thin sections of samples from the Champion Mine area and prospect site. The light grey areas are occupied by sphalerite grains while the darker grey areas are occupied by gangue minerals comprising quartz, plagioclase feldspar, and minor biotite. North is parallel to the long edge of the page border in all images.*

*Figure D.1: Binary images of sphalerite grains in oriented photomicrographs of thin sections of samples from the Golden Eagle mine area and prospect site fitted with best-fit ellipses.*

*Figure D.2: Binary images of sphalerite grains in oriented photomicrographs of thin sections of samples from the Golden Eagle mine area and prospect site fitted with best-fit ellipses.*

*Figure D.3: Binary images of sphalerite grains in oriented photomicrographs of thin sections of samples from the Champion Mine area and prospect site fitted with best-fit ellipses.*

## LIST OF TABLES

*Table 4.1: Interpretations of micro-fracture data from the Golden Eagle mine area and prospect site.*

*Table 4.2: Interpretations of micro-fracture data from the Champion mine area and prospect site.*

*Table 5.1: Average numbers of different orders of RNNs and averages of different orders of neighbour distances in the spatial pattern of ore centroids in the thin sections of samples from the Golden Eagle mine and prospect site.*

*Table 5.2: Average numbers of different orders of RNNs and averages of different orders of neighbour distances in the spatial pattern of ore centroids in the thin sections of samples from the Champion Mine and prospect site.*

# CHAPTER 1:

## INTRODUCTION

This research project endeavoured to contribute to a better understanding of the multi-scale structural controls on shear-zone-hosted precious and base metal mineralisation in the Ngubevu area of the Natal Thrust Front in the Tugela Terrane of South Africa. This was achieved by analysing the trends of micro-fractures and the trends in micro-scale distributions of ore minerals in thin section samples of vein material from the Golden Eagle and Champion Mines in the Ngubevu area, in the Natal Thrust Front of the Tugela Terrane in the Natal Metamorphic Province. The findings of the analyses were integrated with existing knowledge of regional- to local-scale deformation in the Tugela Terrane to deduce the trends of shear-zone-hosted precious and base metal mineralisation and the trends of structures controlling such mineralisation occurrences in the Golden Eagle and Champion Mines, or other parts of the Ngubevu area. The outcomes of this research are critical to better exploration targeting in future projects in the Ngubevu area.

**Research Question:** Can trends in the micro-scale distributions of ore minerals provide insights to local-scale controls on shear-zone-hosted precious and base metal mineralisation in the Ngubevu area?

### 1.1. BACKGROUND

Unlike the western Namaqualand Metamorphic Province, which is well-explored and well-exploited for several mineral deposits, the Natal Metamorphic Province (NMP) is relatively poorly explored (Thomas et al., 1990). This has been attributed to the mountainous terrane, deep weathering profile, poor outcrop pattern and thick vegetation cover, which make mineral exploration difficult in the NMP (Thomas et al., 1990). Another reason is that the structural control on mineralisation in the NMP is poorly understood. Moreover, the literature on mineralisation within the NMP is limited, apart from a few articles on specific mineral occurrences (Reynolds, 1986; Wuth and Archer, 1986; Thomas and Gain, 1989) and a review by Thomas et al. (1990).

The study of micro-structures is a growing field of interest in the geosciences, and it is a valuable asset in understanding the structural geology of certain regions (Blenkinsop, 2002; Mukherjee, 2013), and, therefore, structural controls on the formation of certain types of mineral deposits. However, in the economic geology literature, ideas of regional-scale structural controls on mineral deposit formation are often primarily linked to deposit-scale data on mineral deposits (Duncan et al., 2014). This is the case in the Ngubevu area, where researchers have linked mineral deposit formation and occurrence to the regional-to-local-scale ductile fabrics present in the rocks of the Mfongosi Group (Thomas et al., 1990; Bullen et al., 1994; Basson, 2000; Basson and Watkeys, 2000).

To better understand the nature of the mineralisation in the Ngubevu area, knowledge from previous works was combined with new data generated by this research to elucidate the structural control on shear-zone-hosted precious and base metal mineralisation. The knowledge of local-scale structural controls on deposit formation was derived from Basson (2000), who examined the Golden Eagle and Champion Mines in the Ngubevu West area. Here, the orientations of planar foliations and quartz feldspar-veins observed by Basson (2000) were correlated and integrated with data generated from the micro-scale analyses of micro-fractures and ore mineral distributions generated in this study. Data from foliations and veins were considered representative evidence of controls on mineralisation in the Ngubevu area and, regionally, the Tugela Terrane (Thomas et al., 1990; Bullen et al., 1994; Basson, 2000).

The distribution of ore minerals present in the micro-scale of the Golden Eagle and Champion Mines were studied in thin section using the spatial analytical techniques of point pattern analysis, Fry analysis, fractal analysis, and shape analysis. Spatial analyses of mineral deposit distributions allow reasonable inferences to be drawn about structural controls on mineral deposit formation (Hodkiewicz et al., 2005).

## **1.2. RESEARCH AIMS AND OBJECTIVES**

This research aimed to investigate the hypothesis that local-scale structural controls on shear-zone-hosted precious and base metal mineralisation can be inferred from the micro-scale distributions of ore minerals, micro-fractures, and local-scale structures at/around deposit sites. To do so, a thorough interpretation of the structural controls on precious and base metal mineralisation in the Golden Eagle and Champion Mines in the Ngubevu area was provided through the investigation of the micro-and local-scale patterns of structures and ore deposits.

To achieve the above-stated aim of this research, the following objectives were sought:

1. To generate new micro-structural data from oriented samples of quartz-feldspar veins, which host the mineralisation in the Golden Eagle and Champion Mines, by the mapping of micro-fractures present in oriented thin sections of the samples (Chapter 4).
2. To examine by point pattern analysis the micro-scale spatial distributions of ore minerals (Chapter 5).
3. To examine by Fry analysis the trends in the micro-scale distributions of the ore minerals (Chapter 6).
4. To examine by fractal analysis the behaviour of the ore minerals in the thin section to micro-scale (Chapter 7).
5. To examine the micro-scale orientations of shapes of the ore minerals using the best-fit shape analysis method (Chapter 8).
6. To analyse, compare, and synthesise the new micro-scale structural measurements with existing structural measurements collected at/around the mines to infer local-scale structural controls on mineralisation (Chapter 9).
7. To provide recommendations for mineral targeting in the Ngubevu area based on the micro- to local-scale analyses carried out in this research (Chapter 10).



## **CHAPTER 2:**

### **LITERATURE REVIEW**

#### **2.1. REGIONAL GEOLOGY**

The Mesoproterozoic Natal Metamorphic Province (NMP) forms part of a 400-km-wide metamorphic belt referred to as the Namaqua-Natal Metamorphic Province, which stretches from the Northern Cape on the west coast to KwaZulu-Natal on the east coast of South Africa and is approximately 1250 Ma old (Figure 2.1) (Thomas et al., 1990; McCourt et al., 2006). The Namaqua-Natal Metamorphic Province developed during the Kibaran Orogeny when the supercontinent Rodinia was assembled (Jacobs and Thomas, 1994; Cornell et al., 1996; McCourt et al., 2006; Sharib et al., 2021).

Lithological assemblages in the NMP crop out as a series of inliers and have a broadly E–W-trending structural fabric due to N–NE-directed compression that occurred during deformation and metamorphism (Thomas et al., 1990). The NMP is divided into three tectonostratigraphic terranes based on different lithological assemblages and metamorphic grades, each bounded by tectonic contacts (Figure 2.2). These terranes form a N–S extension along the coast of KwaZulu-Natal and they are referred to as the Tugela, Mzumbe and Margate tectonostratigraphic terranes (Figure 2.1) (Thomas et al., 1990; McCourt et al., 2006). The NMP is a juvenile orogen, and the most ancient rocks are arc-related gneisses of supracrustal origin, felsic to mafic metavolcanic gneisses and minor paragneiss, which have been intruded by ca. 1.2 Ga calc-alkaline orthogneisses in the Mzumbe and Margate Terranes (Figures 2.1 and 2.2) (Eglington et al., 1989; Jacobs et al., 1993; Arima et al., 2001). The Tugela Terrane comprises multi-layered amphibolites and secondary quartz-feldspar gneisses, which are hosted in thrust sheets and intruded by plagiogranites, mafic-ultramafic complexes and serpentinites with minor metasedimentary rocks (Jacobs et al., 1993; Jacobs and Thomas, 1994).

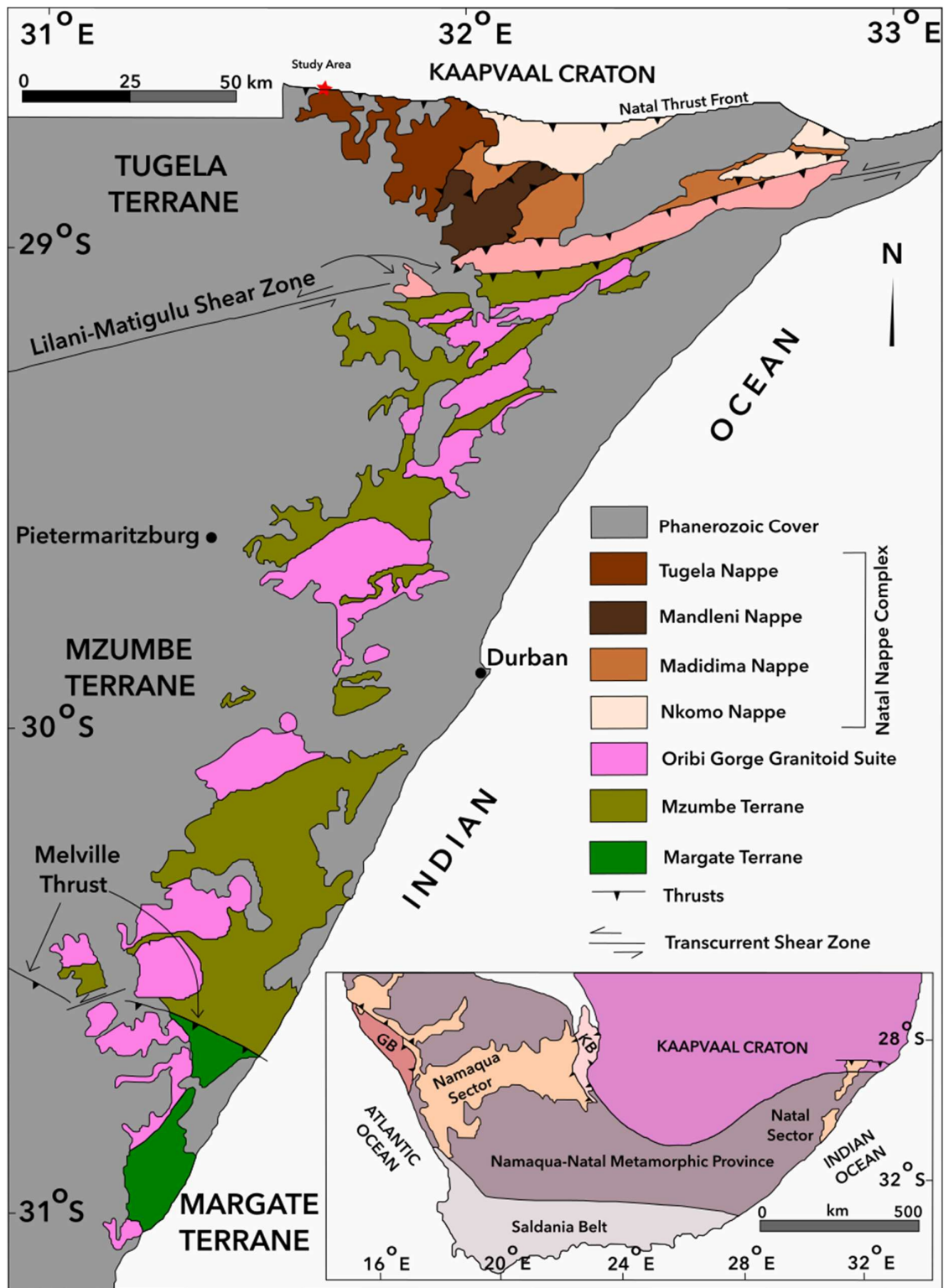


Figure 2.1: Geology and distribution of terranes and lithologies of the Natal Metamorphic Province (modified after Sharib et al. (2021)). The extent of the Namaqua-Natal Metamorphic Province beneath rocks of the Karoo Supergroup is indicated by the inset map. Also shown is the Namaqua Province on the west coast. GB = Gariep Belt and KB = Kheis Belt. The approximate location of the Ngubevu area is indicated by a red star on the Natal Thrust Front; more precise location is indicated in Figures 2.3 and 2.4.

The dominant fabric in the lithologies of the NMP formed during deformation and it is consistent with N–NE-directed thrusting and recumbent folding due to accretion of the tectonostratigraphic terranes at approximately 1.1 Ga (Thomas, 1989; Jacobs and Thomas, 1994; Cornell et al., 1996). After accretion, the Mzumbe and Margate terranes were deformed by numerous NE–NNE-aligned, sinistral, steeply dipping lateral shear zones due to prolonged N–NE-directed crustal thickening and deformation against the oblique, nearly E–W boundary of the Kaapvaal Craton (Thomas, 1989; Jacobs et al., 1993; Jacobs and Thomas, 1994; Cornell et al., 1996). The shear zones indicate transpressional to transtensional movements, and transtensional segments were postulated to indicate orogenic collapse (Jacobs et al., 1993). During this advanced collision phase, rapakivi-textured granites from the Oribi Gorge Suite intruded into the Mzumbe and Margate Terranes along these zones of transcurrent shearing (Jacobs and Thomas, 1994; Cornell et al., 1996). However, the structures preserved in the Tugela Terrane are chiefly those of the initial phase of accretionary tectonics, as it was primarily shielded during ongoing deformation and metamorphism due to its position on the stable Kaapvaal Craton (Figure 2.2) (Jacobs et al., 1993).

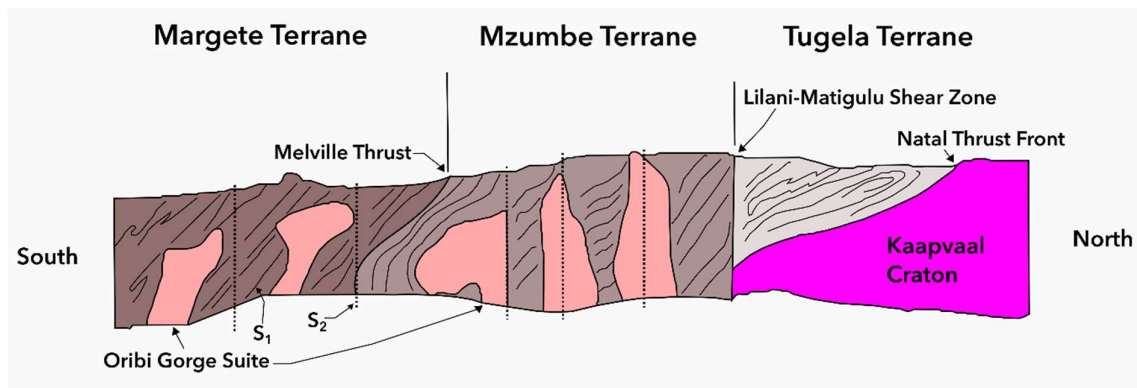


Figure 2.2: Idealised S–N cross-section along the Natal Metamorphic Province indicating the three tectonostratigraphic terranes and their related structures (modified from Mendonidis and Thomas, 2019).

Initially, a two-stage composite arc terrane accretion model was proposed for the evolution of the NMP (Jacobs and Thomas, 1994). In the opening stage, the Tugela Terrane was thrust onto the Kaapvaal Craton margin as the Margate and Mzumbe Terranes were accreted

together, and then during the second stage, the Mzumbe–Margate composite arc was accreted to the Tugela Terrane along the Lilani–Matigulu Shear Zone (Jacobs and Thomas, 1994; Arima et al., 2001; Basson et al., 2005; McCourt et al., 2006). Gravity modelling conducted in the Lilani–Matigulu Shear Zone revealed that this zone of shearing represents the boundary of the Archaean Craton with the northern Tugela Terrane lying directly above the craton (Barkhuizen and Matthews, 1990). This explains the pervasive presence of similarly oriented structures primarily from the initial phase of deformation in the Tugela Terrane. Current studies and data of geochronology in the NMP support a three-stage accretion model where, in the first stage, the Tugela Terrane was thrust onto the Kaapvaal Craton; during the second stage the Margate and Mzumbe Terranes were amalgamated together at ca. 1100–1080 Ma and signalled by syn-collisional granitoid intrusions; the Margate–Mzumbe composite arc then accreted onto the margin of the Kaapvaal Craton/Tugela Terrane during the final stage of accretion (Spencer et al., 2015; Mendonidis and Thomas, 2019). A post-accretion collision phase and late-tectonic magmatism contemporaneous with lateral shearing occurred at ca. 1050–1030 Ma and it is indicated by the Oribi Gorge Suite intruding into the southern terranes (Basson, 2000; Eglington et al., 2003; Spencer et al., 2015; Mendonidis and Thomas, 2019). However, due to its position overlying the Kaapvaal Craton, the Tugela Terrane was unaltered by these late shearing and magmatic events (McCourt et al., 2006). Although the formational details differ between the two models of terrane accretion, both agree that the NMP formed due to subduction directed southwards and away from the Kaapvaal Craton margin (McCourt et al., 2006; Mendonidis and Thomas, 2019).

## **2.2. TUGELA TERRANE**

The Tugela Terrane (Figure 2.3) formed when an island arc, referred to as the Tugela arc, and the Mandleni Oceanic Island were accreted together and then thrust onto the Kaapvaal Craton during N–NE-directed deformation and metamorphism (McCourt et al., 2006). This terrane was previously postulated to be an obducted ophiolite suite (Matthews, 1981; Cornell et al., 1996; Basson, 2000). However, this assertion was disproved by geochemical data, which showed that it is an amalgamated island arc and oceanic island terrane rather than an ophiolite suite (Bisnath, 2000; Arima et al., 2001; Johnston et al., 2003). This Tugela Terrane is divided into the Natal Nappe Complex and Natal Thrust Front and it comprises a

diverse assemblage of rocks. The Natal Thrust Front is a steeply inclined and tapered zone of S-dipping and overlapping greenschist facies rocks, about 2–12 km wide, while the Natal Nappe Complex comprises amphibolite and amphibolitic gneiss-dominated lithologies with lesser metasedimentary schist and gneiss, and intermittent carbonates (Matthews, 1972; Bisnath et al., 2008; McCourt et al., 2006).

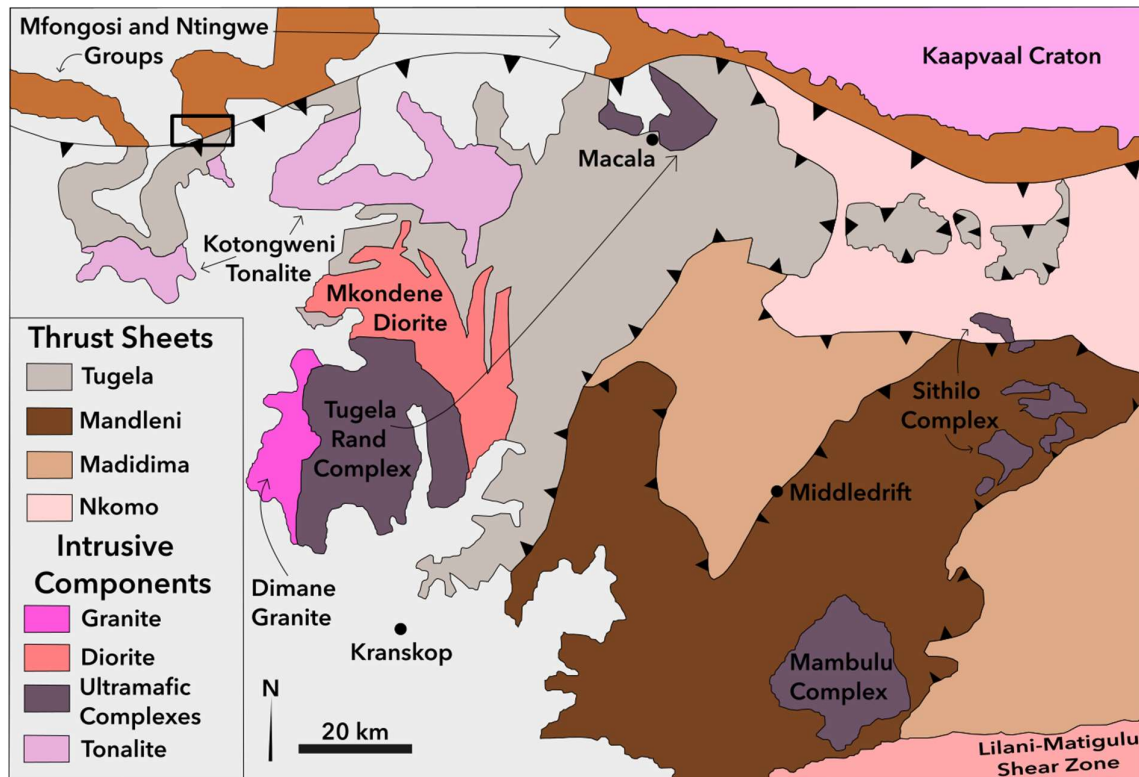


Figure 2.3: Geological map of the Tugela Terrane indicating the Nappe Complex/Zone and related intrusions and the Ntingwe and Mfongosi Groups of the Natal Thrust Front (modified from McCourt et al. (2006)). The Ngubevu area is indicated by the rectangular box in the NW quadrant of the map.

The Tugela Terrane is in tectonic contact with the Mzambe Terrane to the south along the ENE-trending, steeply S-dipping and left-lateral Lilani–Matigulu Shear Zone (Barkhuizen and Matthews, 1990; Jacobs and Thomas, 1994). The transcurrent shearing observed along this shear zone, which is located roughly 50 km south of the study area (see Fig. 2.1), persisted northwards throughout the Tugela Terrane and this transcurrent shearing is postulated to be the control on epigenetic precious metal mineralisation in the terrane (Bullen et al., 1994; Basson, 2000).

### 2.2.1. NATAL NAPPE COMPLEX

The Natal Nappe Complex (referred to in some literature as the Natal Nappe Zone) comprises four gently westward-plunging thrust sheets namely, from west to east, the Tugela, Mandleni, Madidima and Nkomo Thrust Sheets (Figure 2.3). They form a regional antiformal thrust stack bounded by tectonic contacts, which are distinguishable through the occurrence of ultrabasic lenses and talc schists (Matthews, 1981; Cornell et al., 1996; McCourt et al., 2006; Bisnath et al., 2008). The thrust sheets comprise granitic gneiss, amphibolite, metabasite with bands of granitic gneiss, magnetite quartzite, and ultramafic pods and lenses (Cornell et al., 1996; Johnston et al., 2003; Basson et al., 2005). These supracrustal rocks are intruded by metamorphosed mafic and ultramafic rocks (Cornell et al., 1996). Following the original description of Matthews (1972), researchers often use the term Tugela Terrane in reference only to the Natal Nappe Complex (Thomas, 1989; Bullen et al., 1994; Jacobs and Thomas, 1994; Arima and Johnston, 2001; Johnston et al., 2003; McCourt et al., 2006; Bisnath et al., 2008; Mendonidis and Thomas, 2019; Sharib et al., 2021). However, Basson (2000) and Basson et al. (2005) used a four zonal description of the NMP, making the Natal Thrust Front and Natal Nappe Complex separate tectonostratigraphic terranes without confinement to the term Tugela Terrane. In this research, the term Tugela Terrane is used as an umbrella term that includes both the Natal Nappe Complex and the Natal Thrust Front.

The primary structures of the rocks in the Natal Nappe Complex have been transposed and destroyed by extensive deformation and recrystallisation (Bisnath et al., 2008).  $D_1$  structures are found in the early-formed structures as rare inclusion trails in garnet and detached isoclinal intrafolial folds (Sharib et al., 2021). Four planar foliations ( $S_1$  to  $S_4$ ) and a single lineation ( $L_2$ ) that resulted from regional N–NE-directed thrusting and metamorphism are recognised (Johnston et al., 2003; Bisnath et al., 2008). The  $S_1$  foliation is extensively overprinted by subsequent deformation events and is only locally visible in the vicinity of uncommon NE-verging  $F_2$  isoclinal, detached folds that distort the compositional layering in the Mandleni Thrust Sheet (Johnston et al., 2003; McCourt et al., 2006).  $S_2$  has been designated as the dominant regional foliation (Johnston et al., 2003). However, the  $S_2$  and  $S_3$

fabrics may only be separated based on metamorphic grade (McCourt et al., 2006). The  $S_2$  foliation dips towards the SW and varies from moderately to gently inclined (Sharib et al., 2021). The  $S_1$ ,  $S_2$  and  $S_3$  foliations are observable in rocks of the Mandleni, Madidima and Tugela Nappes, and  $S_2$  is parallel to lithological contacts and compositional banding in the Mandleni Thrust Sheet (Johnston et al., 2003; McCourt et al., 2006; Bisnath et al., 2008). A retrogressive syn-kinematic metamorphic event ( $D_4$ ) that resulted from orogenic collapse produced open, southwards plunging folds/fold axes together with a widely separated, weak  $S_4$  foliation (McCourt et al., 2006; Sharib et al., 2021).

The  $S_2$  fabric was formed during dominant isoclinal, asymmetric, and NE-vergent folding ( $F_3$ ) and transposition of older contacts during  $D_2$ ;  $S_2$  is folded and faulted at both local and regional scales and is largely overprinted by  $S_3$  in the Mandleni Thrust Sheet resulting in a composite  $S_2/S_3$  foliation (Johnston et al., 2003). The regional deformation of  $S_2$  during  $D_3$  resulted from SW-dipping, NE-verging brittle-ductile shearing and thrust faulting parallel to the  $F_3$  fold axial planes; these shear zones and faults routinely disrupt the steeply dipping limbs and cores of the  $F_3$  folds (McCourt et al., 2006; Bisnath et al., 2008).  $S_2$  is locally deformed into well-defined wave-like structures that have W- and SW-oriented axes (McCourt et al., 2006; Bisnath et al., 2008).  $F_3$  folds have WNW–ESE- to NW–SE-oriented axial planes, and the  $S_2$  and  $S_3$  foliations run parallel along limbs of  $F_3$  folds but are at high angles to each other at the hinges (McCourt et al., 2006; Sharib et al., 2021).

The Mtungweni granitoids, which were intruded after the  $D_2$  event, lack pervasive foliation and have a cross-cutting relationship with the compositional banding in the lithologies of the Mandleni and Madidima Thrust Sheets (McCourt et al., 2006). They are partly coeval with the  $D_3$  event as, even though they are deformed by  $F_3$  folds, they lie adjacent to axial planes of the  $F_3$  folds and indicate  $D_3$  compression-related ductile shear zones (McCourt et al., 2006).

A persistent nearly E–W-trending  $S_2$  foliation that dips towards the S and SW occurs in the Nkomo Thrust Sheet and is locally cross-cut by aplitic sheets (McCourt et al., 2006). The foliation and aplitic sheets are both, in turn, deformed by tight and asymmetrical  $F_3$  folds, which have been overturned towards the NE (Smalley, 1979; McCourt et al., 2006). The

foliation of the Nkomo and Madidima nappes is thought to be a composite foliation involving all or combinations of the  $S_0$ ,  $S_1$ , and  $S_2$  fabrics (Sharib et al., 2021).

The most recent study undertaken in the Madidima Thrust Sheet recognised a complex array of foliations related to the  $D_2$  event of the Natal Nappe Complex and another deformation event,  $D_5$ , with comparable tectonic transport directions to  $D_2$  and  $D_3$  (Sharib et al., 2021). An  $S_2$  foliation that is sub-vertically inclined and a NE–SW-oriented axial planar foliation were collectively termed  $S_{2b}$ , and differ from the dominant regional  $S_2$  foliation (termed  $S_{2a}$ ) with low to moderate dips; the two foliations are associated but differ in orientation (Sharib et al., 2021). The folds related to these foliations are  $F_{2a}$  and  $F_{2b}$ , and lineations commonly coaxial with the fold axis are apparent on  $S_2$  surfaces of the  $F_{2b}$  folds; these lineations are also sub-parallel to intersections of  $S_0$  and  $S_{2b}$  axial planes (Sharib et al., 2021).

A typically NE–SW-trending and locally concentrated lineation ( $L_2$ ) is visible in numerous lithologies on the surfaces of  $S_{2a}$  foliations, and the axes of syn- and pre- $D_2$  folds are variably orientated towards  $L_2$  (Sharib et al., 2021). The  $D_5$  event occurred during a period of N–NE-directed “cold thrusting” during a retrograde phase characterised by brittle–ductile deformation at the thrust sheet boundaries and signifies the final phase of thrust-related tectonism in the Tugela Terrane (Sharib et al., 2021).

### **2.2.2. NATAL THRUST FRONT**

The Natal Thrust Front (Figure 2.4) occurs at the northernmost extremity of the NMP and it is separated from the Natal Nappe Complex by the Manyane Thrust (Figure 2.5) (McCourt et al., 2006). It constitutes the leading edge of lithological assemblages in the northern Tugela Terrane and comprises the Ntingwe and Mfongosi Groups (Arima et al., 2001; Johnston et al., 2003; McCourt et al., 2006). The 300-m-thick Ntingwe Group is the northernmost assemblage of rocks in the Natal Thrust Front, and it comprises metamorphosed conglomerates and breccias that are overlain by non-schistose dolomite, limestone, shale, and mudstone (Basson and Watkeys, 2003; Basson et al., 2005). The Mfongosi Group encompasses phyllitic quartzite and schists of variable composition (Cornell et al., 1996; Basson and Watkeys, 2003; Basson et al., 2005; McCourt et al., 2006). The rocks of the Natal Thrust Front are separated from the Kaapvaal Craton by the Mfongosi Thrust; this thrust

progressively steepens along with the craton margin from 10°–20° in the west to 45°–60° in the east (Cornell et al., 1996). The most pervasive geological structures in the Natal Thrust Front comprise E–W-, ENE- and ESE-trending folds with axial surfaces that dip towards the S, interrupted by over-thrusting close to the northern foreland (Basson, 2000; Johnston et al., 2001; Basson and Watkeys, 2003).

The Mfongosi Group in the area of Ngubevu comprises the most intensely deformed and metamorphosed rocks of the Natal Thrust Front, with the intensity subsiding eastwards towards the Mfongosi Valley, where it reaches greenschist facies (Basson, 2000; Basson and Watkeys, 2003). The Mfongosi Group lithological assemblages in the Mfongosi Valley are subdivided into those of the Northern and Southern Mfongosi Valley, with varying structural complexity and lithologies between the two localities.

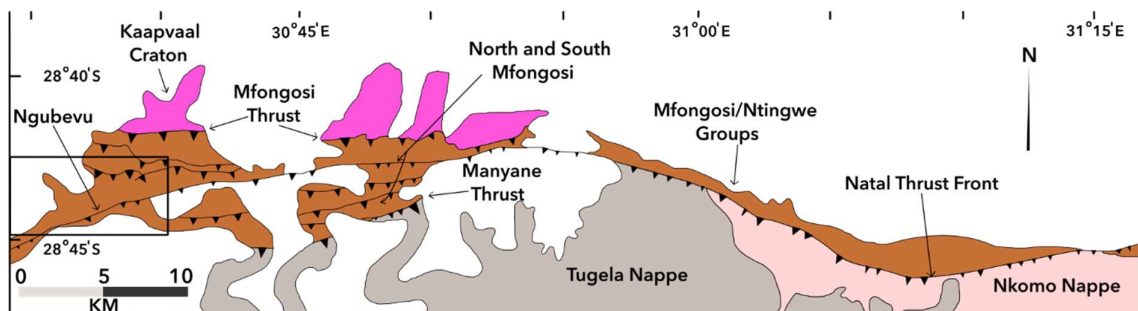


Figure 2.4: Geology and distribution of rocks of the Natal Thrust Front (modified from Basson and Watkeys (2003)). The rectangular box denotes the study area, which continues towards the left out of this map.

The Northern Mfongosi Valley comprises steeply inclined metagreywackes and rare metabasites with an average dip/strike of 59°/083° (Basson, 2000). Structures in the Northern Mfongosi Valley indicate that the Mfongosi Group has undergone only minor lateral transpression, in contrast to the Ngubevu area where high pure and simple shear were experienced (Basson, 2000; Basson and Watkeys, 2003). Kink folds indicating a late sinistral, transpressional event are common, with sections of the Mfongosi Group comprised of a brittle melange (Basson, 2000).

In the Southern Mfongosi Valley, the Mfongosi Group comprises a complex banding of metasedimentary quartz-feldspar schists and metatholeiitic feldspar- and epidote-

dominated schists with an average dip/strike of  $73^{\circ}/077^{\circ}$  (Basson, 2000; Basson and Watkeys, 2003). The steep dip of the rock sequences here results from the influence of the Manyane fault/thrust at the base of the Tugela Thrust Sheet (Figure 2.5) (Basson and Watkeys, 2003).

#### 2.2.2.1. *Ngubevu Area*

The Ngubevu area occurs NW of the Mfongosi area and comprises dominantly schistose epidote-actinolite-feldspar-talc  $\pm$  calcite bearing rocks, chlorite amphibolite with minor crenulated and fine-grained graphite-tourmaline-quartz-albite metasedimentary schist (De Klerk, 1991; Basson, 2000; Basson and Watkeys, 2003). Dominant structures of the Ngubevu area are ESE–WNW- to E–W-oriented folds with axial planar foliations dipping steeply towards the S and SSW at angles of about  $70^{\circ}$ – $80^{\circ}$  (Basson et al., 2005).

In this area, the Mfongosi Group has been affected by three deformation events.  $D_1$  is characterised by oblique NE–SW-directed “multi-arc” collision (Basson et al., 2005). The primary fabric,  $S_0$ , is observable along strongly sheared and poorly lineated margins of rocks and occasionally at boundaries of metabasites and thin metapelitic bands; one significant fold is noticeable in epidote-actinolite and chlorite schists (Basson et al., 2005). Actinolite crystals that are oriented E–W define an  $S_1$ , which is locally indistinguishable from  $S_0$  (Basson et al., 2005). However,  $S_0$  dips towards the N in some areas and defines the northern limbs of shallowly plunging E and ESE  $F_1$  folds, which have steeply inclined S- and SSW-dipping axial planes (Basson et al., 2005).

$D_2$  occurred due to transpression along ENE-trending structures, which resulted in the formation of crenulations and kink folds with hinges at steep angles to  $F_1$  (Basson et al., 2005). Two fabric occurrences define the  $D_2$  event; the first in epidote-actinolite and chlorite schists as  $S_2$  and the second as a synthetic planar surface in a left-lateral shear sense by transposition of  $S_1$  (Basson et al., 2005).  $S_2$  differs in strike to  $S_1$  and is apparent in cross-cutting field relations, even though the separation of  $F_1$  and  $F_2$  folds is not commonly possible in the field; the axes of  $F_2$  axial planes have an average dip/strike of  $52^{\circ}/230^{\circ}$  (Basson et al., 2005).

#### 2.2.2.2. *Mfongosi Area*

In the type area for the Mfongosi Group, it comprises a combination of metamorphosed medium- to coarse-grained sedimentary rocks and minor volcanoclastic rocks, and the deformation is distinct from that in the Ngubevu Area (Basson et al., 2005). In the Mfongosi area, slickenlines ( $L_1$ ) with shallow SSW- to SW-plunges and often containing linear distributions of pyrite that show sinistral shearing towards the S are indicative of the first deformation event ( $D_1$ ); these slickenlines are succeeded by steeply S-plunging lineations (Basson et al., 2005). It is not possible to distinguish  $D_1$  from subsequent deformational events in the area; however, Basson et al. (2005) have interpreted the variability in slickenline orientations to suggest a rotation of the far-field stress during deformation. The ENE–WSW orientation of veins attributed to  $D_1$  in the Northern Mfongosi Valley and their E–W orientation in the Southern Mfongosi Valley are also interpreted to indicate clockwise rotation with NNW-directed thrusting in the south (Basson et al., 2005).  $D_2$  in the Mfongosi Area is most apparent where an ESE–WNW-trending foliation is present in the N, and numerous SW-plunging kink folds indicate N–NE-directed thrusting (Basson et al., 2005).

#### 2.2.2.3. *Manyane Thrust*

The Manyane Thrust (Figure 2.5) marks the tectonic boundary between the Natal Nappe Complex and the Natal Thrust Front; two deformation events that occurred during the juxtaposition of these terranes are apparent in amphibolite sequences (Basson et al., 2005). The orientation of  $D_1$  thrusting is comparable to that of  $S_0$  in the Mfongosi Group, and  $L_1$  is defined by elliptical basalt pillows, the long axes of which plunge steeply ( $70^\circ$ ) towards the S and SSW, and  $D_2$  is evidenced by the superimposition of SSW-plunging slickenlines on  $S_1$  foliations and the margins of  $L_1$  (Basson et al., 2005).

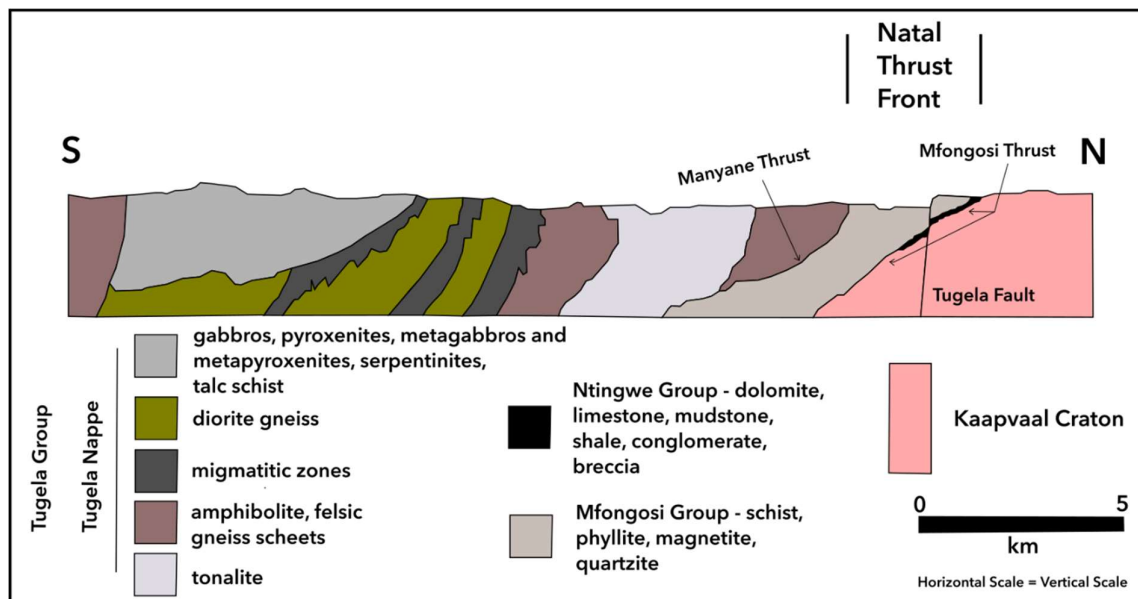


Figure 2.5: S–N cross-section along the western end of the Tugela Terrane, indicating the relationship between rocks of the Natal Nappe Complex (Tugela Nappe) and the Natal Thrust Front (modified from Basson et al., 2005).

### 2.3. LOCAL GEOLOGY

In this section, local- and deposit-scale data around the mine sites in the Ngubevu Area from the PhD dissertation of Basson (2000) are summarised. This previous work has also been published in the literature by Basson et al. (2005). Few changes were made, however, to the naming and positioning of the mines per the local guides' indigenous knowledge of the area and the 1: 50 000 scale regional geological map – sheet 2830DA Collessie. The Golden Eagle mine sits west of the Ngubevu River, while the Champion Mine is situated to the east. The locations of these mines are displayed in Figure 2.6, and the localities at/around these mines were the focus of this study. However, three other known mines also depicted in Figure 2.6 exist in the area (Thomas et al., 1990; Basson, 2000). These are the Golden Dove Mine east of the Champion Mine and west of the Tugela River, the HMS Mine east of the Golden Dove Mine and south of the Tugela River, and the Buffalo River Mine north of the Tugela River and west of the Buffalo River. Mines in the Ngubevu area are oriented parallel to the strike of the host graphite-bearing schist while prospecting trenches at and around each mine have been cut perpendicular to the strike of the  $S_1$  foliation in the Mfongosi Group. The deposit-scale database for this research was established by digitisation of  $S_1$  planar foliation and vein orientation measurements depicted in the lithological map of the Ngubevu West area

(Basson, 2000), where the two mines of interest for this study are situated. These digitised data from Basson (2000) were supported by field structural measurements of the  $S_1$  planar foliation collected during the sampling phase of this study.

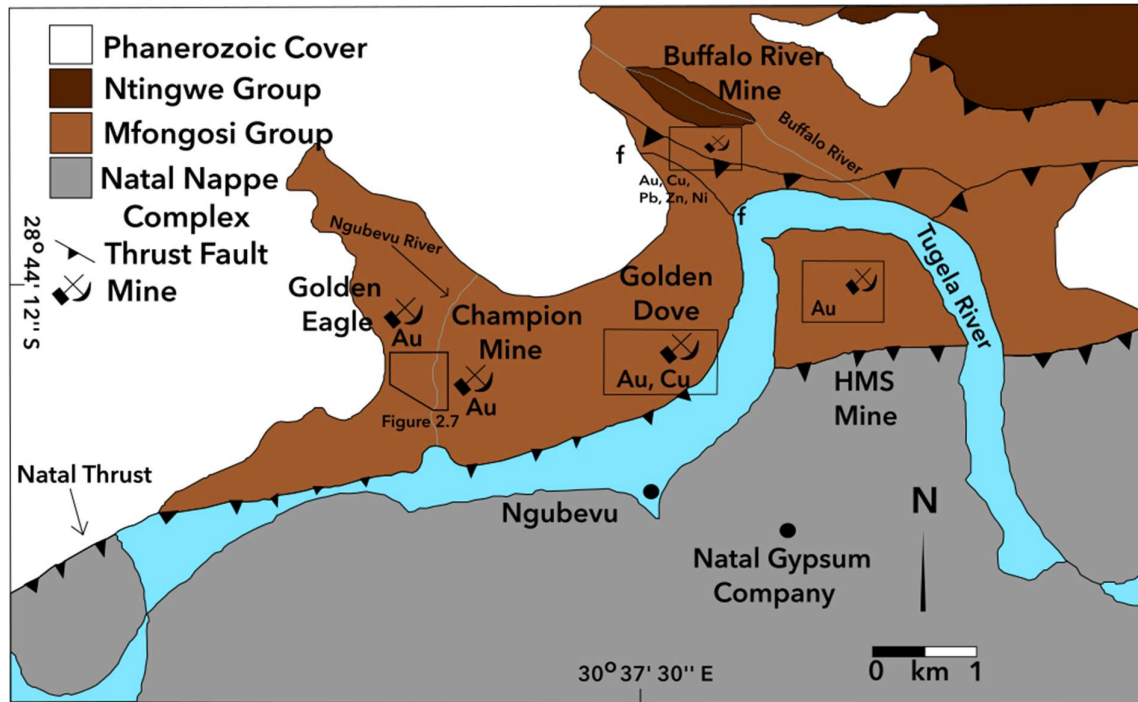


Figure 2.6: Map showing the geology of the Ngubevu area (modified from Basson, 2000). Locations at/around the Golden Eagle and Champion Mines in the western portion of the Ngubevu area were the focus of this study.

### 2.3.1. GEOLOGY

The geology at/around the Golden Eagle and Champion Mines (Figure 2.7) is dominated by two main lithological units with distinctive field appearances and weathering relief; a third rock unit forms lenses aligned parallel to the approximately E–W-trending regional foliation (Basson, 2000). The central segment of the Ngubevu West Area comprises dominant fine-grained calcite-quartz-albite  $\pm$  talc  $\pm$  sericite  $\pm$  chlorite schist intercalated with calcite-bearing schist in the southern and northern limbs of a regional  $F_1$  fold (Basson, 2000). The most expansive lithology in the area comprises the southern and northern limbs of the regional  $F_1$  fold in this portion of Ngubevu and it is an epidote-actinolite-quartz-talc  $\pm$  calcite schist (Basson, 2000). The schists are compositionally homogeneous in areas where quartz-

feldspar veins, quartz-calcite-talc and quartz-calcite-sphene bands are developed (Basson, 2000). The pervasive presence of quartz-feldspar veins in the Ngubevu area has been the focus of precious and base metal mining efforts in the past and of this study. Two lithotypes of limited width and strike length are also recognisable in the area. They form three separate lenses of approximately 2–3-m-wide and 60-m-long, restricted between the dominant lithologies (Basson, 2000). These are calcite-quartz  $\pm$  tremolite schist and diopside-chlorite-sphene-calcite-albite-orthopyroxene  $\pm$  K-feldspar phyllite (Figure 2.7).

### 2.3.2. STRUCTURE AND DEFORMATION

The  $S_0$  syngenetic structure is preserved in the banded lithologies of the Ngubevu Area indicated by 2-mm-thick bands of talc, graphite, sericite and tourmaline (Basson, 2000). The first folding event ( $F_1$ ) is preserved in the epidote-actinolite and chloritic schists and has well-preserved fold axes that plunge towards the southeast at shallow to moderate angles with an average plunge/azimuth of  $45^\circ/121^\circ$  (Basson, 2000). The primary banding in the lithologies remained unaffected by the  $F_1$  folds and was only deformed during  $D_2$  by  $F_2$  through crenulation/kink folding (Basson, 2000). Basson (2000) interpreted this to imply that the  $S_0$  banding is, in fact,  $S_1$  and referred to it as  $S_{01}$ .

$S_1$  is denoted by actinolite, mosaic-textured graphite, quartz, and albite in the epidote-actinolite schist, while  $S_{01}$  is denoted by the highly sheared margins of lithologies that lack lineations (Basson, 2000). The  $S_1$  orientations digitised from Basson (2000) (Figures 2.8A and B) using the right-hand-rule for orientation indicate approximately E–W and ESE–WNW trends at/around the Golden Eagle (average dip/strike of  $69^\circ/088^\circ$ ) and Champion Mines (average dip/strike of  $60^\circ/079^\circ$ ). These are consistent with N–NE-directed regional thrust tectonics during the first deformational phase,  $D_1$  (Basson et al., 2005; McCourt et al., 2006; Bisnath et al., 2008).

The lensoidal shape and abrupt margins of the lithologies hosted in the epidote-actinolite-quartz-talc  $\pm$  calcite schist resulted from sheath folding during N–NE-directed shearing (Basson, 2000).  $F_3$  fold axes have not been directly observed in the field; however, Basson (2000) recorded a significant spread in  $S_{01}$  data on equal area stereonet from which he made an inference of the presence of  $F_3$  folds.

The orientation of veins ( $V_1$ ) formed during  $D_1$  closely resembles the orientation of the  $S_{01}$  planar foliation and margins of lensoid lithologies of the Mfongosi Group (Figures 2.8C and D), with vein material including quartz, feldspar and actinolite often with chlorite and sericite at the margins (Basson, 2000; Basson et al., 2005). These veins resulted from the infilling and resultant deformation of  $F_1$  shears and tension fractures (Basson, 2000; Basson et al., 2005).

The second deformational event,  $D_2$ , was syn- to late-tectonic and resulted from left-lateral transpression accommodated in the epidote-actinolite schist as a planar foliation ( $S_2$ ) and did not obliterate  $S_{01}$  (Basson, 2000; Basson et al., 2005). The  $S_{01}$  and  $S_2$  foliations form acute angles that vary, in the micro-scale, across the left-lateral system (Basson, 2000).  $D_2$  in the banded lithologies is indicated by kinking and crenulations with axes highly inclined to  $F_1$ ;  $F_2$  intrafolial fold axes plunge towards the southwest at an average plunge/azimuth of  $52^\circ/230^\circ$  (Basson, 2000).

$D_3$  is expressed by the refolding of  $F_1$  during continued  $D_2$  sinistral motion throughout the Mfongosi Group schist and involved the intensification of  $S_2$  in the epidote-actinolite schist and kinking of the finely banded lithologies (Basson, 2000; Basson et al., 2005). The final deformation event ( $D_4$ ) occurred during transtension, which generated tension fractures with an average dip/strike of  $67^\circ/196^\circ$  (Basson, 2000).

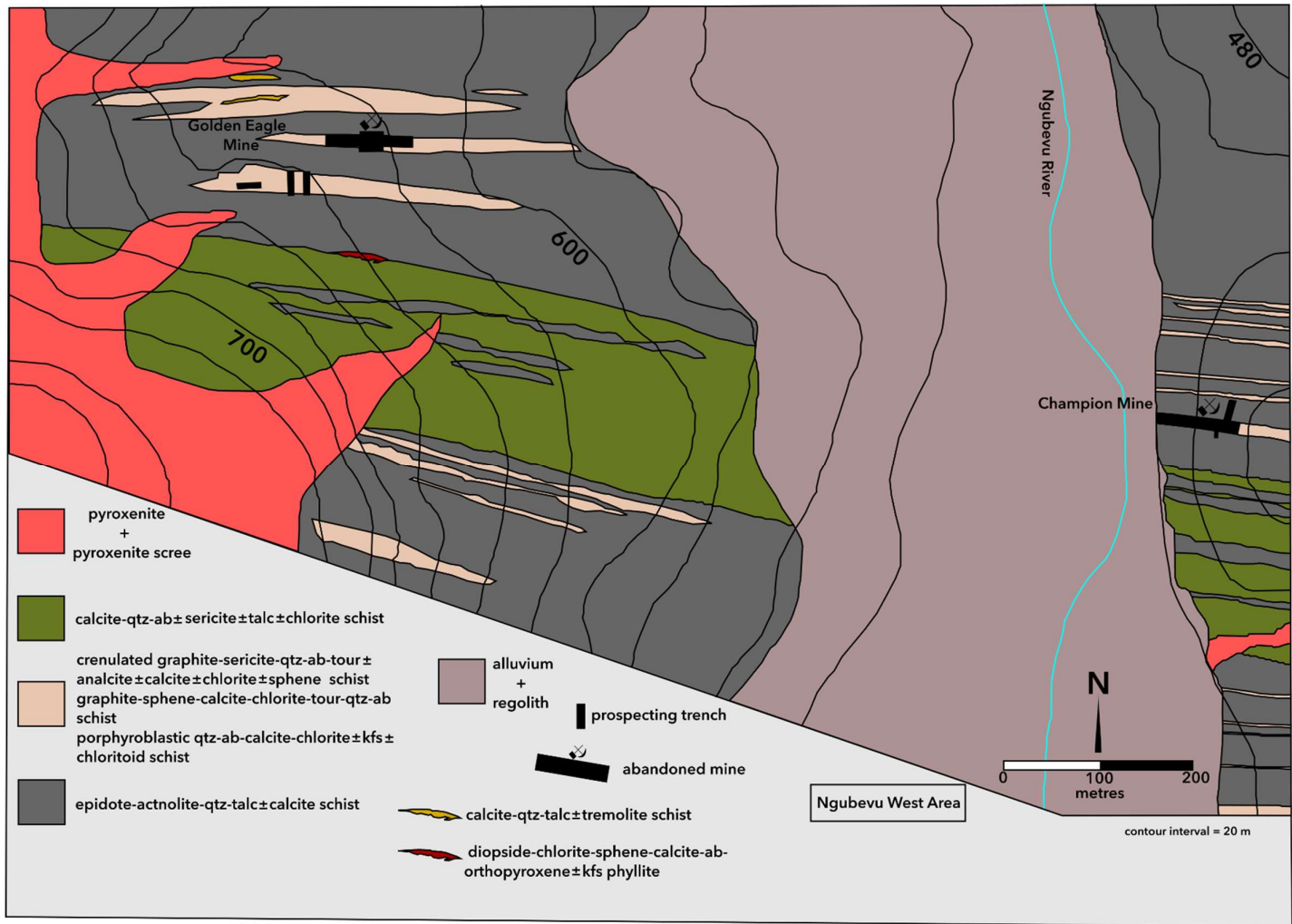


Figure 2.7: Lithological map of the Ngubevu West Area (modified from Basson, 2000), displaying the locations of the mines according to local guides and to regional Geological Map Sheet 2830DA of Collessie. Abbreviations: qtz – quartz, ab – albite, tour – tourmaline, kfs – K-Feldspar.

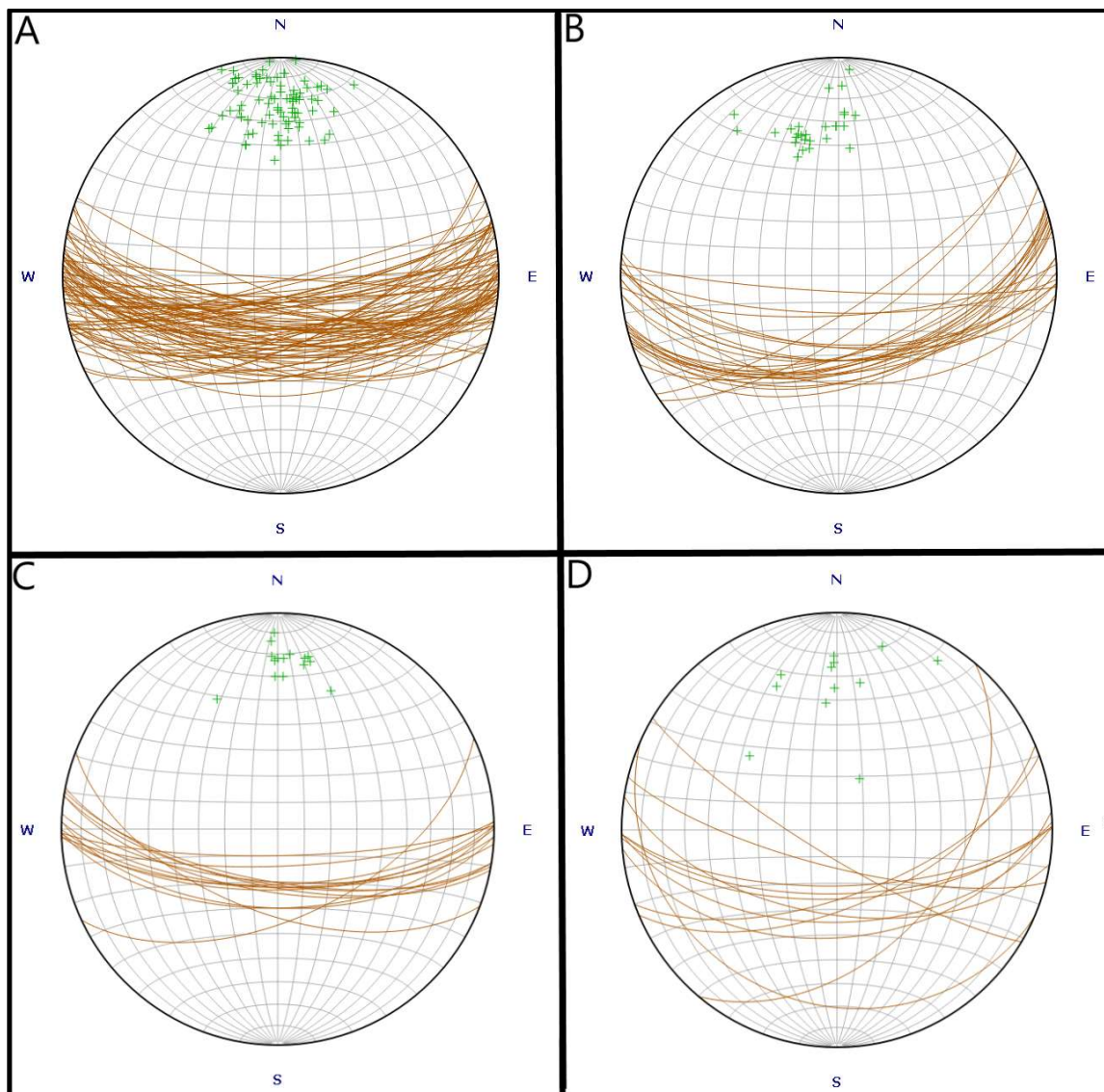


Figure 2.8: Equal area stereonet plots of  $S_1$  planar foliations in the Ngubevu West Area for (A) Golden Eagle Mine area, (B) Champion Mine area, (C)  $V_1$  veins in the Golden Eagle mine area and (D)  $V_1$  veins in the Champion Mine area. These data were digitised from maps in Basson (2000). The beta planes in (A) and (B) represent foliation planes while the crosses represent poles to the foliation planes. The beta planes in (C) and (D) represent veins while the crosses represent poles to the veins.

The last generation of veins ( $V_2$  and  $V_3$ ) occurred during early- to late-tectonic times, and they vary in width from 0.5 mm to 2–4 cm (Basson, 2000; Basson et al., 2005). The earlier-formed veins ( $V_2$ ) form fishhook and rootless folds in the limbs of  $F_1$  folds with thinned limbs lying parallel to  $S_{01}$  due to rotation during transcurrent shearing, the fold axes ( $F_4$ ) of these folded veins lie in the plane of the  $S_1$  foliation in the schist and are vertically inclined (Basson, 2000; Basson et al., 2005). The later veins ( $V_3$ ) have sub-vertical to vertical inclinations and often show antitaxial quartz fibre growth and cross-cut  $F_1$ ,  $F_2$  and  $F_3$  folds

(Basson, 2000; Basson et al., 2005). These veins are related to D<sub>4</sub> post-thrusting collapse and lateral extension (Basson, 2000).

#### **2.4. MINERALISATION**

Mineralisation in the NMP includes shear-zone-hosted precious metal deposits in all terranes, massive to semi-massive sulphides and magmatic ores in the Tugela Terrane, and metasomatic skarn deposits in the Margate Terrane (Thomas et al., 1990; Thomas et al., 1992; Bullen et al., 1994). Most of the mineral deposits in the NMP are hosted in the Natal Thrust Front and Nappe Complex of the Tugela Terrane, with a progressive southward decline in mineralisation into the Mzumbe and Margate Terranes (Thomas et al., 1990; Bullen et al., 1994).

Mineralisation in the Tugela Terrane is divided into three key groups (Thomas et al., 1990):

1. Precious and base metal mineralisation in shear zones, including epigenetic gold, hosted in the first generation of quartz veins (V<sub>1</sub>) within shear zones of the Mfongosi Group in the Natal Thrust Front, the focus of this research, and in the Tugela Group in the Natal Nappe Complex.
2. Gold-bearing massive sulfidic ores in the i'Thuma area within rocks of the Tugela Group.
3. Magmatic mineralisation. This group contains Alpine-type ultramafic bodies (Cr, Cu, Ni), layered mafic/ultramafic bodies (Cr, Cu-Ni, Fe, V, Ti) and lesser Nb, Y and rare earth element (REE) mineralisation within alkaline and peralkaline bodies.

The thrusts and shear zones formed during D<sub>1</sub> collisional orogeny at ca. 1.1 Ga posed as pathways for upwelling gold-bearing solutions, with the result that the ultimate positioning of precious and base metal mineralisation (V<sub>1</sub>) is controlled by the rock structure and, thus, compatible with postulated models of the development of the NMP (Thomas et al., 1990). However, late-formed, unaltered quartz veins (V<sub>2</sub> and V<sub>3</sub>) containing carbonate do occur and present minor quantities of gold – approximately 20 ppb (Thomas et al., 1990; De Klerk, 1991; Bullen et al., 1994).

The shear-zone-hosted precious and base metal mineralisation in the Tugela Terrane has been divided into two sub-groups (Thomas et al., 1990; Bullen et al., 1994): (1) deposits that occur within the Natal Thrust Front in mafic and pelitic schists from the Mfongosi Group that have undergone shearing (Ngubevu and Mfongosi areas); and (2) deposits that occur within the Natal Nappe Complex in amphibolites of the Tugela Group – Phoenix Mine and Mpalala Goldfield. The metal deposits in the thrust front are considered to have formed from volcanic exhalative activity before the onset of deformation, with additional modification and concentration through shearing and metamorphism during  $D_1$  (De Klerk, 1991).

#### *2.4.1. Ngubevu Area*

The Ngubevu area is set in the broadest part of the Natal Thrust Front. It initially consisted of 11 claims, four of which were established into small mines (Thomas et al., 1990; Bullen et al., 1994). Mineralisation in the Ngubevu area is found in the sheared schists of the Mfongosi Group, which comprise greenschist facies metalavas and schistose metargillites (Thomas et al., 1990; Bullen et al., 1994). The metalavas contain a weak to pervasive late carbonate alteration that exists as patches of fine to medium grained calcite and disposed parallel to the foliation, or thin carbonate veins discordant to the foliation that are most concentrated in intense zones of shearing and post-date the mineralisation (Thomas et al., 1990).

Graphitic schists are characteristically developed along boundaries between metalavas and metapelites or confined with the metasediments in the Ngubevu area with the layers containing several metre thick zones of intense carbonation, which is associated with sericite and quartz, with tourmaline occurring as fine grains and locally comprising 20% of the rock – forming tourmalinites (Thomas et al., 1990; Bullen et al., 1994). Disseminated pyrite, pyrrhotite, cubanite, chalcopyrite and sphalerite occur in these graphitic zones but are predominantly barren of gold (Bullen et al., 1994). Researchers suggest that later, epigenetic precious metal mineralisation hosted in shear zones ( $V_1$ ) might have been sourced from a syngenetic, strata-bound, exhalative protore that was rich in tourmaline during  $D_1$  (Thomas et al., 1990).

Mineralisation at all previous workings comprises late epigenetic discontinuous gold-rich quartz veins and stringers ( $V_1$ ) of approximately 3-cm-thickness, containing up to ~7000 ppb Au and confined to nearly E–W-striking zones of intense shearing (Thomas et al., 1990; Bullen et al., 1994). These gold-bearing quartz veins and stringers ( $V_1$ ) post-date a primary stage of barren, pre-tectonic ( $D_0$ ) and extremely distorted quartz veins but pre-date carbonate alteration (Bullen et al., 1994). These barren quartz veins are unspecified in terms of their position in the deformation and veining history of the thrust front and are here referred to as  $V_0$  because they were formed before deformation and were deformed by widespread tectonism in the Natal Thrust Front/Tugela Terrane (Thomas et al., 1990; Bullen et al., 1994).

## **2.5. CONCLUDING REMARKS**

The Tugela Terrane has experienced several deformation events, some of which, like the initial deformation event  $D_1$ , have prepared the ground for epigenetic precious, massive sulfidic and magmatic mineralisation. This study is focused on the epigenetic precious and base metal mineralisation within the Natal Thrust Front, in the Ngubevu area, in rocks of the Mfongosi Group.

## **CHAPTER 3: RESEARCH METHODOLOGY**

### **3.1. LOCAL-SCALE DATABASE COMPILATION**

The local-scale database for this study was compiled from an existing map of the structure and geology of the Ngubevu West area (Basson, 2000), where the precious and base metal mines of interest are located. This map was georeferenced in the Integrated Land and Water Information System (ILWIS) Geographic Information System (GIS) software. From the georeferenced map, orientations of  $S_1$  foliation and  $V_1$  veins in the area were digitised, as these are the posited controls on epigenetic shear zone-hosted mineralisation in the area (Thomas et al., 1990; Bullen et al., 1994; Basson, 2000). The trends of these features were then plotted as rose diagrams using the GeoRose software for comparison with field structural measurements of the same features collected during this research. In addition, the lithology and occurrences of mines and prospects in the area were digitised as well.

### **3.2. SAMPLE COLLECTION AND LABORATORY PREPARATION**

Quartz-feldspar vein material and host rock samples were collected from the Golden Eagle and Champion mines and prospect sites in the Ngubevu area following the methodology outlined in Hansen (1990) for the collection of oriented rock samples. This was important for the proper and representative analysis of trends in distributions of structures and mineral deposits in the micro-scale. Before marking and extracting each sample, the rock outcrop was examined whether it was *in situ* or not. From an *in situ* rock outcrop, the structural attitude of each sample was measured along a foliation plane using the right-hand rule. The measured attitude was recorded with an indelible marker on the top/foliation surface before sample extraction (Figure 3.1). The bottom and sides of each sample were also recorded. The GPS coordinates of each sample were recorded in a field notebook before sample extraction. This procedure was followed, as it is important for the proper analysis of ore-controlling structures at the micro- to-local-scales. That is because trends of mineral orientations at the micro-scale can be related to fractures mapped at the micro-scale and to structures depicted on existing geological maps in order to infer regional structural controls based on the analysis of micro-fractures (cf. Laing, 2004).

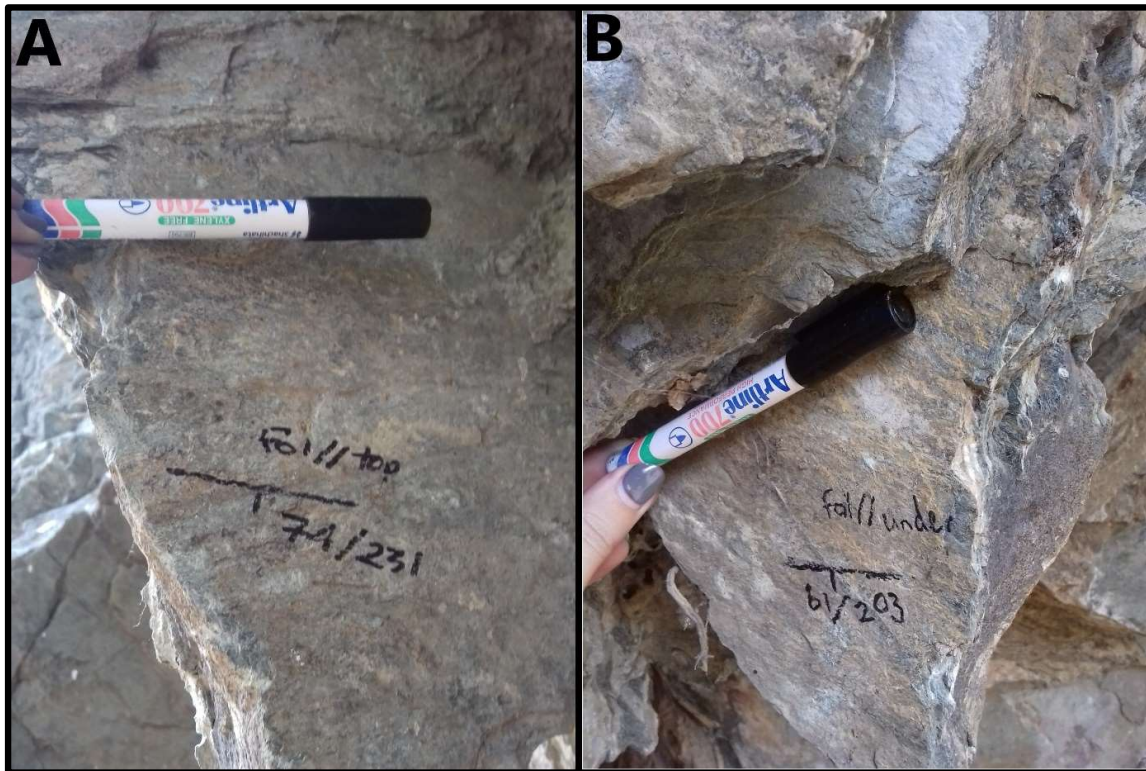


Figure 3.1: Oriented samples measured from an outcrop before extraction. Measurements of planar surface attitudes are marked on (A) top foliation surface and (B) bottom foliation surface.

In the laboratory, each oriented rock slab sample was placed in a sandbox according to its original field orientation and markings. The orientation of a sample in the field, measured as dip and dip direction using the right-hand rule, was applied in the laboratory to re-orientate the samples before sectioning. Each sample was wrapped with a rubber band along the interface of the sand surface and the sample to help outline the horizontal plane (Figure 3.2) (Hansen, 1990). This was done so that (a) every sample was cut along a horizontal plane with respect to the dip of the structure measured from the sampled field outcrop, (b) representative and precise mapping and interpretation of trends in the micro-fractures of oriented samples are guaranteed with respect to structural data published in the literature, and (c) accurate mapping and interpretation of ore mineral trends are guaranteed with respect to mapped micro-fractures and local-to-regional-scale structures published in the literature.

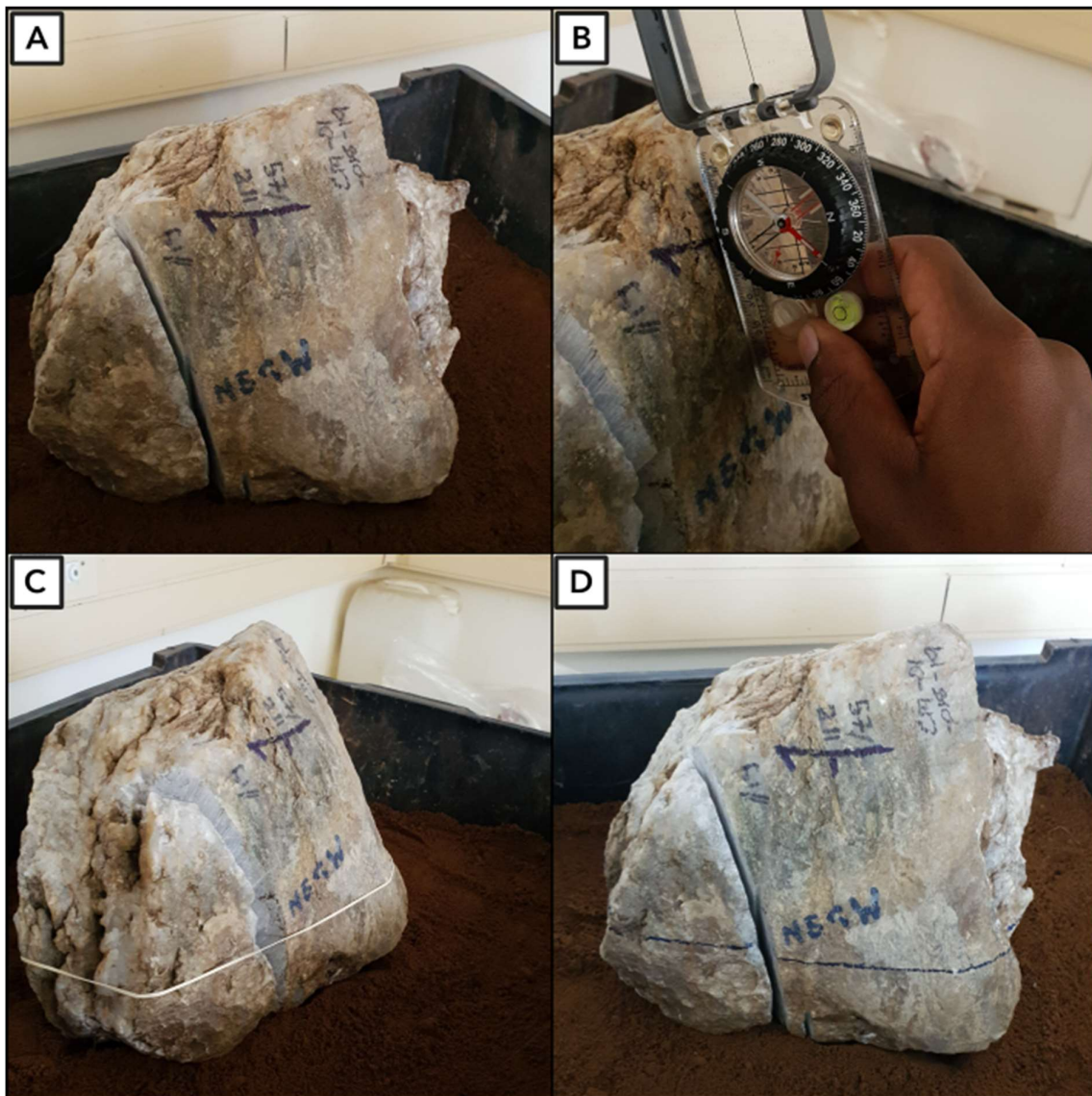


Figure 3.2: Procedure for reorienting a sample in the laboratory. (A) A sample is placed in a sandbox filled with fine beach sand. (B) The sample is oriented to its original dip. (C) The sand surface is ensured to be horizontal, and a rubber band is wrapped around the sample parallel to the horizontal sand surface; this marks the line of zero dip. (D) A line following the rubber band is marked with an indelible marker to prevent it from being washed away to the cutting process.

After sectioning along the horizontal plane, each sample thin section chip was marked to indicate the top and bottom surfaces, and a slit representative of the general N direction of the sample was made to maintain invariably its orientation during thin sectioning (Figure 3.3) (Hansen, 1990). The prepared rock chips were then made into polished thin sections with uniform thickness of 30  $\mu\text{m}$  at a laboratory in the University of the Witwatersrand.

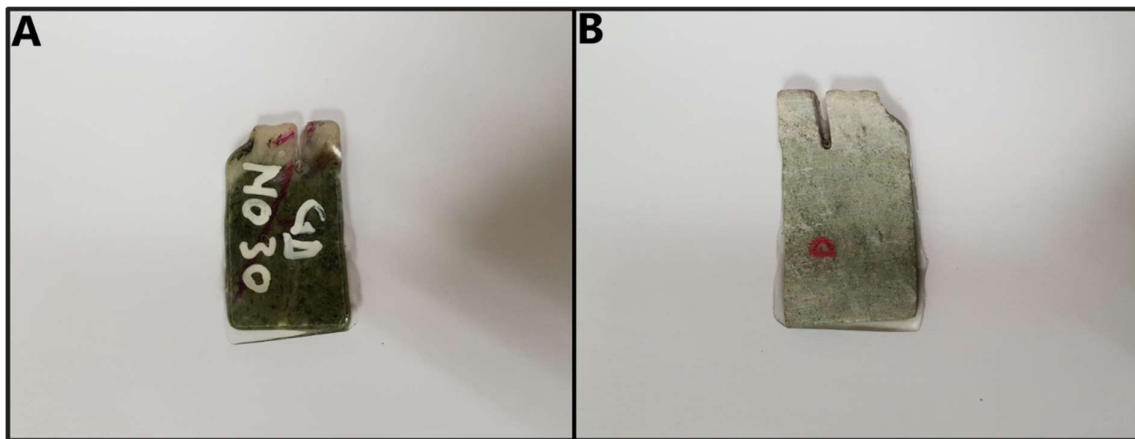


Figure 3.3: Rock chips permanently oriented and prepared for thin sectioning. (A) Top surface of the thin section and (B) mounting/cut surface of the thin section.

### 3.3. MICRO-SCALE MAPPING OF FRACTURES AND ORE MINERAL CENTROIDS

Micro-fractures in the oriented thin sections of quartz-feldspar veins and/or schist host rocks sampled from the Golden Eagle and Champion mine areas were mapped under low magnification in plane polarised light using a Leica DM 750P microscope to ensure consistency of scale throughout the analogue mapping process. To map the centroids of ore minerals, the microscope was then switched to reflected light to facilitate viewing of these opaque minerals. To allow controlled mapping of the thin sections, each thin section was held on the microscope stage using a stage goniometer which allowed incremental X-Y movements of each thin section across the stage. The centroid of each ore mineral was established as the intersection of its long and short axes.

Analogue maps of micro-fractures and ore minerals were created on A4 size paper using an enlarged 7.5 cm x 13.5 cm image expanded from the original thin section dimensions of 2.5 cm x 4.5 cm. This was done to facilitate accurate mapping of all observed micro-fractures and ore minerals in a conveniently small area. All of the mapped ore minerals in the collected samples were sphalerite grains because they were the most abundant in the micro-scale.

### 3.4. DIGITISATION OF MICRO-FRACTURES AND ORE MINERALS

The maps of thin sections with outlines of samples, micro-fractures and ore mineral centroids were raster-scanned. The scanned images were then rotated and saved in their

measured field orientations as recorded during sampling and then imported into ILWIS 3.3 GIS software for georeferencing. The lower-left corner of an oriented thin section image was georeferenced with GPS coordinates corresponding to the sample site. The three other corners were georeferenced with coordinates calculated using fitting trigonometric functions, the dimensions of the thin section and the measured azimuth orientation of the sample. The images were exaggerated using a 4.5 m length and 2.5 m width instead of the 4.5 cm length and 2.5 cm width of a thin section to facilitate viewing of oriented thin sections on a laptop computer (Figure 3.4A and B).

Micro-fractures on georeferenced raster-scanned analogue maps were then digitised in the GIS. In a GIS, the trend of a line segment is defined by its end nodes. The digitised line segments of micro-fractures were snipped (i.e., cut) at bends in order for them to be representative of all straight segment orientations contained in a line. In addition, long straight-line segments were snipped at approximately equal intervals defined by the shortest line segment so that all line segments were of roughly equal length. Then, in the GIS, data of the number of line segments and their trends were generated for the digitised micro-fractures of each oriented thin section.

To display and investigate the trends in micro-fractures, data of orientation and number of line segments representing micro-fractures digitised in ILWIS per sample were imported to Excel software. In Excel, the data were arranged such that the trend of a line segment matched the number of line segments with the same trend. Then, the data were exported to GeoRose software, where rose diagrams of the trends of digitised micro-fractures were plotted per sample. The results of the analysis of trends in micro-fractures are examined in Chapter 4.

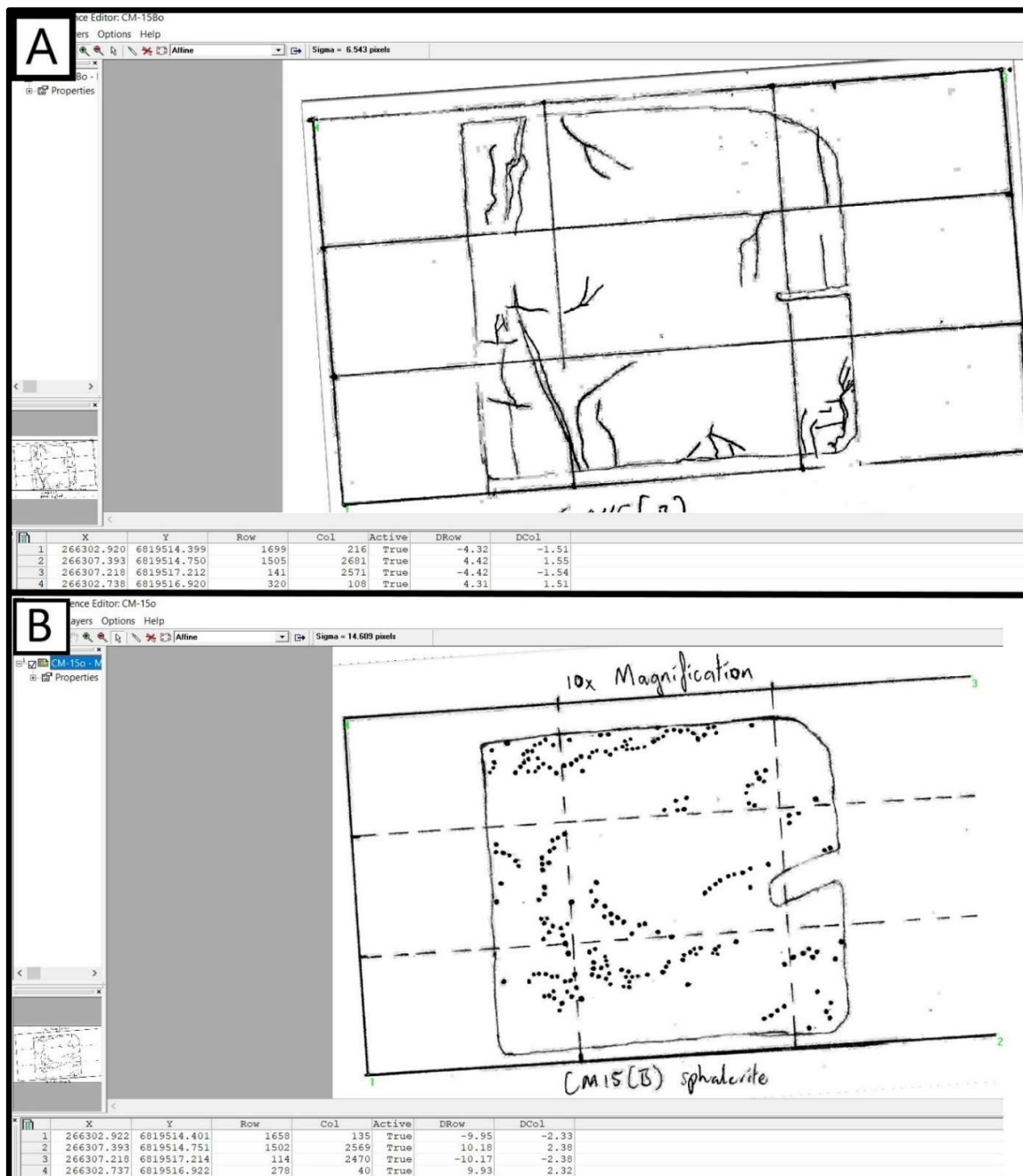


Figure 3.4: The Georeference editing window in ILWIS 3.3 showing the northing and easting coordinates of (A) sample CM-15B with micro-fractures and (B) sample CM-15B with ore mineral centroids.

Likewise, the centroids of ore minerals on georeferenced raster-scanned analogue maps were then digitised in the GIS. The point data of digitised ore centroids per sample were then studied using the spatial analytical techniques outlined in the following section.

### 3.5. SPATIAL ANALYSES

Various methods of spatial analysis were used in this study to generate and analyse data of trends in the georeferenced scanned images of ore mineral centroids. These methods are outlined below. The spatial analyses were carried out using ILWIS 3.3 GIS in combination with other freely available software packages, namely DotProc ([www.kuskov.com](http://www.kuskov.com)), ImageJ (<https://imagej.nih.gov/ij>) and EllipseFit ([www.frederickvollmer.com/ellipsefit](http://www.frederickvollmer.com/ellipsefit)). Rose diagrams of trends in the data were produced using GeoRose software ([www.yongtechnology.com](http://www.yongtechnology.com)).

#### 3.5.1. Point Pattern Analysis

Point pattern analysis was employed in this study to analyse measures of arrangement and dispersion in a spatial point pattern (cf. Carranza, 2009). In this study, a spatial point pattern is that of ore mineral centroids in a thin section of vein material sample. This analysis is important for understanding how the points are distributed and whether their distribution is regular, clustered or random, and what sort(s) of processes may have controlled their distribution.

In ILWIS, a table was created for the digitised ore mineral centroids per sample using the pattern analysis programme. This table reveals the probabilities of point occurrences within specified distances from each point in the thin section. By looking under the additional information tab of the 'properties' menu, two tables with information about the reflexive/reciprocal nearest neighbours and the distances to nearest neighbours were revealed for the points in the thin sections and for points assumed in a situation of complete spatial randomness. These data of point patterns of ore mineral centroids are analysed in Chapter 5.

#### 3.5.2. Fry Analysis

For the analysis of trends in the orientations of points in a point pattern, the Fry analysis method was employed (Fry, 1979). The data of X- and Y-coordinates of each point per thin

section derived by digitisation were used in DotProc where Fry plots per point data set were created.

The point coordinates were copied from ILWIS and converted into a text file using Microsoft Word and Excel. After conversion, the point coordinates were imported into DotProc for Fry analysis. It is known that Fry plot orientations for all points in a spatial pattern are sensitive (i.e., biased) to the geometry of the spatial pattern (Fry, 1979). For this study, the Fry plot trend of all points in a thin section will follow the trend of its length. To avoid this bias, only pairs of Fry points (i.e., two points determine a line, and thus a trend) separated by a distance with probability of just a single ore mineral centroid occurrence next to a neighbour ore mineral centroid were used to produce Fry plots. That distance was determined by point pattern analysis in ILWIS. The data of trends in the Fry plots were then exported to Excel, and rose diagrams were plotted for the data using GeoRose software. The Fry analysis in this research is discussed in Chapter 6.

### *3.5.3. Fractal Analysis*

To analyse the behaviour of points in a spatial point pattern, the box-counting fractal dimension analysis method was used (Mandelbrot, 1983) and it was implemented in ILWIS. The fractal analysis was employed beginning with a box size defined by a distance between pairs of ore mineral centroids in which there is a probability of only one ore mineral centroid occurrence next to a neighbour ore mineral centroid. That distance was determined by point pattern analysis in ILWIS.

The patterns of points were converted into rasters of up to only 5 m × 5 m box sizes, as the maximum length of the exaggerated images in the GIS was 4.5 m. This allowed for convenient sampling of the points at thin section scale. The number of points after each iteration beginning with a box size of 0.05 m × 0.05 m was noted down, and the data were plotted in Excel using logarithmic scale scatter plots. The plotted data were plotted in a log-log plot of point versus box size, and then fitted with regression lines with power functions. From these regression lines, the box-counting fractal dimension of each point pattern was obtained from the power function equation of a line for a monofractal pattern and power

function equations of two lines for a bifractal pattern. The fractal analysis in this research is discussed in Chapter 7.

#### *3.5.4. Shape Analysis*

To analyse the orientations of shapes of individual grains of a specific ore mineral in thin sections, they were photographed using a camera attached to the Leica microscope (Figure 3.5A). Three areas deemed to have ore minerals representative of a thin section were chosen by first browsing the thin section under the microscope, and then photographed.

The obtained image files were then converted into binary images using the ImageJ software by adjusting the brightness in the colour threshold. This was done to ensure that low brightness areas containing gangue minerals were blacked out and only the high brightness areas occupied by ore minerals (i.e., sphalerite grains) were left. The obtained images were then inverted and converted to binary images (Figure 3.5B).

Binary images of each thin section were imported into EllipseFit, where the ore minerals were fitted with ellipses (Figure 3.5C). Because an ellipse has one short axis and one long axis that help define its orientation, the preferential trends of the ore mineral grains are defined by the orientation of the long axis of the ellipse. Orientation data obtained from EllipseFit were transposed to Excel. However, EllipseFit uses E–W (not N–S) as reference for orientation. Therefore, to align the data to N–S orientation and to ensure consistency with the other orientation data, 90° was added to each orientation measured by EllipseFit. From the shape orientation data, rose diagrams were plotted using GeoRose (Figure 3.5D). The shape analysis in this research is discussed in Chapter 8.

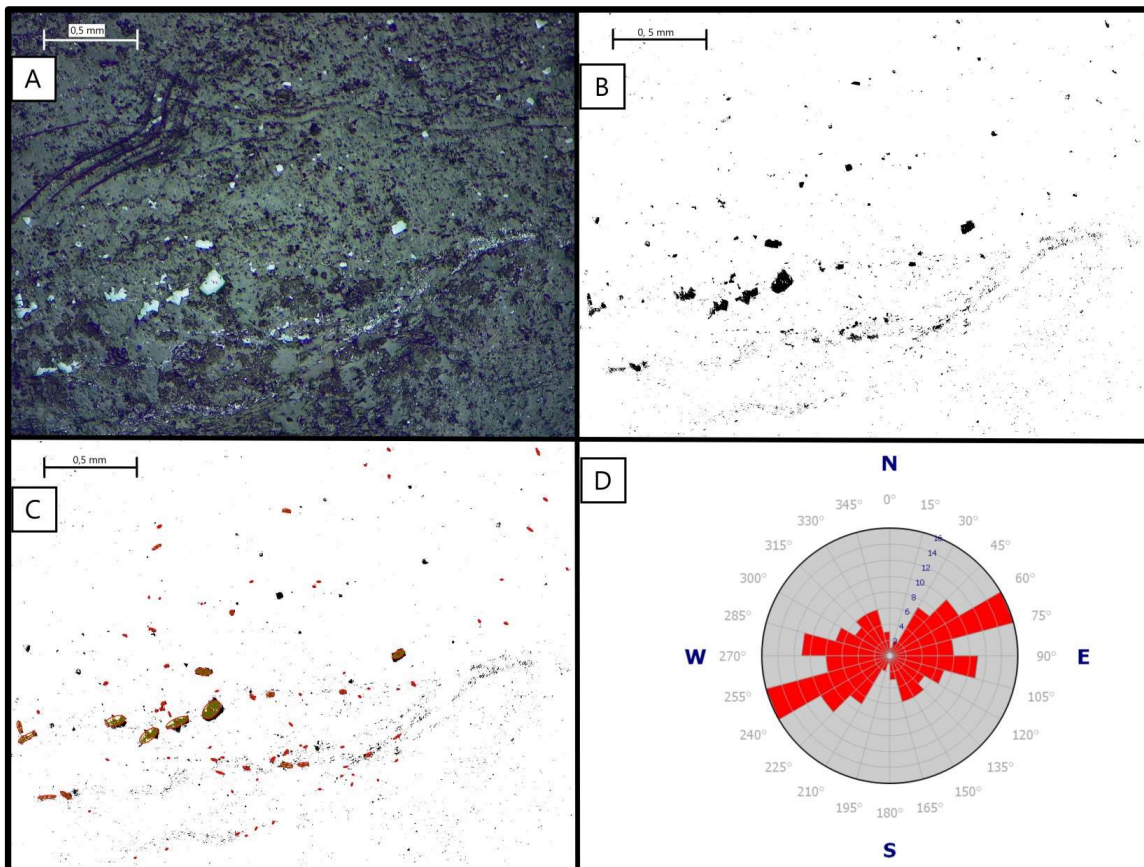


Figure 3.5: The workflow procedure for obtaining the trends in the shapes of ore minerals. (A) Original image captured with a camera attached to a Leica microscope under reflected light. (B) Binary image of ore minerals (sphalerite) in the image obtained using ImageJ. (C) Ellipses fitted automatically to selected ore minerals in EllipseFit. Only minerals with unequal axes were selected and fitted with ellipses as equal sided shapes would produce circles. (D) Rose diagram plotted with GeoRose for trends of major axes of ellipses fitted to ore mineral shapes. All the images above are from sample CM-04.

### 3.6. CONCLUDING REMARKS

Descriptions and rationales of the spatial analytical techniques (point pattern analysis, Fry analysis, fractal analysis and shape analysis) used in this study for the characterisation of the trends of ore minerals are provided in the respective chapters that follow. Because the micro-fractures and point data analysed in the following chapters of this research are represented in two-dimensions (i.e., the mapping plane), the orientations of the relative stresses affecting them can only be described by the relative stress magnitudes, namely  $S_v$ ,  $S_{Hmax}$  and  $S_{Hmin}$  (cf. Mizuno et al., 2005; Giner-Robles et al., 2012; Niu et al., 2020) which are related to the style of faulting active in a region (Zoback, 2010).  $S_v$  is the vertical stress,  $S_{Hmax}$  is the maximum horizontal stress, and  $S_{Hmin}$  is the minimum horizontal stress

(Zoback, 2010). The horizontal stresses,  $S_{Hmax}$  and  $S_{Hmin}$ , may be greater than, or less than  $S_v$ , depending on the geological setting (Zoback, 2010). The interpreted results of microfracture orientations and two-dimensional stress orientations were then compared with trends of the point data to deduce structures that were permissive for mineralisation in the Golden Eagle and Champion mines of the Ngubevu area. The results from the microfractures were also compared with existing data from Basson (2000) and other literature (e.g., Basson and Watkeys, 2003; Basson et al., 2005; McCourt et al., 2006, Bisnath et al., 2008) about the local/regional stresses that affected the Natal Thrust Front during its development.



## **CHAPTER 4:**

### **ANALYSIS OF MICRO-FRACTURES**

Examination of micro-fractures may help geologists in their quest to understand the local and regional paleostress/evolution of a geological terrane, the differences between laboratory-generated and natural fractures, the micromechanics of fracture and fault propagation, and the passageways of fluids through rocks in certain districts (Kranz, 1983; Anders et al., 2014). In this research, micro-fractures were studied with the aim of understanding the micro-scale stress field orientation and controls on precious and base metal mineralisation in the Ngubevu West area. These were then compared to the known local- and regional-scale stress field of the Tugela Terrane/Natal Metamorphic Province.

Micro-fractures or micro-cracks are lensoidal or tabular fractures along which there is no displacement (Mode I) and have dimensions so minute that they can only be viewed with the help of an optical microscope (van der Pluijm and Marshak, 2004; Anders et al., 2014). They result from the application of differential stress to a rock (Anders et al., 2014). Fractures in rocks are often suitable passageways for fluids and gases to enter and be trapped during cementation or closure of the fracture (Anders et al., 2014), thereby allowing the precipitation of dissolved metals from solution.

It is important to note that fractures that develop during folding may propagate in a variety of orientations not coincident with the orientation of the maximum principal stress (Watkins et al., 2015). Moreover, fracturing may be influenced by other factors such as rock type (Hoek and Brown, 1980; Mighani et al., 2016), rock fabric (Ghazvinian et al., 2014) and mineralogy (Lu et al., 2020) such that the orientation of the type of fractures developed in a rock may be at an angle to the maximum principal stress. Furthermore, there are three recognised modes of fracturing, namely (1) Mode I – fractures with no displacement, (2) Mode II – shear fractures along which there is displacement, and (3) Mode III – mixed mode fractures that are a combination of Modes I and II (Nicholson and Pollard, 1985; van der Pluijm and Marshak, 2004). These different modes of fractures may also form in a variety of propagation paths and larger fractures may form by linkage of different fractures during propagation (Nicholson and Pollard, 1985; Laubach, 1989; Anders et al., 2014). The

interpretation of fractures in this study as Mode I is based as there were no visible displacements along the fractures.

A variety of micro-fracture types (Simmons and Richter, 1976; Kranz, 1983) may be observed in rocks, and these are grain boundary cracks/fractures (between grains), intracrystalline cracks/fractures (within a single grain) and intercrystalline or transgranular cracks (from one grain boundary to the next across two or more grains). These micro-fracture types were all mapped from the samples of oriented quartz-feldspar veins and host rock from the Golden Eagle and Champion Mine areas. There was a notable dominance of intercrystalline and transgranular micro-fractures in the study area.

The oriented thin sections in this study were cut from and they are representative of the horizontal plane, i.e., the mapping plane. It follows that the rose diagrams generated for the trends in micro-fracture orientations allow for the inference of the local stress field that affected samples whilst in situ based on the maximum horizontal stress (SHmax) and the minimum horizontal stress (SHmin) (Zoback, 2010). These stresses are mutually perpendicular to each other (cf. Morley, 2010; Carafa and Barba, 2013; Velandia et al., 2020). Under compressional stresses, fractures/cracks in rocks will propagate in the direction parallel to the maximum compressive stress axis (van der Pluijm and Marshak, 2004; Zhong et al., 2015). Therefore, the most preferred orientation of micro-fractures visible in the rose diagrams of oriented thin sections in this study was interpreted to be SHmax, and the orientation orthogonal to that, in the horizontal plane, is SHmin.

## **4.1. RESULTS**

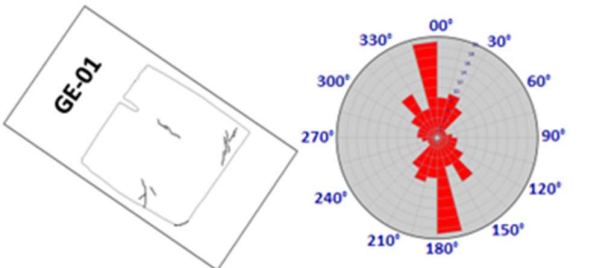
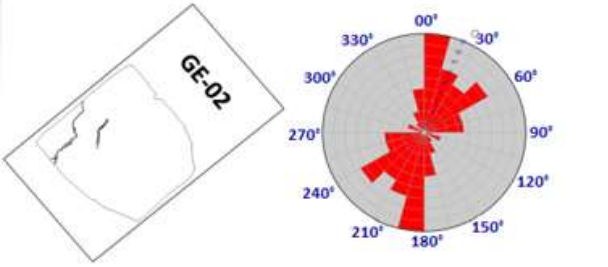
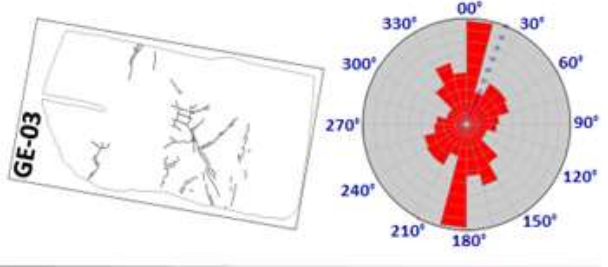
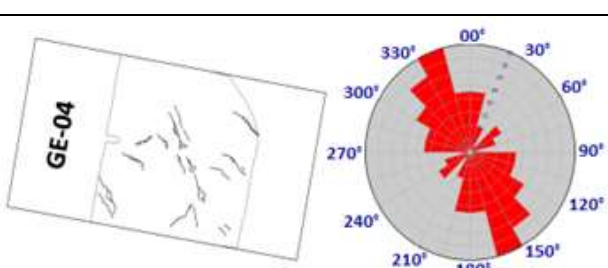
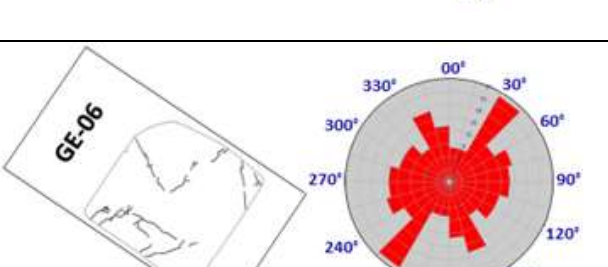
### *4.1.1. Golden Eagle*

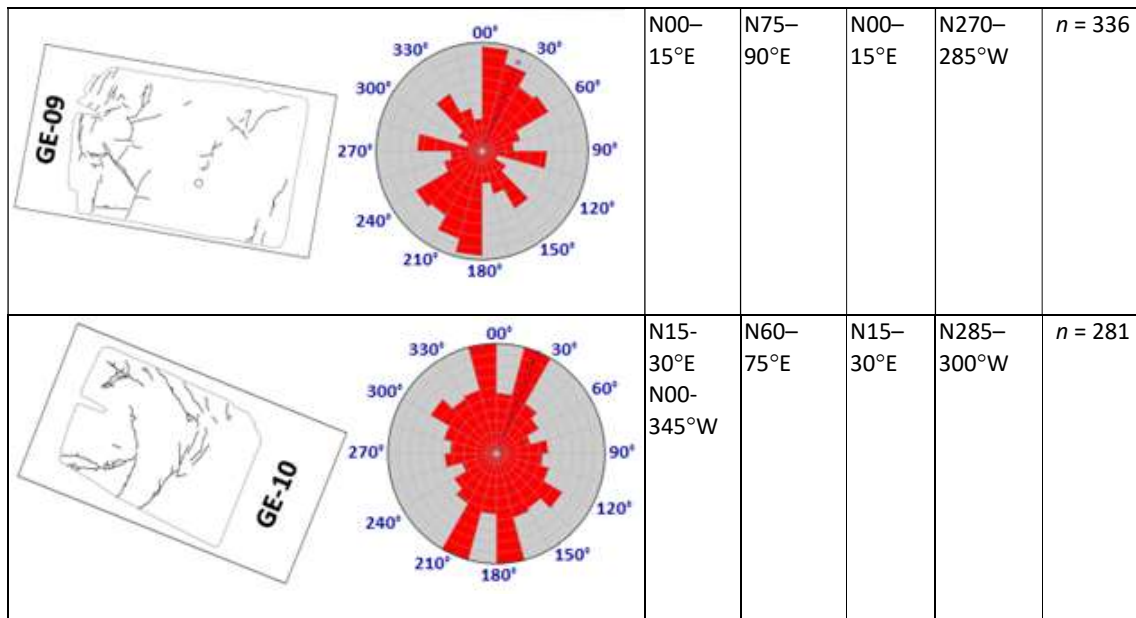
Based on the major and minor trends in the micro-fractures' orientations in sample GE-01 (Table 4.1), the interpreted SHmax was oriented towards N00°–345°W, and SHmin was oriented towards N75°–90°E. Based on the major and minor trends in the micro-fractures' orientations in sample GE-02 (Table 4.1), the interpreted SHmax was oriented towards N00°–15°E, and SHmin was oriented towards N270°–285°W. Based on the major and minor trends in the micro-fractures' orientations in sample GE-03 (Table 4.1), the interpreted SHmax was oriented towards N00–15°E, and SHmin was oriented towards N270°–285°W. Based on the

major and minor trends in the micro-fractures' orientations in sample GE-04 (Table 4.1), the interpreted SHmax was oriented towards N330–345°W, and SHmin was oriented towards N60°–75°E. Based on the major and minor trends in the micro-fractures' orientations in sample GE-06 (Table 4.1), the interpreted SHmax was oriented towards N30°–45°E, and SHmin was oriented towards N300°–315°W.

Based on the major and minor trends in the micro-fractures' orientations in sample GE-09 (Table 4.1), the interpreted SHmax was oriented towards N00°–15°E, and SHmin was oriented towards N270°–285°W. Based on the major and minor trends in the micro-fractures' orientations in sample GE-10 (Table 4.1), the interpreted SHmax was oriented towards N00°–15°E, and SHmin was oriented towards N285°–300°W.

Table 4.1: Interpretations of micro-fracture data from the Golden Eagle mine area and prospect site.

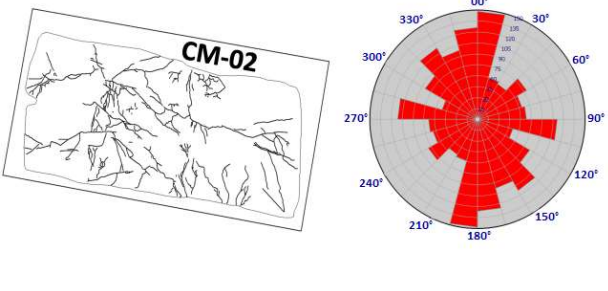
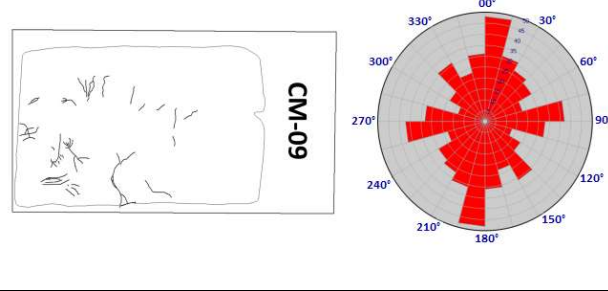
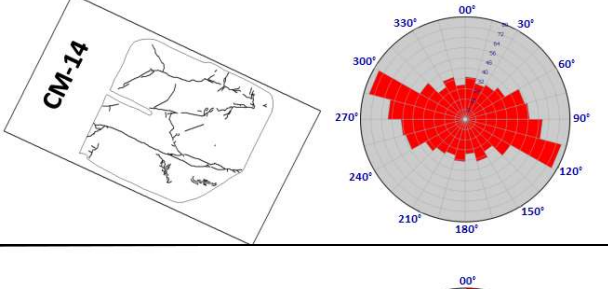
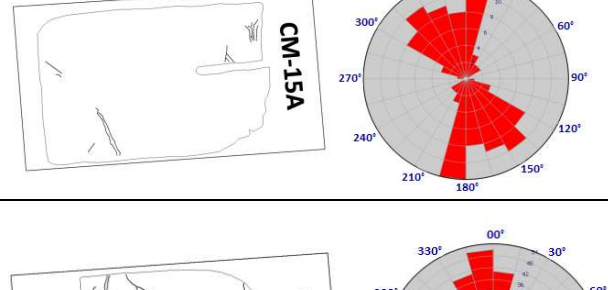
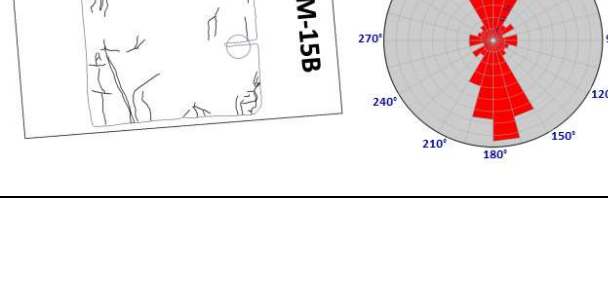
N-oriented rock thin section & rose diagram of trends of micro-fractures	Observed axes		Interpreted stress orientations		n value
	Major	Minor	SHmax	SHmin	
	N00– 345°W	N75– 90°E	N00– 345°W	N75– 90°E	n = 76
	N00– 15°E	N75– 90°E	N00– 15°E	N270– 285°W	n = 84
	N00– 15°E	N75– 90°E	N00– 15°E	N270– 285°W	n = 208
	N330– 345°W	N60–75°E	N330– 345°W	N60– 75°E	n = 191
	N30– 45°E	N15– 30°W	N30– 45°E	N300– 315°W	n = 148

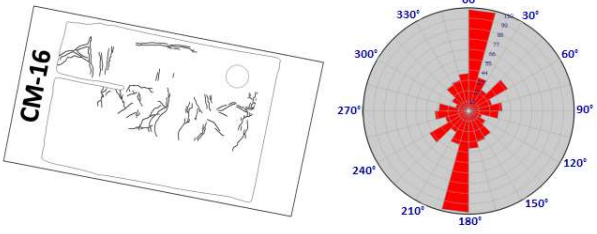
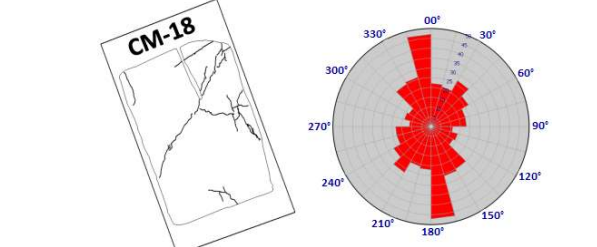
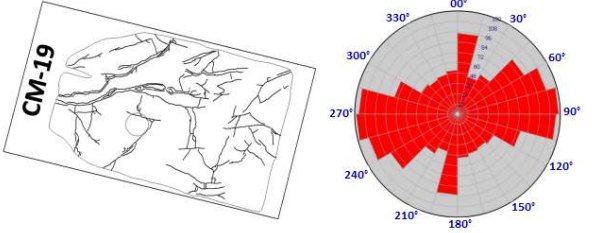
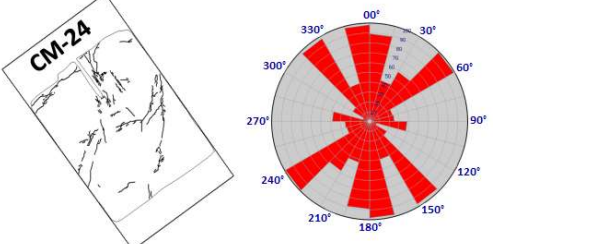


#### 4.1.2. Champion Mine

Based on the major and minor trends in the micro-fractures' orientations in sample CM-02 (Table 4.2), the interpreted SHmax was oriented towards N00°–15°E, and SHmin was oriented towards N270°–285°W. Based on the major and minor trends in the micro-fractures' orientations in sample CM-09 (Table 4.2), the interpreted SHmax was oriented towards N00°–15°E, and SHmin was oriented towards N270°–285°W. Based on the major and minor trends in the micro-fractures' orientations in sample CM-14 (Table 4.2), the interpreted SHmax was oriented towards N285°–300°W, and SHmin was oriented towards N15°–30°E. Based on the major and minor trends in the micro-fractures' orientations in sample CM-15A (Table 4.2), the interpreted SHmax was oriented towards N00°–15°E, and SHmin was oriented towards N270°–285°W. Based on the major and minor trends in the micro-fractures' orientations in sample CM-15B (Table 4.2), the interpreted SHmax was oriented towards N00°–345°W, and SHmin was oriented towards N75°–90°E. Based on the major and minor trends in the micro-fractures' orientations in sample CM-16 (Table 4.2), the interpreted SHmax was oriented towards N00°–15°E, and SHmin was oriented towards N270°–285°W. Based on the major and minor trends in the micro-fractures' orientations in sample CM-18 (Table 4.2), the interpreted SHmax was oriented towards N00°–345°W, and SHmin was oriented towards N75°–90°E.

Table 4.2: Interpretations of micro-fracture data from the Champion mine area and prospect site.

N-oriented rock thin section & rose diagram of trends of micro-fractures	Observed axes		Interpreted stress orientations		n value
	Major	Minor	SHmax	SHmin	
	N00– 15°E	N45– 60°E	N00– 15°E	N270– 285°W	n = 1053
	N00– 15°E	N270– 285°W	N00– 15°E	N270– 285°W	n = 334
	N285– 300°W	N00– 15°E	N285– 300°W	N15– 30°E	n = 441
	N00– 15°E	N285– 300°W	N00– 15°E	N270– 285°W	n = 58
	N00– 345°W	N75– 90°E	N00– 345°W	N75– 90°E	n = 228

	N00– 15°E	N75– 90°E	N00– 15°E	N270– 285°W	<i>n</i> = 438
	N00– 345°W	N270– 285°W	N00– 345°W	N75– 90°W	<i>n</i> = 258
	N75– 90°E	N15– 30°E	N75– 90°E	N00– 345°W	<i>n</i> = 875
	N45– 60°E	N75– 90°E	N45– 60°E	N315– 330°W	<i>n</i> = 617

Based on the major and minor trends in the micro-fractures' orientations in sample CM-19 (Table 4.2), the interpreted SHmax was oriented towards N75°–90°E, and SHmin was oriented towards N00°–345°W. Based on the major and minor trends in the micro-fractures' orientations in sample CM-24 (Table 4.2), the interpreted SHmax was oriented towards N45°–60°E, and SHmin was oriented towards N315°–330°W.

#### 4.2. DISCUSSION AND CONCLUSION

The analyses of trends of micro-fractures from the Golden Eagle and Champion Mines and prospect sites in the Ngubevu West area indicate that the orientations of the relative stress magnitudes, SHmax and SHmin, are fairly consistent with the N–NE-directed local- and

regional-scale compression that resulted in the formation of the Tugela Terrane and Natal Metamorphic Province (Jacobs and Thomas, 1994; Cornell et al., 1996., Arima and Johnston, 2001; Basson et al., 2005; McCourt et al., 2006; Bisnath et al., 2008). The above observations are also supported by deposit-scale field structural measurements of the  $S_1$  foliation at/around the two mine sites, which are indicative of a N–NE-directed compressive stress regime during the deformation of the lithologies at/around the study areas (Figures 4.1A and B). A few discrepancies are apparent in the data, however, which indicate a nearly E–W orientation of SHmax (see CM-14 and CM-19 in Table 4.2). These discrepancies indicate rotation of the stress field through time. A similar observation was made by Basson et al. (2005) from the variable orientation of slickenlines present in the Mfongosi Group in the Mfongosi area and the disparities in vein orientations between the Northern and Southern Mfongosi Valleys. Although there was no evidence to suggest the direction of stress evolution in this study, these researchers suggested a clockwise rotation of the stress field during deformation. However, as evidenced by the orientation of the foliation in Figure 4.1, these nearly E–W oriented fractures in sample CM-14 and CM-19 may just be paralleling the orientation of this local- and regional-scale fabric in the Ngubevu area.

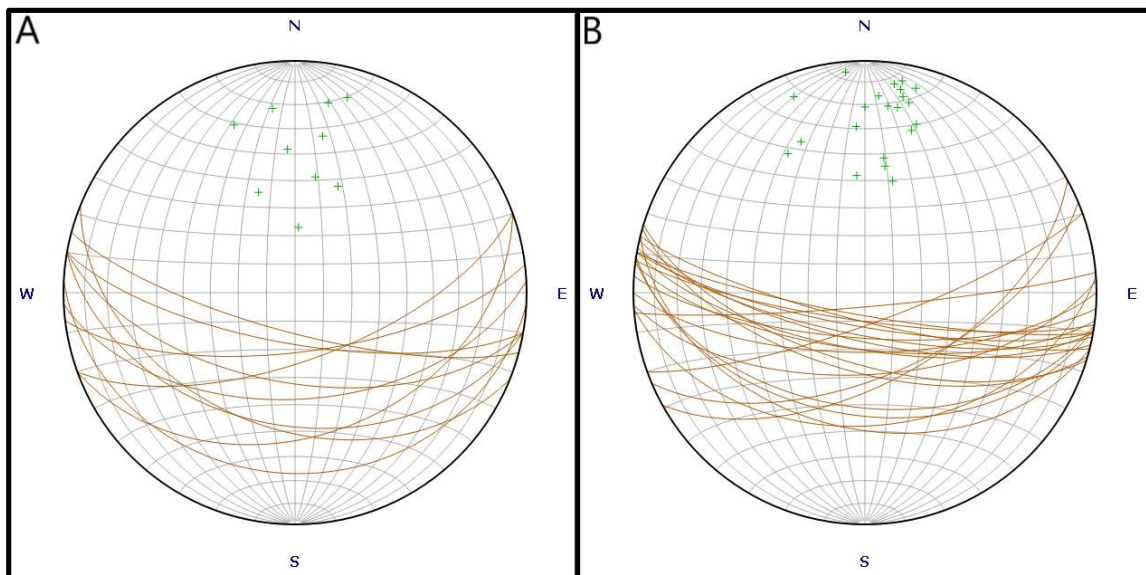


Figure 4.1: Equal area stereonet plots of deposit-scale field structural measurements collected at (A) Golden Eagle Mine area and prospect site and (B) Champion Mine area and prospect site. The beta planes represent foliations and crosses represent poles to the foliation.

With trends of the micro-fractures and orientations of relative stress magnitudes now obtained, the study shifted focus on spatial analysis of the micro-scale distribution of ore mineral centroids to identify trends in the distribution of the ore minerals. These trends are important because they can be related to structures controlling mineralisation in the study area.



## CHAPTER 5:

### POINT PATTERN ANALYSIS OF MICRO-SCALE MINERAL DISTRIBUTION

The spatial distribution of mineralisation of a specific type in an area is normally displayed and materialised as points (Carranza, 2008, 2009). Knowledge about the mineralisation phenomena that resulted in their distribution in certain locations (or points) can then be acquired from investigation of their geographical co-ordinates and corresponding spatial arrangement (Lloyd, 2007; Mamuse et al., 2010; Fils et al., 2020). Point pattern analysis is useful for acquiring information about the disposition of points in space; that is, it analyses patterns generated by a point process (Carranza, 2008; Maanijou et al., 2020).

Three principal types of spatial point patterns are recognised (Diggle, 1983, 2013; Boots and Getis, 1988). These are (1) a random pattern in which points have no correlation with each other, (2) a regular pattern where neighbouring points are farther apart compared to a random pattern and form uniformly spaced points, and (3) a clustered pattern where points form groups, and points within groups are closer to each other compared to points in a random pattern (Carranza, 2008, 2009; Fils et al., 2020). These fundamental point patterns are displayed in Figure 5.1. A random pattern results from independent processes that occur coincidentally, while regular and clustered patterns result from an interaction of processes that comprise either circulation (which form a regular pattern) or concentration (which form a clustered pattern) of point features at specific locations (Carranza, 2008, 2009; Fils et al., 2020).

Point pattern analysis has been used in the investigation of the regional-scale distribution of low-sulphidation epithermal gold deposits in the Philippines (Carranza, 2009), nickel sulphide deposits hosted in komatiite in western Australia (Mamuse et al., 2010), gold mineralisation in eastern Cameroon (Maanijou et al., 2020), local-to-regional scale distribution of copper mineralisation in SE Iran (Fils et al., 2020), and the micro- to local-scale distribution of iron-oxide copper-gold deposits in Brazil (Haddad-Martim et al., 2018). In this research, this technique was employed to investigate micro-scale mineral distribution of sphalerite grains, and to combine this information with knowledge of macro-scale deformation, with the aim of understanding controls on the distribution of shear zone-

hosted precious and base metal mineralisation in the Ngubevu area in the Natal Thrust Front of the Tugela Terrane.

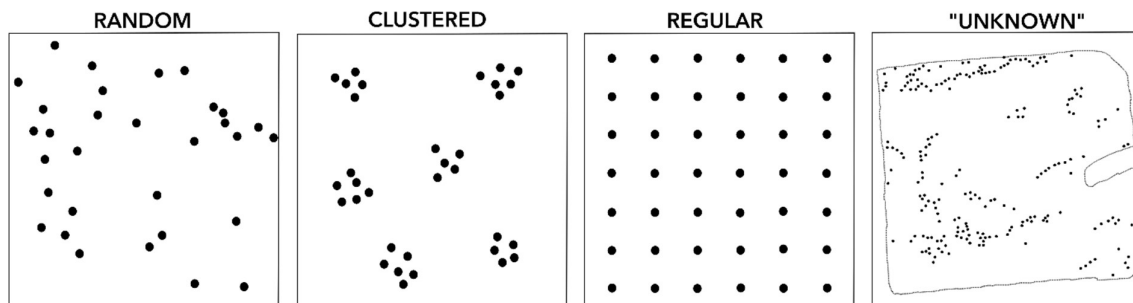


Figure 5.1: The three principal types of spatial point pattern occurrences; random, clustered, and regular (modified from Carranza, 2009). The unknown pattern represents centroids of sphalerite grains in thin section of sample CM-15B of this research.

In point pattern analysis, a pattern of points of interest is compared to a random pattern of points or pattern of complete spatial randomness (CSR) with the null hypothesis that the former is randomly distributed (Carranza, 2009; Maanijou et al., 2020). Alternatively, the point pattern under study is hypothesized to be non-random such that the points (which here represent ore mineral grains) were produced by an interaction of processes involving either concentration or circulation and, therefore, displaying either a clustered or a regular distribution, respectively (Carranza, 2009). These null and alternative hypotheses are tested by making use of certain measures of arrangement and of dispersion (Boots and Getis, 1988).

To measure the arrangement of points in this study, the number of observed reciprocal nearest neighbour (RNN) points (i.e., centroids of ore minerals) in oriented thin sections is compared with that expected for a completely random pattern (cf. Carranza, 2009). Two points are regarded as first-order RNNs when they are closest to each other in the point pattern (cf. Carranza, 2009). The number of observed RNN points is constantly even because RNNs are always point pairs (Carranza, 2009). The number of expected  $n^{\text{th}}$ -order RNN points is predicted according to the likelihood of a point being the  $n^{\text{th}}$ -order nearest neighbour of its own  $n^{\text{th}}$ -order nearest neighbour (Carranza, 2009). If the number of observed  $n^{\text{th}}$ -order RNN points is greater than anticipated in a completely random point pattern, then the points

of interest assume a clustered arrangement. The pattern of interest assumes a regular arrangement if the number of observed  $n^{\text{th}}$ -order RNN points is less than that anticipated for a completely random pattern. When the observed and anticipated numbers of  $n^{\text{th}}$ -order RNN points are equal, then the point pattern of interest assumes a random distribution.

To measure point dispersion, separations (or distances) between mapped ore mineral centroids in oriented thin sections were compared to separations between points in a completely random pattern (cf. Carranza, 2009; Haddad-Martim et al., 2018; Maanijou et al., 2020). This exercise was replicated for the same oriented thin sections used in the measure of arrangement. The distances measured from a point to every other point in a distribution of  $n$  number of points are known as the first, second, third or  $(n-1)^{\text{th}}$  neighbour distances (Carranza, 2009). When the average of the measured neighbour distances is less than that anticipated for a completely random pattern, the point pattern being investigated is a clustered pattern. The pattern of interest assumes a dispersed/regular distribution when the average of measured neighbour distances is greater than expected for a completely random pattern. If the averages of the measured and expected neighbour distances are equal, then the pattern under examination assumes a random distribution.

## **5.1. RESULTS**

The results of analysis of the spatial point patterns are discussed in the sub-sections that follow. Micro-maps of the spatial distribution of centroids of sphalerite grains in the thin section samples examined are shown in Figure A.1 of Appendix A for Golden Eagle and Figure A.2 for the Champion Mine.

### *5.1.1. Golden Eagle*

The analysis of six orders of RNNs (Table 5.1) for sample GE-01 showed that the points of ore mineral centroids assume a clustered spatial point pattern, because the observed number of RNNs was slightly higher than that anticipated for points in a pattern of CSR. However, in the 6<sup>th</sup>-order, the spatial point pattern assumes a regular distribution. The analysis of six orders of nearest neighbour distances (Table 5.1) also showed that the ore mineral centroids in

sample GE-01 assume a clustered distribution because the number of observed neighbour distances was slightly lower than that expected for points in CSR.

The analysis of six orders of RNNs (Table 5.1) for sample GE-02 showed that the ore mineral centroids assume a dominantly regular spatial point pattern, with clustering in the 3<sup>rd</sup>- and 6<sup>th</sup>-orders. The analysis of six orders of nearest neighbour distances (Table 5.1) showed that the ore mineral centroids in sample GE-02 assume a clustered spatial point distribution.

*Table 5.1: Average numbers of different orders of RNNs and averages of different orders of neighbour distances in the spatial pattern of ore centroids in the thin sections of samples from the Golden Eagle mine and prospect site.*

Sample	Order	RNNs		Neighbour Distances	
		Observed number	Expected number in CSR	Observed distance (m)	Expected distance in CSR (m)
GE-01	1st	90.00	85.15	0.06	0.10
	2nd	48.00	45.09	0.10	0.15
	3rd	38.00	33.30	0.14	0.19
	4th	38.00	27.61	0.17	0.22
	5th	34.00	24.11	0.19	0.25
	6th	18.00	21.67	0.22	0.27
GE-02	1st	80.00	87.63	0.06	0.08
	2nd	42.00	46.40	0.08	0.13
	3rd	36.00	34.28	0.11	0.16
	4th	28.00	28.41	0.13	0.18
	5th	18.00	24.82	0.14	0.21
	6th	24.00	22.31	0.16	0.23
GE-04	1st	186.00	188.31	0.06	0.07
	2nd	102.00	99.72	0.09	0.11
	3rd	80.00	73.66	0.11	0.13
	4th	52.00	61.05	0.14	0.15
	5th	54.00	53.33	0.15	0.17
	6th	44.00	47.93	0.17	0.19
GE-09	1st	54.00	53.45	0.11	0.15
	2nd	24.00	28.30	0.18	0.23
	3rd	26.00	20.91	0.24	0.29
	4th	24.00	17.33	0.29	0.34
	5th	16.00	15.14	0.35	0.38
	6th	12.00	13.61	0.40	0.41
GE-10	1st	26.00	22.37	0.11	0.22
	2nd	12.00	11.85	0.28	0.34
	3rd	8.00	8.75	0.34	0.42
	4th	6.00	7.25	0.48	0.49
	5th	2.00	6.34	0.53	0.55
	6th	4.00	5.70	0.57	0.61

The analysis of six orders of RNNs (Table 5.1) for sample GE-04 showed that the ore mineral centroids assume both regular and clustered spatial point patterns. Clustering occurs in the 2<sup>nd</sup>-, 3<sup>rd</sup>-, and 5<sup>th</sup>-orders, while the pattern was regular in the 1<sup>st</sup>-, 4<sup>th</sup>-, and 6<sup>th</sup>-orders. The analysis of six orders of nearest neighbour distances (Table 5.1) showed that the ore mineral centroids in sample GE-04 assume a clustered spatial point distribution.

The analysis of six orders of RNNs (Table 5.1) for sample GE-09 showed that the ore mineral centroids assume a mostly clustered spatial point pattern, with regular spatial point patterns observed in the 2<sup>nd</sup>- and 6<sup>th</sup>-orders. The analysis of six orders of nearest neighbour distances (Table 5.1) showed that the ore mineral centroids in sample GE-09 assume a clustered spatial point distribution.

The analysis of six orders of RNNs (Table 5.1) for sample GE-10 showed that the points of ore mineral centroids assume a mostly regular spatial point pattern with clustering occurring in the 1<sup>st</sup>- and 2<sup>nd</sup>-orders. The analysis of six orders of nearest neighbour distances (Table 5.1) showed that the ore mineral centroids in sample GE-10 assume a clustered spatial point distribution.

#### *5.1.2. Champion Mine*

The analysis of six orders of RNNs (Table 5.2) for sample CM-15B showed that the ore mineral centroids occupy a regular spatial point pattern because the observed number of RNNs was lower than expected for points in CSR. However, in the 3<sup>rd</sup>- and 4<sup>th</sup>-order RNNs, the points assume a clustered distribution of the spatial point pattern. The analysis of six orders of nearest neighbour distances (Table 5.2) showed that the ore mineral centroids in sample CM-15B occupy a clustered distribution because the observed number of neighbour distances was less than anticipated for points in CSR.

The analysis of six orders of RNNs (Table 5.2) for sample CM-19 showed that the ore mineral centroids assume a regular spatial point pattern. The analysis of six orders of nearest neighbour distances (Table 5.2) showed that the ore mineral centroids in sample CM-19 assume a clustered spatial point distribution.

The analysis of six orders of RNNs (Table 5.2) in sample CM-24 showed that the ore mineral centroids mostly assume a regular spatial point pattern, with clustering occurring in the 2<sup>nd</sup>- and 3<sup>rd</sup>-orders. The analysis of six orders of nearest neighbour distances (Table 5.2) showed that the ore mineral centroids in sample CM-24 assume a clustered spatial point distribution.

*Table 5.2: Average numbers of different orders of RNNs and averages of different orders of neighbour distances in the spatial pattern of ore centroids in the thin sections of samples from the Champion Mine and prospect site.*

Sample	Order	RNNs		Neighbour Distances	
		Observed number	Expected number in CSR	Observed distance (m)	Expected distance in CSR (m)
<b>CM-15B</b>	1st	120.00	129.89	0.06	0.08
	2nd	64.00	68.78	0.08	0.12
	3rd	58.00	50.81	0.10	0.15
	4th	52.00	42.11	0.13	0.17
	5th	32.00	36.78	0.16	0.20
	6th	32.00	33.06	0.18	0.22
<b>CM-19</b>	1st	68.00	68.37	0.09	0.14
	2nd	30.00	36.20	0.13	0.21
	3rd	22.00	26.74	0.17	0.26
	4th	18.00	22.17	0.22	0.30
	5th	10.00	19.36	0.28	0.34
	6th	14.00	17.40	0.32	0.38
<b>CM-24</b>	1st	140.00	140.46	0.06	0.11
	2nd	78.00	74.38	0.09	0.16
	3rd	76.00	54.94	0.12	0.20
	4th	40.00	45.54	0.15	0.24
	5th	34.00	39.78	0.17	0.27
	6th	24.00	35.75	0.20	0.29

## 5.2. DISCUSSION AND CONCLUSION

The point pattern analyses of centroids of sphalerite grains show that their occurrence in the Golden Eagle and Champion Mines and prospect sites in the Ngubevu area is non-random. The precious and base metal mineralisation at the micro-scale in the area resulted from approximately regularly spaced but densely packed geological processes/structures. These geological processes/structures were permissive for (a) the circulation of mineralising hydrothermal fluids to form the mostly regular arrangement of ore minerals, and (b) the concentration of these fluids resulting in a clustered distribution of ore minerals. These

imply that, at the micro-scale, the mineral deposits in the Golden Eagle and Champion Mines and prospect sites formed regularly arranged clusters. This assertion is visually demonstrated in Figure 5.1. The “unknown” pattern in Figure 5.1, which represents points in sample CM-15B, shows clusters of mineral centroids in certain locations but also “lines” that indicate the regular dispersion of the spatial pattern.

At this stage, it is difficult to assess which factors controlled mineral deposit formation and distribution based on only the geometrical perspective provided by point pattern analysis (cf. Haddad-Martim et al., 2018). Therefore, to identify trends in ore mineral distributions, which can provide insights to structural controls, the micro-maps of ore mineral centroids were subjected to Fry analysis (Chapter 6).



## CHAPTER 6:

### FRY ANALYSIS OF MICRO-SCALE MINERAL DISTRIBUTION

Fry analysis was developed by Norman Fry in 1979 as a method for studying strain in rocks based on the respective locations of geological objects in a thin section (Fry, 1979; Hanna and Fry, 1979). Fry analysis is carried out by constructing an autocorrelation diagram referred to as the Fry plot (Sun et al., 2018). In a Fry plot, the separations and directions of each point from every other point in a pattern are recorded, therefore revealing any subtleties in the spatial point pattern (Carranza, 2009). Rose diagrams can then be constructed, based on a Fry plot, to analyse the preferred orientations of point pairs within specific distances from each other or of all point pairs in a pattern. Fry plots can reveal any structural controls on mineral deposit occurrence and distribution based on directional trends in a point pattern (Parsa and Maghsoudi, 2018; Sun et al., 2018; Fils et al., 2020).

Fry analysis can be carried out manually on a tracing paper or by using software in a computer (Vearncombe and Vearncombe, 1999). In this study, Fry analysis was accomplished using the DotProc computer software because computerised Fry analysis is efficient for large data sets and provides the additional capability of plotting points within specified distances from each other which is not readily available manually (cf. Vearncombe and Vearncombe, 1999). For  $n$  number of points, Fry analysis creates  $n^2 - n$  translated points, which are referred to as Fry points (Parsa and Maghsoudi, 2018). The procedure for constructing a Fry plot is indicated in Figure 6.1 and it was carried out through the following steps (Sun et al., 2018):

- (1) Two sheets of tracing paper, including a sheet with the original spread of points and an empty sheet, were prepared.
- (2) The centre, "C", of the empty tracing sheet was overlaid on a single point in the pattern.
- (3) The positioning and distances of all remaining points were then recorded on the empty sheet of tracing paper.
- (4) The centre, "C", of the empty tracing sheet was then placed on another point and the positioning and distances of all the other points were recorded. This process was repeated until all points in the pattern have been plotted as the diagram

centre. The resulting point spread with all pairs of translated points is referred to as a Fry plot.

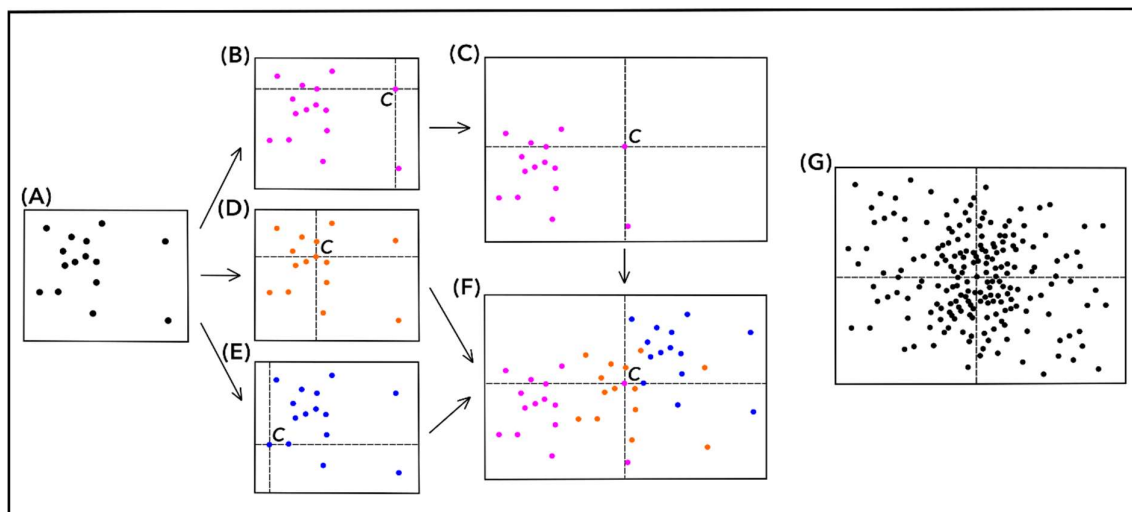


Figure 6.1: Schematic diagram illustrating the procedure for the construction of a Fry plot (modified from Sun et al., 2018). (A) Original point pattern. (B) One of the points in the original pattern is used as the diagram centre/origin. (C) Fry distribution according to points in (B). (D) and (E) Other points are selected and used as the diagram centre. (F) Fry distribution according to points in (B), (D), and (E). (G) Fry plot obtained when all points in (A) have been used as the diagram centre. For the translations shown in the above diagram, "C" indicates the points used as the diagram centre.

For Fry analysis to be effective, it is required that the points under study are well-spread to allow representation as points in a matrix that is evenly deformed, to allow for mathematically appropriate sampling, and to have a pre-strain distribution that is relatively regular or clustered (Fry, 1979; Hanna and Fry, 1979). A regular or clustered distribution of points is significant because a Fry diagram of random points does not produce appropriate results (Haddad-Martim et al., 2017).

In this research, centroids of sphalerite grains were mapped from oriented polished thin sections and subjected to Fry analysis. This was done for distances within which there is a probability of only one neighbour point occurrence next to any point in the distribution. The choice of a single point occurrence next to a neighbour point in this study was so that the Fry analyses revealed trends of Fry points related to micro-scale structural controls on mineral deposit formation/distribution (cf. Vearncombe and Vearncombe, 1999; Carranza,

2009; Parsa and Maghsoudi, 2018) and to minimise spurious results because Fry analysis can be sensitive to study areas with narrow shapes (Haddad-Martim et al., 2018). Because the locations of sphalerite grains in a thin section were derived from oriented samples, the trends in their spatial point distribution in the micro-scale were compared to the trends of micro-fractures and local-scale structures to identify plausible structural controls on mineralisation in the Golden Eagle and Champion Mines and prospect sites in the Ngubevu area.

## **6.1. RESULTS**

The following sections provide results from rose diagrams of the micro-scale trends of Fry points of ore mineral centroids in the Golden Eagle and Champion mines and prospect sites. The Fry plots of mineral deposit distribution are not shown here because it is difficult to visualise trends in the distribution of mineral deposits with the naked eye since the number of Fry points created for each oriented thin section is too large. For example, the Fry plot of 209 centroids of sphalerite grains in sample CM-15B returned 43 472 Fry points. The Fry plots of the data are displayed in Figure B.1 of Appendix B for Golden Eagle and Figure B.2 for the Champion Mine.

### *6.1.1. Golden Eagle*

The rose diagrams for the Fry plots of centroids of sphalerite grains in thin sections of oriented samples from the Golden Eagle mine and prospect site (Figure 6.2) show dominant trends of N00°–75°E and N270°–315°W. Minor trends in the samples are N00°–45°E and N270°–300°W. These results from the rose diagrams of Fry plots suggest that the formation and distribution of mineral deposits in the micro-scale of the Golden Eagle mine and prospect site was controlled by NNE–NE- and WNW–NW-trending fractures/foliations with subsidiary control by NNE–NE trending fractures.

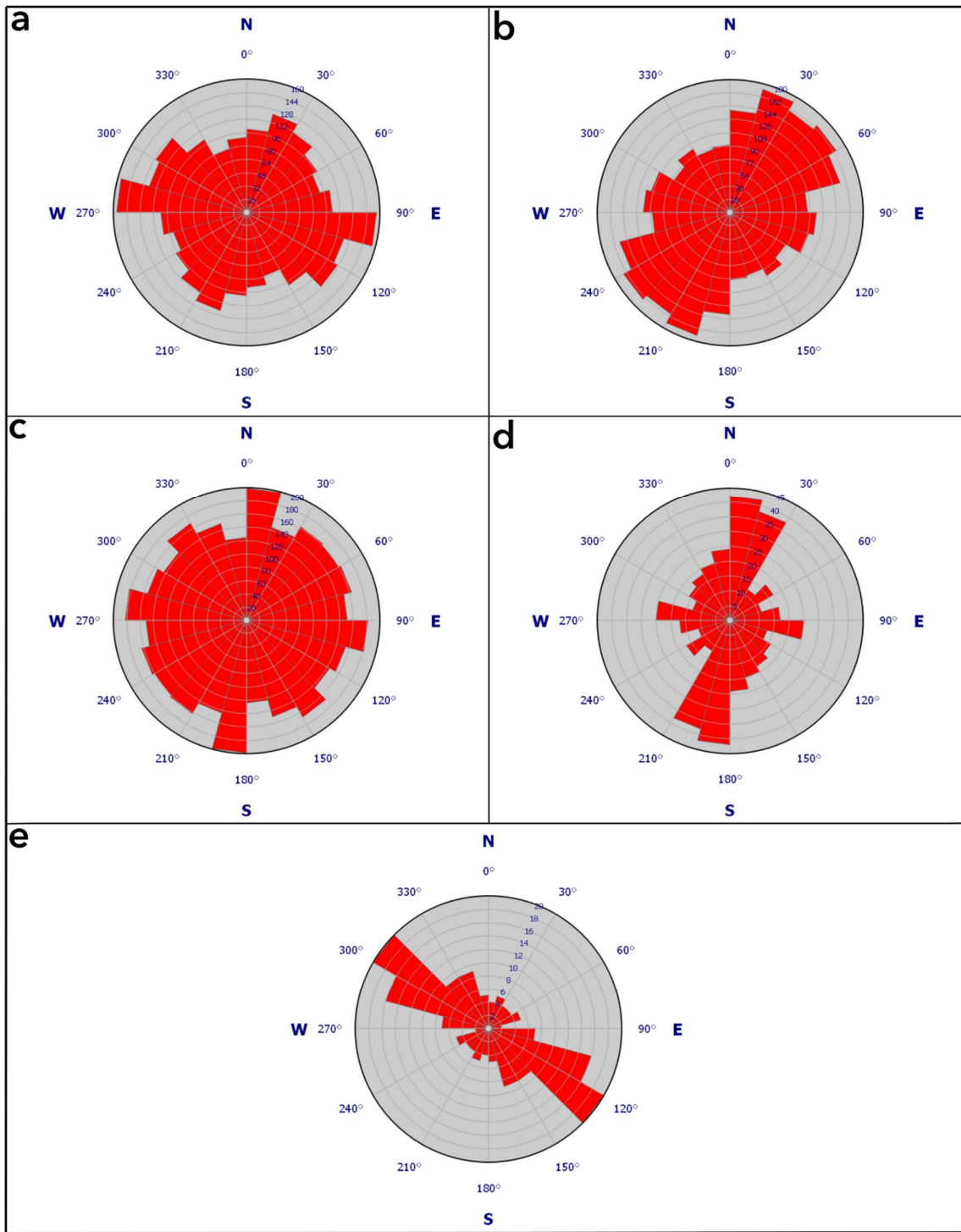


Figure 6.2: Trends of Fry points of centroids of spherulite grains in oriented thin sections of samples collected from the Golden Eagle Mine area and prospect site. (a) GE-01, (b) G-E02, (c) GE-04, (d) GE-09, (e) GE-10.

### 6.1.2. Champion Mine

The rose diagrams for the Fry plots of centroids of sphalerite grains in thin sections of oriented samples from the Champion Mine and prospect site (Figure 6.3) show dominant trends of N00°–75°E, N45°–105°E and N315°–345°W. A minor trend of N270°–300°W is also observed in the samples. These results from the rose diagrams of Fry plots suggest that the formation and distribution of mineral deposits in the micro-scale of the Champion Mine and prospect site was controlled by NNE–NE-, NE–ENE- and NNW-trending fractures/foliations with subsidiary control by WNW trending fractures/foliations.

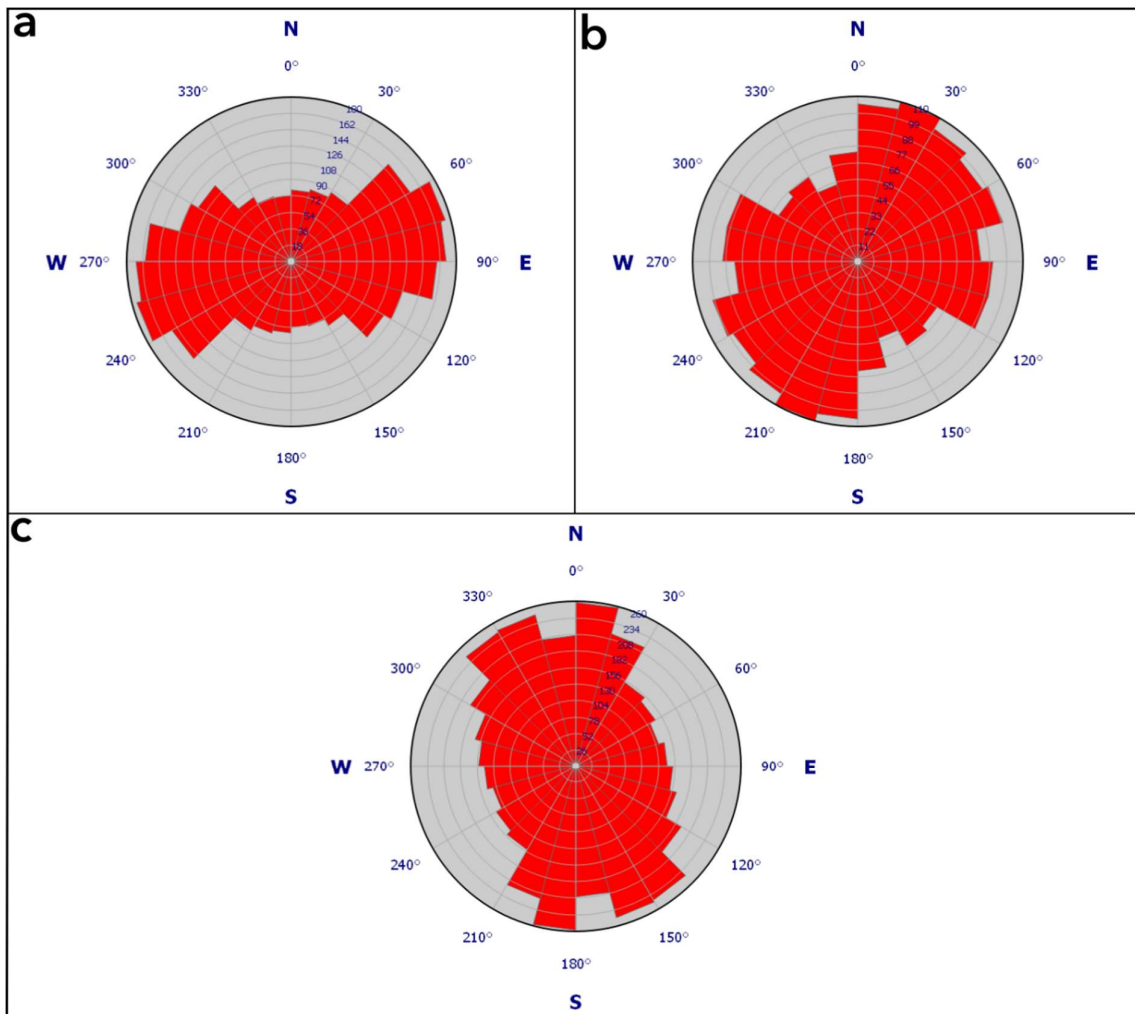


Figure 6.3: Trends of Fry points of centroids of sphalerite grains in oriented thin sections of samples collected from the Champion Mine area and prospect site. (a) CM-15B, (b) CM-19, (c) CM-24.

## 6.2. DISCUSSION AND CONCLUSION

The Fry analyses of the trends in the thin section distribution of sphalerite grains suggest that the formation and distribution of mineral deposits in the micro-scale of the Golden Eagle and Champion Mines and prospect sites in the Ngubevu area was plausibly controlled mostly by fractures/foliations with NNE–SSW, NNW–SSE, and approximately E–W trends. These trends in the Fry plots of micro-scale mineral distribution suggest that, in the light of the results of point pattern analysis (Chapter 5), the mineral deposits formed at regularly spaced intervals along NNE–SSW-, NNW–SSE- and nearly E–W-trending fractures/foliations. Deposit clusters were plausibly formed at intersections of such fractures/foliations.

Previous researchers (Thomas et al., 1990; Bullen et al., 1994; Basson, 2000) have shown that the emplacement of mineralised quartz-feldspar veins in the Ngubevu area was structurally controlled by the nearly E–W-trending  $S_1$  foliation present in the lithologies of the Mfongosi Group. This earlier interpretation is supported by the nearly E–W trends found in this study of Fry plots of centroids of sphalerite grains in the micro-scale. Therefore, the presence of similar trends in the deposit- to local-scale structures and micro-scale mineral distribution suggests the scale-invariance of the behaviour of the geological structures that controlled the mineralisation in the Ngubevu area (cf. Fils et al., 2020). To investigate further this scale-invariance, the micro-scale distributions of ore minerals present in the oriented thin sections were subjected to fractal analysis (Chapter 7).

## **CHAPTER 7:**

### **FRACTAL ANALYSIS OF MICRO-SCALE MINERAL DISTRIBUTION**

A fractal is an entity with a Hausdorff–Besicovitch or fractal dimension, the parameter employed to characterise natural fractals; the fractal dimension of a fractal exceeds its Euclidean dimension (Mandelbrot, 1983). Fractals present similar geometric patterns at various spatial scales, and numerous geological objects, such as coastlines and drainage patterns, possess fractal properties (Turcotte, 1989; Goryainov et al., 1997; Hodkiewicz et al., 2005; Sun et al., 2018). The scale-invariance of any fractal can be shown by means of a power-law relationship between its pattern (or geometry) and its scale (Mandelbrot, 1977).

The box- or quadrant-counting and radial density techniques of obtaining the fractal dimension of a pattern are the most commonly used for analysis of spatial geometric (e.g., point, line, polygon) patterns (Sun et al., 2018). The aim of investigating the fractality of a spatial point pattern (e.g., distribution of mineral deposits of a given type) in mineral exploration is to establish the various scales through which geological features/processes have functioned in the formation and distribution of mineral deposits (usually depicted as points on a map) in a certain region because certain controls on mineralisation could be dependent or operate only on a certain scale (Austin and Blenkinsop, 2009; Parsa and Maghsoudi, 2018). In this study, the box-counting method for obtaining fractal dimension was applied to the spatial patterns of centroids (i.e., points) of sphalerite grains mapped in thin sections of oriented samples from the Golden Eagle and Champion Mines and prospect sites.

#### **7.1. BOX-COUNTING FRACTAL DIMENSION**

To derive the fractal dimension of an object with the box-counting method (Figure 7.1), the examined area (i.e., a thin section) is overlain with a grid of square cells with a side of length  $\delta$ , and the number of squares containing at least one point (i.e., centroid of sphalerite grain),  $n(\delta)$ , is counted (Haddad-Martim et al., 2017, 2018). This procedure is replicated with different box sizes to obtain the corresponding numbers of boxes containing points (Maanijou et al., 2020). If the spatial point pattern under examination has fractal properties,

then the association of  $n(\delta)$  vs  $\delta$  will follow a power function equation as denoted in Equation 1 (Mandelbrot, 1983):

$$n(\delta) = A\delta^{-D_b} \quad \text{(Equation 1)}$$

where  $D_b$  is the box/quadrant-counting fractal dimension, which varies between 0 and 2, and  $A$  is a proportionality constant between  $n(\delta)$  and  $\delta$  representing the mean number of points in square cells with a mean side length of  $\delta$  (Carranza, 2009; Parsa and Maghsoudi, 2018). The outcomes of the analyses are then plotted on a  $\log n(\delta)$  vs  $\log \delta$  plot, and the fractal dimension of a spatial point pattern is derived from the power function equation of a regression line fitted through the points (Haddad-Martim et al., 2017, 2018). The grids of different sizes used in this study covered an identical area for each thin section to ensure consistency in the analysis (cf. Agterberg, 2013).

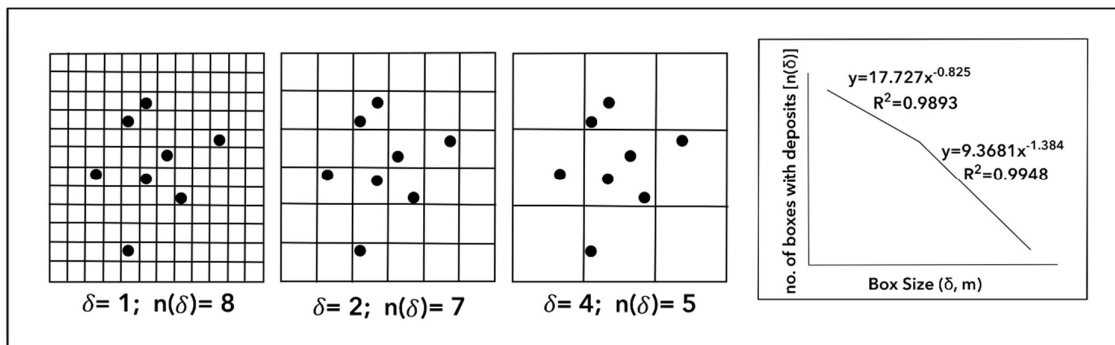


Figure 7.1: Schematic diagram illustrating the procedure for obtaining the fractal dimension of a pattern of points using the box-counting method (modified from Carranza, 2009). Grids of square cells with side lengths,  $\delta$ , are overlain over the point pattern. After each iteration, the number of square cells containing at least one point,  $n(\delta)$ , is counted. The dummy resulting plot on the right-hand side for the three iterations completed in this figure indicates a bifractal pattern with box-counting fractal dimensions of 0.825 and 1.384 based on the power functions of the equations. Because the dimensions of the thin sections in this study were exaggerated to facilitate viewing on a scale suitable for a laptop computer (see Chapter 3), the dimensions depicted in this log-log plot should be divided by 100 to obtain the correct micro-scale value.

## 7.2. RESULTS

The maps of ore mineral centroids in the thin section samples used in this study were exaggerated 100 $\times$  to facilitate viewing at a scale suitable for a laptop computer (see Chapter 3). Therefore, to obtain the correct micro-scale dimensions obtained during analysis the

resulting dimensions were divided by 100. The same was applied to the dimensions displayed on the log-log plots.

### 7.2.1. *Golden Eagle*

The spatial pattern of centroids of sphalerite grains mapped in sample GE-01 (Figure 7.2A) had two fractal dimensions because the plot of  $\log n(\delta)$  vs  $\log \delta$  for the point data was fitted with two straight lines by least squares regression. The straight-line segment fitted over the data when  $\delta$  was  $\leq 0.003 \mu\text{m}$  had a  $D_b$  of 0.635 and, when  $\delta$  was  $\geq 0.003 \mu\text{m}$  it had a  $D_b$  of 1.325.

The spatial pattern of centroids of sphalerite grains mapped in sample GE-02 (Figure 7.2B) had a single fractal dimension because the plot of  $\log n(\delta)$  vs  $\log \delta$  for the point data was fitted with one straight line by least squares regression. The straight-line segment fitted over the data had a  $D_b$  of 1.153 at all spatial scales.

The spatial pattern of centroids of sphalerite grains mapped in sample GE-04 (Figure 7.2C) had two fractal dimensions because the plot of  $\log n(\delta)$  vs  $\log \delta$  for the point data was fitted with two straight lines by least squares regression. The straight-line segment fitted over the data when  $\delta$  was  $\leq 0.002 \mu\text{m}$  has a  $D_b$  of 0.73 and, when  $\delta$  was  $\geq 0.002 \mu\text{m}$  it had a  $D_b$  of 1.331.

The spatial pattern of centroids of sphalerite grains mapped in sample GE-09 (Figure 7.2D) had two fractal dimensions because the plot of  $\log n(\delta)$  vs  $\log \delta$  for the point was fitted with two straight lines by least squares regression. The straight-line segment fitted over the data when  $\delta$  was  $\leq 0.003 \mu\text{m}$  had a  $D_b$  of 0.403 and, when  $\delta$  was  $\geq 0.003 \mu\text{m}$  it had a  $D_b$  of 1.257.

The spatial pattern of centroids of sphalerite grains mapped in sample GE-10 (Figure 7.2E) had two fractal dimensions because the plot of  $\log n(\delta)$  vs  $\log \delta$  for the point data was fitted with two straight lines by least squares regression. The straight-line segment fitted over the data when  $\delta$  was  $\leq 0.005 \mu\text{m}$  had a  $D_b$  of 0.399 and, when  $\delta$  was  $\geq 0.005 \mu\text{m}$  it had a  $D_b$  of 1.155.

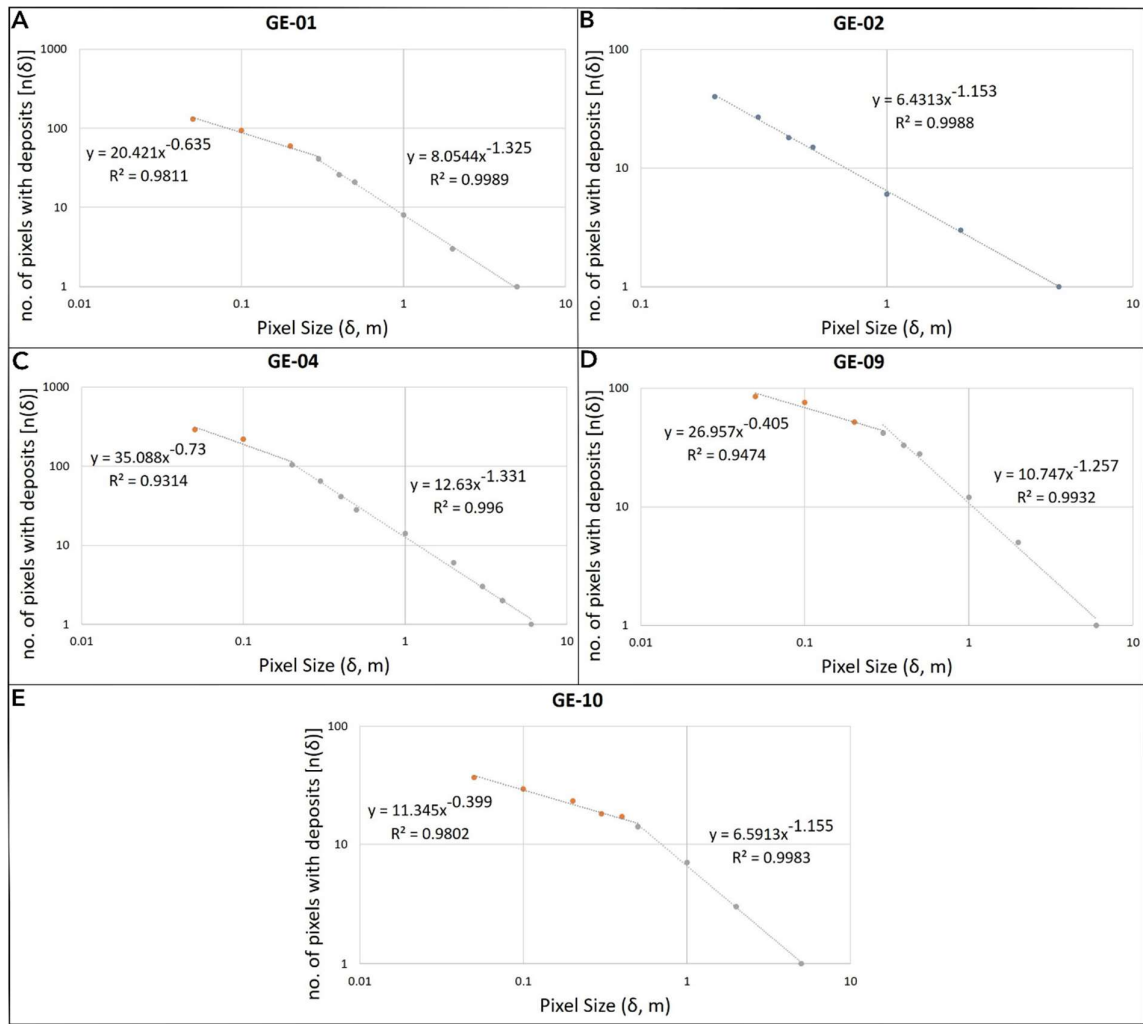


Figure 7.2: Log  $n(\delta)$  vs log  $\delta$  plots indicating fractal dimensions of patterns of sphalerite grains in thin sections of oriented samples from the Golden Eagle mine and prospect site: (A) GE-01, (B) GE-02, (C) GE-04, (D) GE-09, and (E) GE-10. The difference in colour of the points indicates a change in fractal dimension. Because the dimensions of the thin sections in this study were exaggerated to facilitate viewing on a scale suitable for a laptop computer (see Chapter 3), the dimensions depicted in these log-log plots should be divided by 100 to obtain the correct micro-scale value.

### 7.2.2. Champion Mine

The spatial pattern of centroids of sphalerite grains mapped in sample CM-15B (Figure 7.3A) had two fractal dimensions because the plot of log  $n(\delta)$  vs log  $\delta$  for the point data was fitted with two straight lines by least squares regression. The straight-line segment fitted over the data when  $\delta$  was  $\leq 0.004 \mu\text{m}$  had a  $D_b$  of 0.825 and, when  $\delta$  was  $\geq 0.004 \mu\text{m}$  it had a  $D_b$  of 1.384.

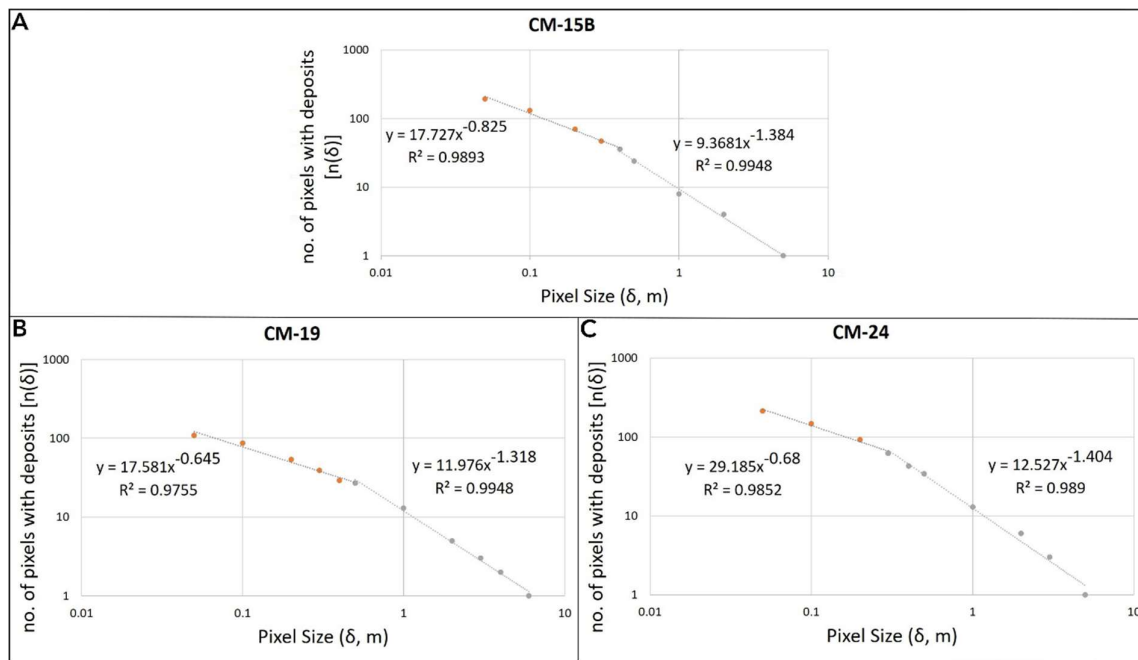


Figure 7.3: Log  $n(\delta)$  vs log  $\delta$  plots indicating fractal dimensions of patterns of sphalerite grains in thin sections of oriented samples from the Champion Mine and prospect site: (A) CM-15B, (B) CM-19, and (C) CM-24. The difference in colour of the points indicates a change in fractal dimension. Because the dimensions of the thin sections in this study were exaggerated to facilitate viewing on a scale suitable for a laptop computer (see Chapter 3), the dimensions depicted in these log-log plots should be divided by 100 to obtain the correct micro-scale value.

The spatial pattern of centroids of sphalerite grains mapped in sample CM-19 (Figure 7.3B) had two fractal dimensions because the plot of log  $n(\delta)$  vs log  $\delta$  for the point data was fitted with two straight lines by least squares regression. The straight-line segment fitted over the data when  $\delta$  was  $\leq 0.005 \mu\text{m}$  had a  $D_b$  of 0.645 and, when  $\delta$  was  $\geq 0.005 \mu\text{m}$  it had a  $D_b$  of 1.318.

The spatial pattern of centroids of sphalerite grains mapped in sample CM-24 (Figure 7.3C) had two fractal dimensions because the plot of log  $n(\delta)$  vs log  $\delta$  for the point data was fitted with two straight lines by least squares regression. The straight-line segment fitted over the data when  $\delta$  was  $\leq 0.003 \mu\text{m}$  had a  $D_b$  of 0.680 and, when  $\delta$  was  $\geq 0.003 \mu\text{m}$  it had a  $D_b$  of 1.404.

### 7.3. DISCUSSION AND CONCLUSION

The box-counting fractal analyses of micro-scale distributions of sphalerite grains in the Golden Eagle and Champion Mines and prospect sites indicate that micro-scale mineral occurrence in mines/prospects in the study areas is non-random and their distribution is fractal. This is deduced from the plots of  $\log n(\delta)$  vs  $\log \delta$ , which exhibit fractional slopes greater than -2 (cf. Carranza, 2009; Parsa and Maghsoudi, 2018). These results are also in accordance with the results of point pattern and Fry analyses (Chapters 5 and 6, respectively).

Certain geological processes/features that controlled the flow of mineralising hydrothermal fluids and, then, mineral deposition in the study areas functioned in a minimum of two spatial scales. One kind of geological control on mineralisation operated in spatial scales of at most 0.005  $\mu\text{m}$  resulting in mineralisation as points that behave as Euclidean lines at the micro-scale. This is visually demonstrated in the unknown pattern in Figure 5.1, which shows mineral deposits as points that form clusters (a point feature) that form lines at regular intervals and define trends in the distribution of mineralisation. Another type of geological control operated at spatial scales of at least 0.002  $\mu\text{m}$  resulting in mineralisation as lines that may define planes. This is also visually demonstrable in Figure 5.1, in which lines can be drawn along points to define linear features and, where these lines connect, they may define or approximate two-dimensional shapes.

To supplement further the point pattern, Fry and fractal analyses, oriented images of sphalerite grains were subjected to shape analysis to identify trends in their distributions. The results of shape analysis are described and discussed in Chapter 8.

## CHAPTER 8:

### SHAPE ANALYSIS OF MICRO-SCALE MINERAL DISTRIBUTION

Shape analysis of mineral grains was developed in the early 1990s (Launeau et al., 1990; Launeau and Cruden, 1994; Launeau and Robin 1996). This method can help study a myriad of geological processes because it produces information about a feature's origin based on its resultant shape (Heilbronner and Barrett, 2014). This method has been employed before in geological remote sensing (Fabbri et al., 1993), paleontology (Crampton, 1995), geological exploration (Blenkinsop, 2004), and structural geology (Launeau and Robin 1996; Heilbronner and Keulen, 2006). The various methods for studying the shapes of objects are reliant on cross-sectional area, best-fit ellipse, Feret diameter or projection, digital image analysis for grain measurements, intersection method, shape preferred orientation and perimeter measurements (Launeau et al., 1990; Launeau and Cruden, 1994; Launeau and Robin 1996; Heilbronner and Keulen, 2006).

In this study, shape analysis was employed using the best-fit ellipse method to determine the micro-scale orientations of sphalerite grains on the horizontal plane. This analysis is a useful supplement to Fry analysis (Chapter 6) of trends in the occurrence and distribution of sphalerite grains/centroids in oriented thin sections of samples from the Golden Eagle and Champion Mines and prospect sites. This method has been employed by Haddad-Martim et al. (2018) to study structural controls on mineralisation in the world-class iron-oxide copper-gold deposits in the Carajás Mineral Province of Brazil.

It is helpful to simplify the shapes of the ore minerals being examined to basic parameters of size, axial ratio and orientation; best-fit ellipses are convenient in this regard because their shapes are defined by all three parameters (Heilbronner and Barrett, 2014; Haddad-Martim et al., 2018). Not all naturally occurring materials are elliptical; however, best-fit ellipses are justifiable in representing these parameters for a given shape, particularly for axial ratio and alignment (Heilbronner and Barrett, 2014). In this study, the focus was on the preferred orientations of ellipses that best-fit sphalerite grains in the oriented images of thin sections, as indicated by the orientations of the long axes of the ellipses.

## 8.1. RESULTS

The sections that follow discuss results from the rose diagrams of the orientations of best-fit ellipses fitted to sphalerite grains in thin section samples from the study area. Oriented photomicrographs of samples are shown in Figures C.1 and C.2 of Appendix C for Golden Eagle and C.3 for the Champion Mine. The binary images of sphalerite grains fitted with best-fit ellipses are shown in Figures D.1 and D.2 of Appendix D for Golden Eagle and D.3 for the Champion Mine.

### 8.1.1. Golden Eagle

The rose diagrams of orientations of the long axes of ellipses that best-fit sphalerite grains in oriented images of thin sections of samples from the Golden Eagle mine and prospect site (Figure 8.1) showed dominant trends of N00°–60°E, N75°–90°E, N270°–300°W and N330°–345°W. A minor trend of N315°–330°W was also observed in the samples.

The results of the shape analysis suggest that the micro-scale flow of mineralising hydrothermal fluids, which resulted in the formation/distribution of mineral deposits in the Golden Eagle mine and prospect site was structurally controlled by NNE–NE-, ENE-, and NNW-trending fractures. The micro-scale flow of mineralising hydrothermal fluids was also controlled by WNW-trending foliations. Subsidiary structural control on micro-scale fluid flow and mineral deposition occurred due to NW-trending fractures.

### 8.1.2. Champion Mine

The rose diagrams of orientations of the long axes of ellipses that best-fit sphalerite grains in oriented images of thin sections of samples from the Champion Mine and prospect site (Figure 8.2) showed dominant trends of N00°–75°E, N270°–285°W and N315°–330°W. A minor trend of N60°–90°E was also observed in the samples.

The results of the shape analysis suggest that the micro-scale flow of mineralising hydrothermal fluids, which resulted in the formation/distribution of mineral deposits in the micro-scale of the Champion Mine and prospect site, was structurally controlled by NNE–NE-, , and NW-trending fractures. The micro-scale flow of mineralising hydrothermal fluids was

also controlled by WNW-trending foliations. Subsidiary control on micro-scale fluid flow and mineral deposition was due to ENE-trending foliations.

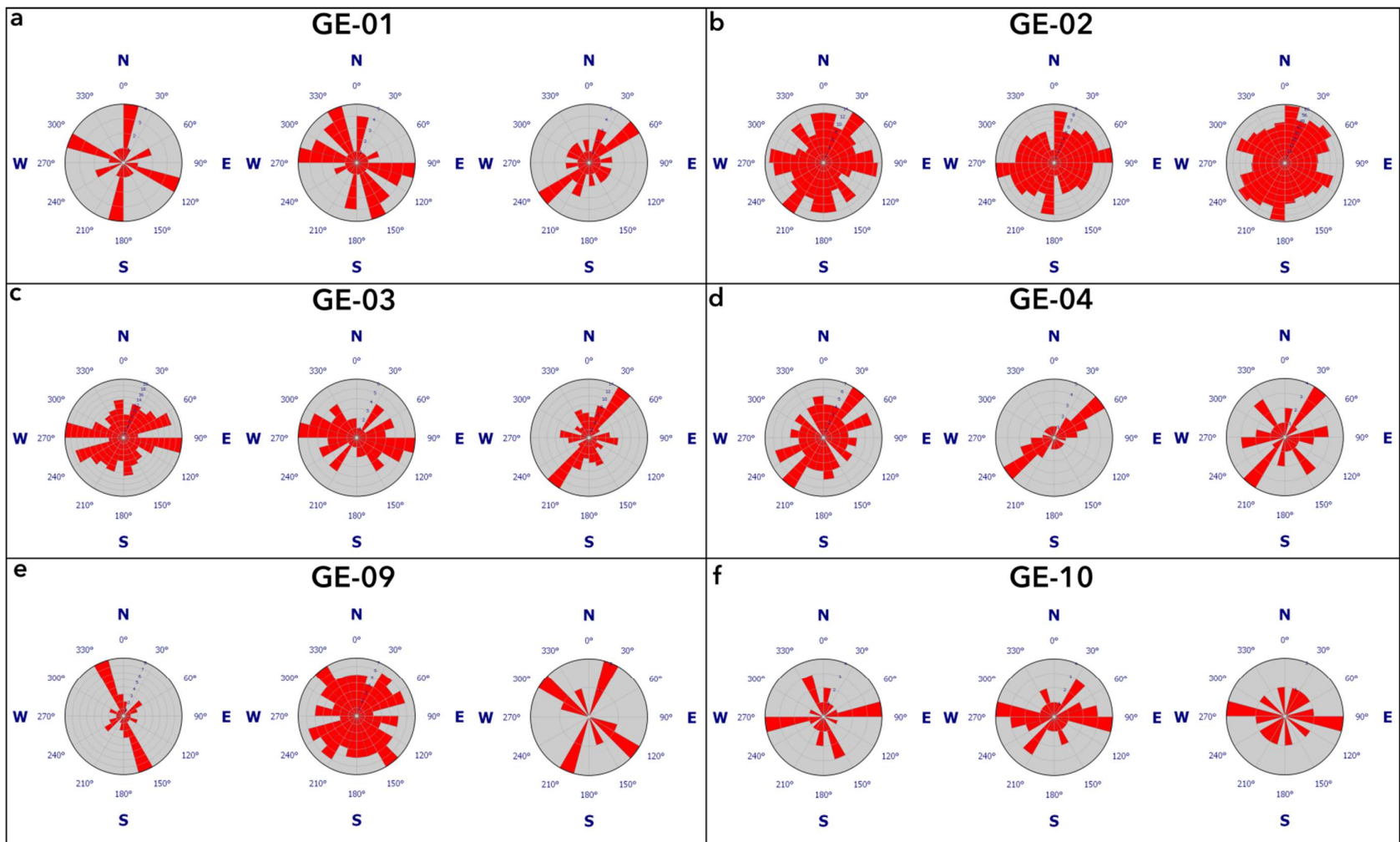


Figure 8.1: Trends in the orientations of ellipses that best-fit sphalerite grains in oriented images of thin sections of samples collected from the Golden Eagle Mine and prospect site. (a) GE-01, n = 69; (b) GE-02, n = 765; (c) GE-03, n = 242; (d) GE-04, n = 88; (e) GE-09, n = 100; and (f) GE-10, n=42.

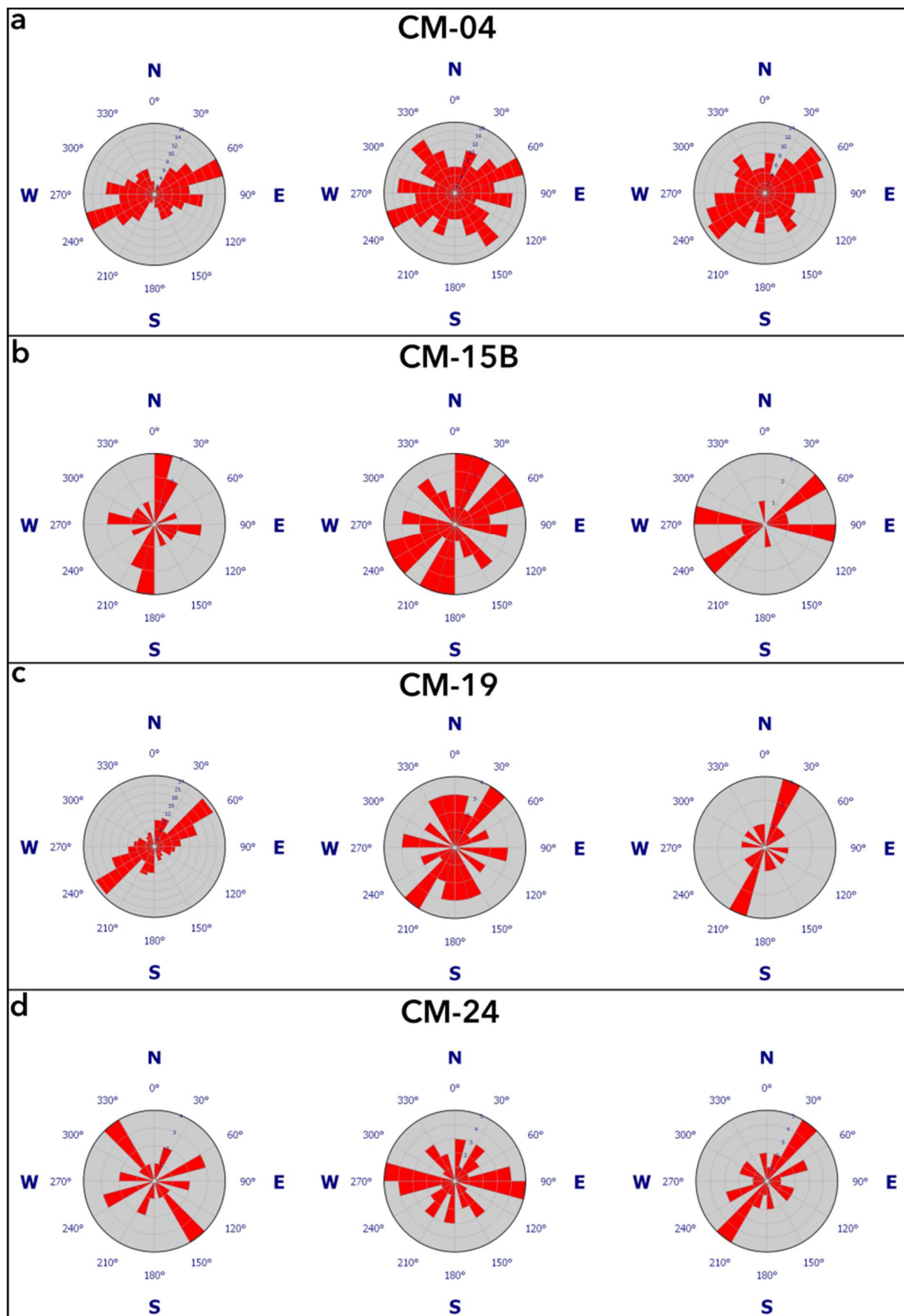


Figure 8.2: Trends in the orientations of ellipses that best-fit sphalerite grains in oriented images of thin sections of samples collected from the Champion Mine and prospect site. (a) CM-04,  $n = 320$ ; (b) CM-15B,  $n = 48$ ; (c) CM-19,  $n = 130$ ; and (d) CM-24,  $n = 59$ .

## 8.2. DISCUSSION AND CONCLUSION

The shape analyses of the micro-scale distribution of sphalerite grains in the Golden Eagle and Champion Mines and prospect sites indicate that the long axes of their best-fit ellipses are aligned preferably towards the NNE, NNW and E–W directions. This demonstrates that, in combination with the results of the point pattern and Fry analyses (Chapters 5 and 6, respectively), the formation and distribution of mineral deposit occurrences in the study areas was controlled by regularly arranged NNE–SSW- and NNW–SSE-trending fractures, and nearly E–W-trending foliations. Mineral deposit clusters were plausibly formed by mineralising hydrothermal fluids at intersections of differently oriented sets of fractures and between intersections of fractures and foliations. The nearly E–W trends obtained from the shape analyses are also consistent with previous regional- to local- and deposit-scale research on the emplacement of mineralised quartz-feldspar veins ( $V_1$ ) in the Ngubevu area (Thomas et al., 1990; Bullen et al., 1994; Basson, 2000) and further demonstrate the scale-invariance of structural controls on mineral deposit formation/distribution in the Ngubevu area. The NNE–SSW and NNW–SSE trends of sphalerite grains observed in the analyses suggest the presence of macro-scale NNE–SSW- and NNW–SSE-trending ore-controlling fractures in the Ngubevu area. This interpretation is also supported by, and is consistent with, the results of fractal analysis discussed in Chapter 7, which show that the controls on mineral deposit occurrence in the study area are fractal and they functioned in at least two spatial scales.

In the following chapter, the results of micro-fracture trends, deposit-scale  $S_1$  foliation measurements and spatial analyses of mineral deposit distribution are integrated and discussed with local- to regional-scale data from the literature regarding the precious and base metal mineralisation in the Ngubevu area in the Natal Thrust Front of the Tugela Terrane.

## **CHAPTER 9: DISCUSSION**

### **9.1. MICRO-SCALE STUDY OF MINERAL DEPOSIT DISTRIBUTION**

The methods employed in this research to the micro-scale study of structural controls on mineral deposit formation/distribution have been used before in previous studies. However, these previous studies were mostly conducted at the local- to regional-scales (e.g., Carranza, 2009; Carranza et al., 2009; Haddad-Martim et al., 2017; Amirhanza et al., 2018; Parsa and Maghsoudi, 2018; Sun et al., 2018; Fils et al., 2020; Maanijou et al., 2020). The scale-invariance of mineral deposit spatial distribution has been demonstrated before and interpreted as a result of the fractality of structures that controlled the flow of mineralising hydrothermal fluids (Blenkinsop and Sanderson, 1999; Hodkiewicz et al., 2005); therefore, suggesting systematic geometric patterns in mineral deposit distribution regardless of spatial scale (Munro et al., 2018). Because controls on mineral deposit formation could be scale-invariant and because results of micro-scale study could be linked to local-scale controls on mineral deposit formation, this research undertook to explore the likely scale-invariance of mineralisation controls in the Ngubevu area in the Natal Thrust Front of the Tugela Terrane. This was done to understand the various scales at which mineralisation operated and the structural controls on such mineralisation in the area.

Although the methodologies applied in this study have mostly been applied previously at the local- to regional-scales, their effectiveness has also been demonstrated for micro-scale study of hydrothermal mineral deposits (cf. Haddad-Martim et al., 2018). Haddad-Martim et al. (2018) employed the same spatial analytical methods (i.e., point pattern, Fry, fractal, and shape analyses) to study the micro- to regional-scale spatial distribution of iron-oxide copper-gold deposits in the Carajás Mineral Province. These authors were able to demonstrate that (a) controls on mineral deposit formation were fractal and (b) the trends of mineral deposits in the micro-scale followed known local- to regional-scale trends of mineral deposits and structures. Similarly, Carranza et al. (2019) analysed trends in the micro-scale distribution of geochemical anomaly centres using Fry analysis in the Carajás Mineral Province and found that the trends of micro-geochemical anomalies followed trends

of known macro-scale faults that controlled the occurrence/distribution of iron-oxide copper-gold mineralisation.

## **9.2. MICRO- TO LOCAL-SCALE STRUCTURAL CONTROLS ON PRECIOUS AND BASE METAL MINERALISATION IN THE NGUBEVU AREA**

The occurrence of mineral deposits in the micro-scale of the Golden Eagle and Champion Mines and prospect sites in the Ngubevu area is non-random and their spatial distribution is fractal. This micro-scale mineral distribution was structurally controlled by regularly spaced NNE–SSW- and NNW–SSE-trending sets of fractures, and nearly E–W-trending foliations, which plausibly controlled the circulation of mineralising hydrothermal solutions resulting in the regular spatial pattern of points depicting sphalerite grains in the mines/prospects. The flow of mineralising hydrothermal solutions was also plausibly focussed at intersections of different sets of micro-fractures, and intersections of micro-fractures and foliations where ore minerals may have precipitated from solution and formed clusters of points depicting the micro-scale spatial distribution of sphalerite grains in the Ngubevu area.

Micro-fractures grow from grain-scale stress concentrations and, as they become transgranular, they may propagate further and form macro-fractures (Anders et al., 2014). These sets of macro-fractures will have trends defined by the trends of micro-fractures of the same set from which they propagate (Laubach, 1989). If micro-fractures are part of a larger population of macro-fractures, then unrecognised macro-fractures can be revealed from micro-fracture study because orientations of separate transgranular/intercrystalline micro-fractures can be employed to establish macro-fracture trends (Laubach, 1997; Anders et al., 2014). Researchers have used micro-scale fractures to infer the presence of larger, local- to regional-scale fractures along the Shawangunk Ridge in New York and the Moine Thrust Zone in NW Scotland (Vermilye and Scholz, 1998; Laubach and Diaz-Tushman, 2009). Micro-fractures have also been used to predict successfully the orientation of regional-scale fractures in the San Juan Basin in New Mexico (Ortega and Marrett, 2000).

The fractal nature of structural controls on mineral deposit formation/distribution in the Golden Eagle and Champion Mines and prospect sites in the Ngubevu area has been proven in this study (Chapter 7). Therefore, this suggests the presence of regularly spaced NNE–

SWW- and NNW–SSE-trending corridors of macro-scale fractures in the areas of the two mines (Figure 9.1), and nearly E–W trending corridors of macro-scale foliations in at least the deposit- to local-scale of the Ngubevu area in the Natal Thrust Front of the Tugela Terrane. Discrepancies in orientations of micro-fractures in some samples indicating nearly E-W-orientations (Chapter 4) are likely due to rotation of the stress field during deformation (Basson et al., 2005). However, no evidence of rotation could be found in this study and so these micro-fracture sets may have preferably developed parallel to the prevailing foliation orientation (E-W) in the Ngubevu area (Ghazvinian et al., 2014). The fractures, here designated as  $F_1$ , and foliations ( $S_1$ ) developed during the dominantly N–NE-directed compressional tectonics that affected the Natal Metamorphic Province (McCourt et al., 2006; Bisnath et al., 2008; Sharib et al., 2021) and were plausibly whereabouts mineralising hydrothermal fluids were circulated in the deposit- to local-scale and focussed at the intersections of such structures. This interpretation is supported by the presence of the dominantly E–W-trending local- to regional-scale  $S_1$  foliation that controlled the emplacement of mineralised quartz-feldspar veins ( $V_1$ ) recognised by researchers in the Ngubevu area in the thrust front of the Tugela Terrane (Thomas et al., 1990; Basson, 2000), deposit-scale  $S_1$  measurements collected during this study and, the parallel NE-orientation of the relative stress magnitude,  $SH_{max}$ , with the maximum principal stress,  $\sigma_1$ , in the horizontal plane (i.e., the mapping plane) of the Natal Metamorphic Province. The parallel orientations of  $SH_{max}$  and  $\sigma_1$  in the horizontal plane show that the development of micro-fractures in the Ngubevu area is consistent with the model of proposed development for the Natal Metamorphic Province, which suggests N–NE-directed compression during the tectonic development of the province.

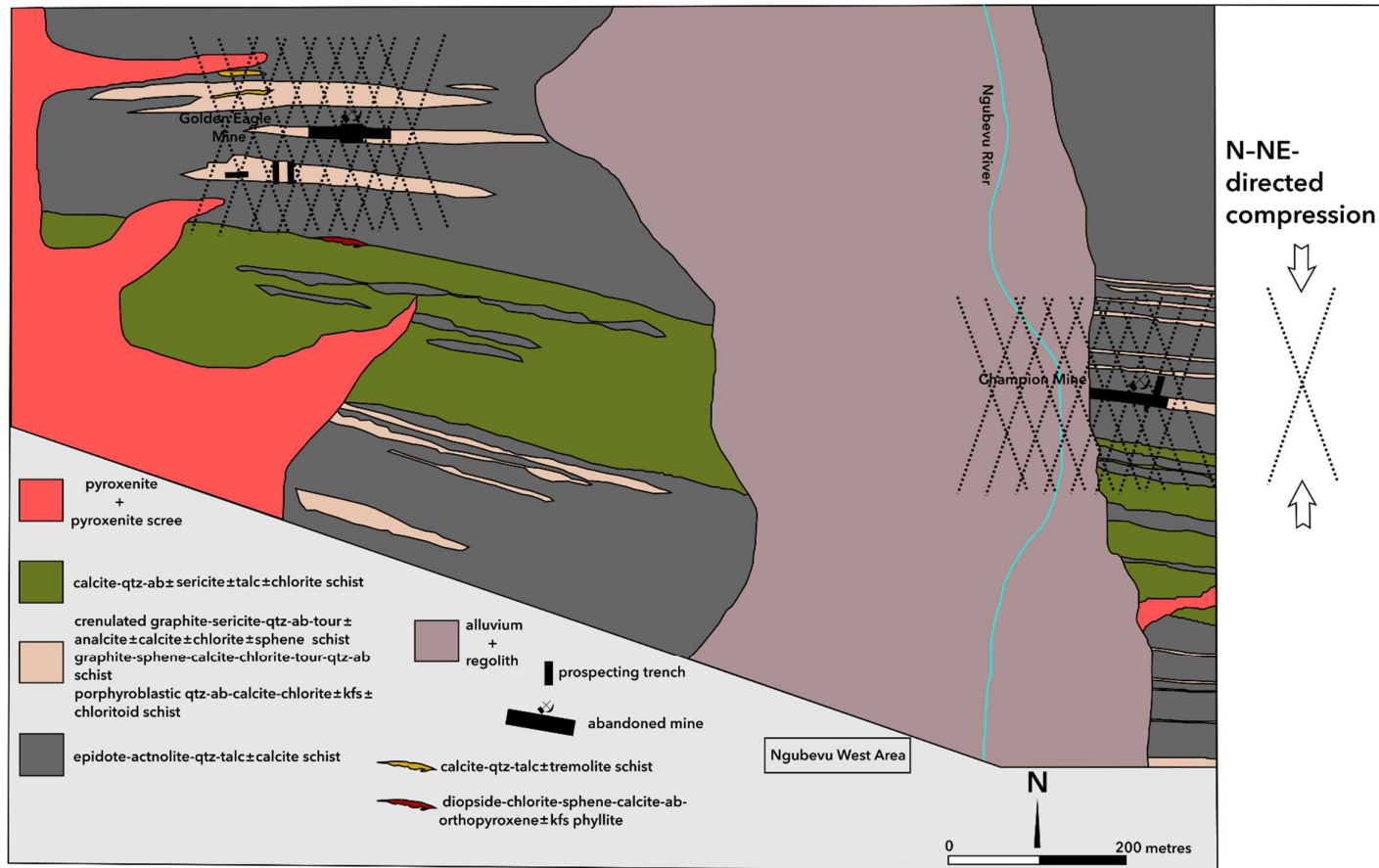


Figure 9.1: Lithological map of the Ngubevu West Area (modified from Basson, 2000) displaying a fracture mesh model of regularly spaced NNE-SSW- and NNW-SSE-trending sets of posited macro-scale fractures around the Golden Eagle and Champion Mine areas and prospect sites. Regularly spaced mineral deposits were plausibly formed along the fractures while deposit clusters were plausibly formed along the intersections of these fractures. The  $S_1$  foliation in the Ngubevu area has a nearly E-W trend. The model presented on the right-hand panel of the map indicates N-NE-directed compression which resulted in the formation of the fractures (dashed lines indicate the orientation of the foliation). This model is constructed for the two mines of interest and not the whole area because of a lack of data between the two mines (i.e., samples were only collected at the mines of interest).

### 9.3. SHORTCOMINGS OF THIS RESEARCH

The methodologies applied in this research are well-demonstrated for hydrothermal mineral deposits. However, the Tugela Terrane also hosts magmatic deposits in mafic and ultramafic bodies (Thomas et al., 1990). The methods employed here have not been demonstrated for such deposit types because the mineral deposits of interest should have characteristics indicative of structural control related to their formation/distribution from which their trends can then be extracted and related to geological structures (cf. Haddad-Martim et al., 2018). Therefore, to explore the mineral potential of this magmatic mineralisation in the Tugela Terrane may require different approaches to the ones used here.

Although this research has identified plausible structures related to mineral deposit formation/distribution in the micro- to local-scales of the Ngubevu area, it is difficult to assess from the data gathered which of these structures would be most permissive for mineral exploration. However, the results obtained from this research suggest a spatial association between mineral deposits and structures (Figure 9.2). In Figure 9.2C, parts of sample CM-24 where fractures have an apparent positive spatial association with mineral centroids are indicated in green while those with apparent negative spatial association are indicated in red. Mineral centroids with positive spatial association with micro-fractures occur preferably along micro-fractures with N–NNE orientations, such orientations in micro-fractures have also been identified for sample CM-24 (Table 4.2). In addition, the Fry analysis of points in sample CM-24 (Figure 6.3C) also identified preferred N-NNE trends in the alignment of mineral centroids. Mineral centroids with negative spatial association with fractures may be (a) associated with fractures that are not visible on the thin section or (b) sporadically distributed along inter-granular pore spaces in the sample.

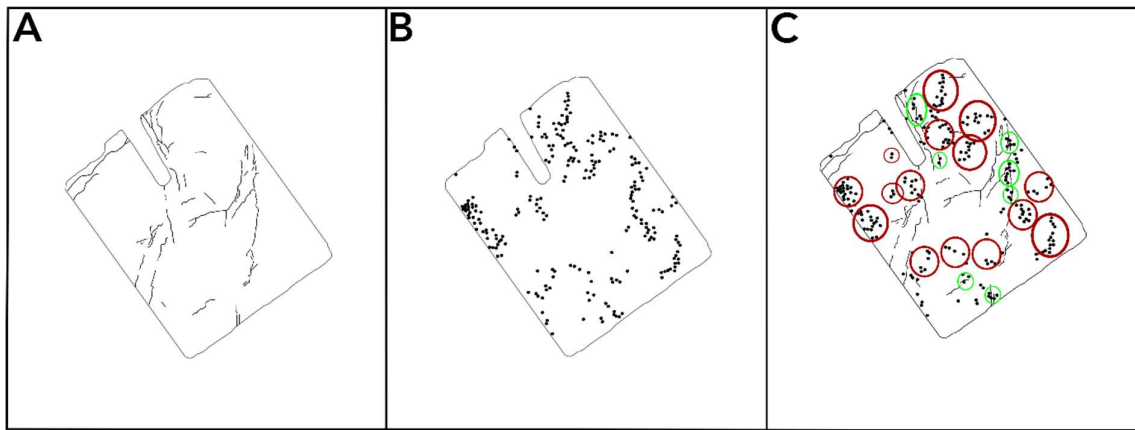


Figure 9.2: Micro-maps of sample CM-24 indicating (A) the micro-fracture pattern, (B) the micro-scale spatial pattern of centroids of spherulite grains and (C) the postulated spatial association between micro-fractures and mineral deposits in the study area.

#### 9.4. DELINEATING POTENTIAL EXPLORATION TARGETS

Regions with high potential for hosting mineral deposits can be delineated by mineral prospectivity prediction (MPP) (Ford and Hart, 2013). However, MPP or mineral potential mapping depends on the sufficiency and quality of data, and knowledge of mineral deposits in a certain region (Ford and Hart, 2013). The results of this research may be used in conceptual modelling of prospectivity as guides in the choice/generation of evidential layers for MPP to identify areas with the highest likelihood of occurrence of shear-zone-hosted precious and base metal mineralisation in the Ngubevu area (cf. Andrada de Palomera, 2004; Carranza, 2009; Parsa et al., 2017; Parsa and Maghsoudi, 2018). MPP in the Ngubevu area may also benefit from future research on understanding the shear-zone-hosted precious and base metal mineralisation in Natal Thrust Front, which would contribute to generation of more robust layers of spatial evidence and to better prediction of mineral prospectivity. In the closing chapter, the conclusions drawn from this micro-scale study of the shear-zone-hosted precious and base metal mineralisation in the Ngubevu area are provided. Some recommendations are also given for the exploration of other, structurally controlled, mineral deposits using the same methods applied in this study.

## **CHAPTER 10:**

### **CONCLUSIONS AND RECOMMENDATIONS**

#### **10.1. CONCLUSIONS**

This study aimed to understand whether certain micro-scale structural features of mineral deposits could be useful to providing insights to local-scale structural controls on shear-zone-hosted precious and base metal mineralisation in the Ngubevu area, in the Natal Thrust Front of the Tugela Terrane. In the light of the results obtained from the analyses discussed in this research, the following conclusions were made.

1. The occurrence/distribution of precious and base metal mineralisation in the micro-scale of the Ngubevu area is, as shown by the results of point pattern analysis (Chapter 5), non-random. The micro-scale patterns of ore minerals in the deposits examined show both regular and clustered spatial distributions.
2. Important micro-scale structures that plausibly controlled mineralisation in the study area, as revealed by Fry analysis (Chapter 6) and shape analysis (Chapter 8), are NNE–SSW- and NNW–SSE-trending sets of fractures, and nearly E–W-trending foliations. The intersections of these different sets of fractures and their intersections with foliations likely posed important structural controls on mineralisation in the Ngubevu area, whereby deposit clustering was plausibly formed at micro-scale.
3. The nature of structural controls on ore mineral occurrence/distribution in the Ngubevu area is fractal, and they functioned in at least two spatial scales. One type of structural control on mineralisation operated at spatial scales of at most 0.005  $\mu\text{m}$ , while another type of structural control operated at spatial scales of at least 0.002  $\mu\text{m}$ . The fractality of mineral deposits (Chapter 7) and structural controls in the micro-scale deduced from Fry and shape analyses (Chapters 6 and 8, respectively) suggest the presence of NNE–SSW- and NNW–SSE-trending sets of fractures and nearly E–W-trending foliations, and the intersections of such structures that controlled mineral deposit occurrence/distribution in at least the deposit- to local-scale of the Ngubevu area.
4. The spatial analytical methods employed during this research (i.e., point pattern, Fry, fractal, and shape analyses) are useful for studying the micro-scale features of mineral deposits; and the micro-scale features of structures and ore minerals are

useful for inferring local-scale structural controls on mineral deposit occurrence/distribution in the Ngubevu area.

## **10.2. RECOMMENDATIONS**

The following recommendations for further research on structurally controlled mineralisation within the Tugela Terrane and in the western Namaqua Province are made:

1. The methodologies employed in this study can be applied to study the epigenetic shear-zone-hosted precious and base metal mineralisation in the Mfongosi area, where mineralisation is hosted in quartz-feldspar veins of the Mfongosi Group like those investigated in this research (cf. Thomas et al., 1990; Bullen et al., 1994). Epigenetic shear-zone-hosted precious mineralisation has also been described in amphibolites and schists of the Tugela Group in the Tugela Nappe of the Natal Nappe Complex (cf. Thomas et al., 1990).
2. The posited spatial association between mineral deposits and structures in this research has not been quantified. This spatial association can be investigated further with distance-distribution analysis (Berman, 1977). This method quantifies the spatial association between geologic structures/features and mineral deposit occurrences and assists in recognising roles of lineament patterns associated with mineral deposit occurrences (Carranza, 2009; Parsa et al., 2017; Sun et al., 2018).
3. The suggested NNE–SSW and NNW–SSE trends of macro-fractures presented in this study are strongly supported by the micro-scale data analysis. However, it would be interesting to conduct Fry analysis of shear-zone-hosted precious and base metal mineral deposit distribution in other parts of the Tugela Terrane (e.g., Natal Nappe Zone) to examine whether the trends of mineral deposit points match the trends of macro-scale fractures presented in this study. Moreover, conducting structural mapping to identify the postulated NNE–SSW and NNW–SSE-trending macro-scale fractures would further assist in drawing an exploration strategy for the Ngubevu area to target such structures which could be potential hosts for mineral deposits.
4. In the western Namaqua Province, base metals have been exploited from rocks in the defunct Areachap, Kantienpan and Prieska-Copperton volcanogenic massive sulphide deposits/mines (Ghavami-Riabi, 2006; Rozendaal et al., 2017). To explore further the nature of structures that controlled mineralisation during deformation and

metamorphism at various spatial scales in this province and further the search for deposits, these spatial analytical methods can be employed.



## REFERENCES

- Agterberg, F.P., 2013. Fractals and spatial statistics of point patterns. *Journal of Earth Science*, 24(1): 1-11.
- Amirihanza, H., Shafieibafti, S., Derakhshani, R. and Khojastehfar, S., 2018. Controls on Cu mineralization in central part of the Kerman porphyry copper belt, SE Iran: constraints from structural and spatial pattern analysis. *Journal of Structural Geology*, 116: 159-177.
- Anders, M.H., Laubach, S.E. and Scholz, C.H., 2014. Microstructures: A review. *Journal of Structural Geology*, 69: 377-394.
- Andrada de Palomera, R.P., 2004. Application of Remote Sensing and Geographic Information Systems for Mineral Predictive Mapping, Deseado Massif, Southern Argentina. MSc Thesis, International Institute for Geo-Information Science and Earth Observation, Enschede, The Netherlands, 73 pp.
- Arima, M. and Johnston, S.T., 2001. Crustal evolution of the Tugela terrane, Natal belt, South Africa. *Gondwana Research*, 4: 563-564.
- Arima, M., Tani, K., Kawate, S. and Johnston, S.T., 2001. Geochemical characteristics and tectonic setting of metamorphosed rocks in the Tugela terrane, Natal belt, South Africa. *Memoir, National Institute of Polar Research, Tokyo, Japan, Special Issue No. 55: 1-39.*
- Austin, J. and Blenkinsop, T.G., 2009. Local to regional scale structural controls on mineralisation and the importance of a major lineament in the eastern Mount Isa Inlier, Australia: review and analysis with autocorrelation and weights of evidence. *Ore Geology Reviews*, 35(3-4): 298-316.
- Barkhuizen, J.G. and Matthews, P.E., 1990. Gravity modelling of the Natal Thrust Front: a Mid-Proterozoic crustal suture in southeastern Africa. *Extended Abstracts, Geological Society of South Africa, Geocongress*, 90: 32-35.
- Basson, I.J., 2000. The Structural, Metamorphic and Tectonic Context of Selected Sub-Economic Veining in the Natal Thrust Front and Natal Nappe Zone, Northern KwaZulu-Natal. PhD Thesis, University of Natal, Durban, 362 pp.
- Basson, I.J. and Watkeys, M.K., 2000. Structural and stratigraphic setting of gold and base metal deposits in the Natal Thrust Front, South Africa. In: J.K. Cluer., J.G. Price., E.M. Struhsacker., R.F. Hardyman., and C.L. Morris (Editors), *Geology and Ore Deposits -*

- The Great Basin and Beyond. Geological Society of Nevada Symposium Proceedings, pp. 571-582.
- Basson, I.J. and Watkeys, M.K., 2003. Tectonic implications from the geochemistry of Mfongosi Group metasediments, Natal Metamorphic Province, South Africa. *South African Journal of Geology*, 106(4): 265-280.
- Basson, I.J., Watkeys, M.K. and Phillips, D., 2005. Structural evolution and tectonic context of the Mfongosi Group, Natal thrust front, Tugela terrane, South Africa. *Journal of African Earth Sciences*, 43(4): 415-432.
- Berman, M., 1977. Distance distributions associated with Poisson processes of geometric figures. *Journal of Applied Probability*, 14(1): 195-199.
- Bisnath, A., 2000. Geology of the Tugela Group Rocks in the Nsuze River Valley, Tugela Terrane, Natal Belt, South Africa. MSc Thesis, University of Durban-Westville, South Africa, 110pp.
- Bisnath, A., McCourt, S., Frimmel, H.E. and Buthelezi, S.B.N., 2008. The metamorphic evolution of mafic rocks in the Tugela Terrane, Natal Belt, South Africa. *South African Journal of Geology*, 111(4): 369-386.
- Blenkinsop, T.G., 2002. *Deformation Microstructures and Mechanisms in Minerals and Rocks*. Kluwer Academic Publishers, New York, 150 pp.
- Blenkinsop, T.G., 2004. Orebody geometry in lode gold deposits from Zimbabwe: implications for fluid flow, deformation and mineralization. *Journal of Structural Geology*, 26(6-7): 1293-1301.
- Blenkinsop, T.G. and Sanderson, D.J., 1999. Are gold deposits in the crust fractals? A study of gold mines in the Zimbabwe craton. Geological Society, London, Special Publications, 155(1): 141-151.
- Boots, B.N. and Getis, A., 1988. *Point pattern analysis: Sage University Scientific Geography Series no. 8*. Sage Publications, Beverly Hills, 69 pp.
- Bullen, W.D., Thomas, R.J. and McKenzie, A., 1994. Gold mineralisation in Natal, South Africa. *Journal of African Earth Sciences*, 18(2): 99-109.
- Carafa, M.M.C. and Barba, S., 2013. The stress field in Europe: optimal orientations with confidence limits. *Geophysical Journal International*, 193(2): 531-548.
- Carranza, E.J.M., 2008. Geochemical anomaly and mineral prospectivity mapping in GIS. *Handbook of Exploration and Environmental Geochemistry*, 11. Elsevier, 351pp.

- Carranza, E.J.M., 2009. Controls on mineral deposit occurrence inferred from analysis of their spatial pattern and spatial association with geological features. *Ore Geology Reviews*, 35(3-4): 383-400.
- Carranza, E.J.M., de Souza Filho, C.R., Haddad-Martim, P.M., Nagayoshi, K. and Shimizu, I., 2019. Macro-scale ore-controlling faults revealed by micro-geochemical anomalies. *Scientific reports*, 9(1): 4410.
- Carranza, E.J.M., Owusu, E.A. and Hale, M., 2009. Mapping of prospectivity and estimation of number of undiscovered prospects for lode gold, southwestern Ashanti Belt, Ghana. *Mineralium Deposita*, 44(8): 915-938.
- Cornell, D.H., Thomas, R.J., Bowring, S.A., Armstrong, R.A. and Grantham, G.H., 1996. Protolith interpretation in metamorphic terranes: a back-arc environment with Besshi-type base metal potential for the Quha Formation, Natal Province, South Africa. *Precambrian Research*, 77(3-4): 243-271.
- Crampton, J.S., 1995. Elliptic Fourier shape analysis of fossil bivalves: some practical considerations. *Lethaia*, 28: 179-186.
- De Klerk, I.D., 1991. The Nature and Origin of Gold Mineralization in the Tugela Valley, Natal Structural and Metamorphic Province. MSc Thesis, Rhodes University, 113 pp.
- Diggle, P.J., 1983. *Statistical Analysis of Spatial Point Patterns*. Academic Press, London, 148 pp.
- Diggle, P.J., 2013. *Statistical analysis of spatial and spatio-temporal point patterns*. CRC press, 262 pp.
- Duncan, R.J., Hitzman, M.W., Nelson, E.P. and Togtokhbayar, O., 2014. Structural and lithological controls on iron oxide copper-gold deposits of the southern Selwyn-Mount Dore corridor, Eastern fold belt, Queensland, Australia. *Economic Geology*, 109(2): 419-456.
- Eglington, B.M., Harmer, R.E. and Kerr, A., 1989. Isotope and geochemical constraints on Proterozoic crustal evolution in south-eastern Africa. *Precambrian Research*, 45(1-3): 159-174.
- Eglington, B.M., Thomas, R.J., Armstrong, R.A. and Walraven, F., 2003. Zircon geochronology of the Oribi Gorge Suite, KwaZulu-Natal, South Africa: Constraints on the timing of trans-current shearing in the Namaqua–Natal Belt. *Precambrian Research*, 123(1): 29-46.

- Fabbri, A.G., van der Meer, F.D., Velanzuela, C.R. and Kushigbor, C.A., 1993. Shape analysis and multispectral classification in geological remote sensing. *Mathematical Geology*, 25(7): 774-793.
- Fils, S.C.N., Mimba, M.E., Nyeck, B., Nforba, M.T., Kankeu, B., Nouck, P.N. and Hell, J.V., 2020. GIS-Based Spatial Analysis of Regional-Scale Structural Controls on Gold Mineralization along the Bétaré-Oya Shear Zone, Eastern Cameroon. *Natural Resources Research*, 29: 3457-3477.
- Ford, A. and Hart, C.J.R., 2013. Mineral potential mapping in frontier regions: A Mongolian case study. *Ore Geology Reviews*, 51: 15-26.
- Fry, N., 1979. Random point distributions and strain measurement in rocks. *Tectonophysics*, 60(1-2): 89-105.
- Ghavami-Riabi, R., 2006. Geochemical exploration for base metal sulphide deposits in an arid environment (eastern Namaqua Metamorphic Province), South Africa. PhD Thesis, University of Pretoria, 306 pp.
- Ghazvinian, E., Diederichs, C.H. and Rai, C.S. 2016. 3D random Voronoi grain-based models for simulation of brittle rock damage and fabric-guided micro-fracturing. *Journal of Rock Mechanics and Geotechnical Engineering*, 6, 506-521.
- Giner-Robles, J.L., Pérez-López, R., Silva, P.G., Jiménez-Díaz, A. and Rodríguez-Pascua, M.A., 2012. Recent tectonic model of the Upper Tagus Basin (central Spain). *Journal of Iberian Geology*, 38: 113-126.
- Goryainov, P.M., Ivanyuk, G.Y. and Sharov, N.V., 1997. Fractal analysis of seismic and geological data. *Tectonophysics*, 269(3-4): 247-257.
- Haddad-Martim, P.M., Carranza, E.J.M. and de Souza Filho, C.R., 2018. The fractal nature of structural controls on ore formation: the case of the iron oxide copper-gold deposits in the Carajás Mineral Province, Brazilian Amazon. *Economic Geology*, 113(7): 1499-1524.
- Haddad-Martim, P.M., de Souza Filho, C.R. and Carranza, E.J.M., 2017. Spatial analysis of mineral deposit distribution: A review of methods and implications for structural controls on iron oxide-copper-gold mineralization in Carajás, Brazil. *Ore Geology Reviews*, 81: 230-244.
- Hanna, S.S. and Fry, N., 1979. A comparison of methods of strain determination in rocks from southwest Dyfed (Pembrokeshire) and adjacent areas. *Journal of Structural Geology*, 1(2): 155-162.

- Hansen, V. L., 1990. Collection and preparation of thin sections of oriented samples. *Journal of Geological Education*, 38(4): 294-297.
- Heilbronner, R. and Barrett, S., 2014. *Image Analysis in Earth Sciences: Microstructures and Textures of Earth Materials*. Springer, Berlin, Heidelberg, 520 pp.
- Heilbronner, R. and Keulen, N., 2006. Grain size and grain shape analysis of fault rocks. *Tectonophysics*, 427: 199-216.
- Hodkiewicz, P.F., Weinberg, R.F., Gardoll, S.J. and Groves, D.I., 2005. Complexity gradients in the Yilgarn Craton: fundamental controls on crustal-scale fluid flow and the formation of world-class orogenic-gold deposits. *Australian Journal of Earth Sciences*, 52(6): 831-841.
- Hoek, E. and Brown, E.T. 1980. Empirical strength criterion for rock masses. *Journal of Geotechnical Engineering Division*, 106, <https://doi.org/10.1061/AJGEB6.0001029>.
- Jacobs, J. and Thomas, R.J., 1994. Oblique collision at about 1.1 Ga along the southern margin of the Kaapvaal continent, south-east Africa. *Geologische Rundschau*, 83(2): 322-333.
- Jacobs, J., Thomas, R.J. and Weber, K., 1993. Accretion and indentation tectonics at the southern edge of the Kaapvaal craton during the Kibaran (Grenville) orogeny. *Geology*, 21(3): 203-206.
- Johnston, S.T., Armstrong, R., Heaman, L., McCourt, S., Mitchell, A., Bisnath, A. and Arima, M., 2001. Preliminary U-Pb geochronology of the Tugela terrane, Natal belt, eastern South Africa. *Memoirs of National Institute of Polar Research. Special issue (55)*: 40-58.
- Johnston, S.T., McCourt, S., Bisnath, A. and Mitchell, A.A., 2003. The Tugela Terrane, Natal belt: Kibaran magmatism and tectonism along the southeast margin of the Kaapvaal Craton. *South African Journal of Geology*, 106(1): 85-97.
- Kranz, R.L., 1983. Microcracks: A Review. *Tectonophysics*, 100: 449-480.
- Laing, W.P., 2004. Tension vein arrays in progressive strain: complex but predictable architecture, and major hosts of ore deposits. *Journal of Structural Geology*, 26(6-7): 1303-1315.
- Laubach, S.E., 1989. Paleostress directions from the preferred orientation of closed microfractures (fluid-inclusion planes) in sandstone, East Texas basin, USA. *Journal of Structural Geology*, 11(5): 603-611.

- Laubach, S.E., 1997. A method to detect natural fracture strike in sandstones. *American Association of Petroleum Geologists Bulletin*, 81(4): 604-623.
- Laubach, S.E. and Diaz-Tushman, K., 2009. Laurentian palaeostress trajectories and ephemeral fracture permeability, Cambrian Eriboll Formation sandstones west of the Moine Thrust Zone, NW Scotland. *Journal of the Geological Society*, 166(2): 349-362.
- Launeau, P. and Cruden, A., 1994. Mineral recognition in digital images of rocks: A new approach using multichannel classification. *The Canadian Mineralogist*, 32, 919-933.
- Launeau, P., Bouchez, J.-L. and Benn, K., 1990. Shape preferred orientation of object populations: automatic analysis of digitized images. *Tectonophysics*, 180, 201-211.
- Launeau, P. and Robin, P.-Y.F., 1996. Fabric analysis using the intercept method. *Tectonophysics*, 267, 91-119.
- Lloyd, C.D., 2007. *Local Models for Spatial Analysis*. CRC/Taylor & Francis, Boca Raton, 244 pp.
- Lu, G., Zhou, J., Li, Y., Zhang, X. and Gao, W. 2020. The influence of minerals on the mechanism of wave-induced fracturing of rocks. *Journal of Applied Geophysics*, 180, 104123.
- Maanijou, M., Daneshvar, N., Alipoor, R. and Azizi, H., 2020. Spatial Analysis on Gold Mineralization in Southwest Saqqez Using Point Pattern, Fry and Fractal Analyses *Geotectonics*, 54: 589-604.
- Mamuse, A., Porwal, A., Kreuzer, O. and Beresford, S., 2010. Spatial statistical analysis of the distribution of komatiite-hosted nickel sulfide deposits in the Kalgoorlie terrane, Western Australia: clustered or not? *Economic Geology*, 105(1): 229-242.
- Mandelbrot, B.B., 1977. *Fractals: Form, Chances and Dimension*. W.H. Freeman, New York, 384pp.
- Mandelbrot, B.B., 1983. *The fractal geometry of nature*, 173. WH freeman New York, 495 pp.
- Matthews, P.E., 1972. Possible Precambrian obduction and plate tectonics in southeastern Africa. *Nature* (240): 37-39.
- Matthews, P.E., 1981. Eastern or Natal sector of the Namaqua-Natal Mobile Belt in Southern Africa. In: D.R. Hunter (Editor), *Precambrian of the Southern Hemisphere*. Elsevier, Amsterdam, pp. 705-725.

- McCourt, S., Armstrong, R.A., Grantham, G.H. and Thomas, R.J., 2006. Geology and evolution of the Natal belt, South Africa. *Journal of African Earth Sciences*, 46(1-2): 71-92.
- Mendonidis, P. and Thomas, R.J., 2019. A review of the geochronology of the Margate Terrane reveals a history of diachronous terrane docking and arc accretion across the Mesoproterozoic Natal belt, southeastern Africa. *Journal of African Earth Sciences*, 150: 532-545.
- Mighani, S., Sondergeld, C.H. and Rai, C.S. 2016. Observations of rock tensile fracturing of anisotropic rocks. *SPE Journal*, 21(4), 1289-1301.
- Mizuno, T., Ito, H., Kuwahara, Y., Imanishi, K. and Takeda, T., 2005. Spatial variation of shear-wave splitting across an active fault and its implication for stress accumulation mechanism of inland earthquakes: The Atotsugawa fault case. *Geophysical Research Letters*, 32(20): L20305.
- Morley, C.K., 2010. Stress re-orientation along zones of weak fabrics in rifts: An explanation for pure extension in 'oblique' rift segments? *Earth and Planetary Science Letters*, 297(3-4): 667-673.
- Mukherjee, S., 2013. *Deformation Microstructures in Rocks*. Springer, Heidelberg, Berlin, 111 pp.
- Munro, M.A., Ord, A. and Hobbs, B.E., 2018. Spatial organization of gold and alteration mineralogy in hydrothermal systems: wavelet analysis of drillcore from Sunrise Dam Gold Mine, Western Australia. *Geological Society, London, Special Publications*, 453(1): 165-204.
- Nicholson, R. and Pollard, D.D. 1985. Dilution and linkage of echelon cracks. *Journal of Structural Geology*, 7(5), 583-590.
- Niu, H., Liu, S., Lai, J., Wang, G., Liu, B., Xie, Y. and Xie, W., 2020. In-situ stress determination and fracture characterization using image logs: The Paleogene Dongying Formation in Nanpu Sag, Bohai Bay Basin, China. *Energy Science & Engineering*, 8(2): 476-489.
- Ortega, O. and Marrett, R., 2000. Prediction of macrofracture properties using microfracture information, Mesaverde Group sandstones, San Juan basin, New Mexico. *Journal of Structural Geology*, 22(5): 571-588.
- Parsa, M. and Maghsoudi, A., 2018. Controls on Mississippi Valley-Type Zn-Pb mineralization in Behabad district, Central Iran: Constraints from spatial and numerical analyses. *Journal of African Earth Sciences*, 140: 189-198.

- Parsa, M., Maghsoudi, A. and Yousefi, M., 2017. An improved data-driven fuzzy mineral prospectivity mapping procedure; cosine amplitude-based similarity approach to delineate exploration targets. *International Journal of Applied Earth Observation and Geoinformation*, 58: 157-167.
- Reynolds, I.M., 1986. The mineralogy of some vanadium bearing titaniferous iron ores of the Mambula Complex, Zululand. In: C.R. Anhaeusser and S. Maske (Editors), *Mineral Deposits of Southern Africa Geological Society of South Africa, South Africa* pp. 1695-1708.
- Rozendaal, A., Rudnick, T.-K. and Heyn, R., 2017. Mesoproterozoic base metal sulphide deposits in the Namaqua Sector of the Namaqua-Natal Metamorphic Province, South Africa: a review. *South African Journal of Geology*, 120(1): 153-186.
- Sharib, A.S.A.A.A., Reinhardt, J. and McCourt, S., 2021. Structural diversity within a thrust complex reflecting progressive overprinting during a protracted orogenic process of terrane accretion, Natal belt, South Africa. *Journal of Structural Geology*, 142: 104-231.
- Simmons, G. and Richter, D., 1976. Microcracks in Rock. In: R.G.J. Strens (Editor), *The Physics and Chemistry of Minerals and Rocks*. Wiley, New York, pp. 105-137.
- Smalley, T.J., 1979. Structure and metamorphism of the Tugela Group within the northern zone of the Natal Mobile Belt. PhD Thesis, University of Natal, Durban, South Africa, 220 pp.
- Spencer, C.J., Thomas, R.J., Roberts, N.M.W., Cawood, P.A., Millar, I. and Tapster, S., 2015. Crustal growth during island arc accretion and transcurrent deformation, Natal Metamorphic Province, South Africa: new isotopic constraints. *Precambrian Research*, 265: 203-217.
- Sun, T., Xu, Y., Yu, X., Liu, W., Li, R., Hu, Z. and Wang, Y., 2018. Structural Controls on Copper Mineralization in the Tongling Ore District, Eastern China: Evidence from Spatial Analysis. *Minerals*, 8: 254-279.
- Thomas, R.J., 1989. A tale of two tectonic terranes. *South African Journal of Geology*, 92(4): 306-321.
- Thomas, R.J., Ashwal, L.D. and Andreoli, M.A.G., 1992. The petrology of the Turtle Bay Suite: a mafic-felsic granulite association from southern Natal, South Africa. *Journal of African Earth Sciences (and the Middle East)*, 15(2): 187-206.

- Thomas, R.J., Bullen, W.D., De Klerk, I. and Scogings, A.J., 1990. The distribution and genesis of precious and base metal mineralisation in the Natal Metamorphic Province, South Africa. *South African Journal of Geology*, 93(4): 683-695.
- Thomas, R.J. and Gain, S.B., 1989. The geological setting of gold mineralisation at Dumisa, Natal. *South African Journal of Geology*, 92(4): 410-419.
- Turcotte, D.L., 1989. Fractals in geology and geophysics. *Pure and Applied Geophysics*, 131(1-2): 171-196.
- van der Pluijm, B. A. and Marshak, S. 2004. *Earth Structure: An Introduction to Structural Geology and Tectonics*, New York, Norton and Company, 656pp.
- Vearncombe, J. and Vearncombe, S., 1999. The spatial distribution of mineralization: applications of Fry analysis. *Economic Geology*, 94: 475-486.
- Velandia, F., García-Delgado, H., Zuluaga, C.A., López, J.A., and Bermúdez, M.A., 2020. Present-day structural frame of the Santander Massif and Pamplona Wedge: The interaction of the Northern Andes. *Journal of Structural Geology*, 137: 104087.
- Vermilye, J.M. and Scholz, C.H., 1998. The process zone: A microstructural view of fault growth. *Journal of Geophysical Research: Solid Earth*, 103(B6): 12223-12237.
- Watkins, H., Butler, R.W.H., Bond, C.E. and Healy, D., 2015. Influence of structural position on fracture networks in the Torridon Group, Achnashellach fold and thrust belt, NW Scotland. *Journal of Structural Geology*, 74, 64-80.
- Wuth, M.G. and Archer, P.D., 1986. Chromite mineralisation at Sithilo, northern Zululand. In: C.R. Anhaeusser and S. Maske (Editors), *Mineral Deposits of Southern Africa*, II. Geological Society of South Africa, Johannesburg, pp. 1694.
- Zhong, J., Liu, S., Ma, Y., Yin, C., Liu, C., Li, Z., Liu, X. and Li, Y., 2015. Macro-fracture mode and micro-fracture mechanism of shale. *Petroleum Exploration and Development*, 42: 269-276.
- Zoback, M.D., 2010. *Reservoir geomechanics*. Cambridge University Press, 505 pp.



**APPENDIX A:**  
**SPATIAL DISTRIBUTION OF CENTROIDS OF SPHALERITE GRAINS IN THIN**  
**SECTIONS OF SAMPLES FROM THE STUDY AREA**

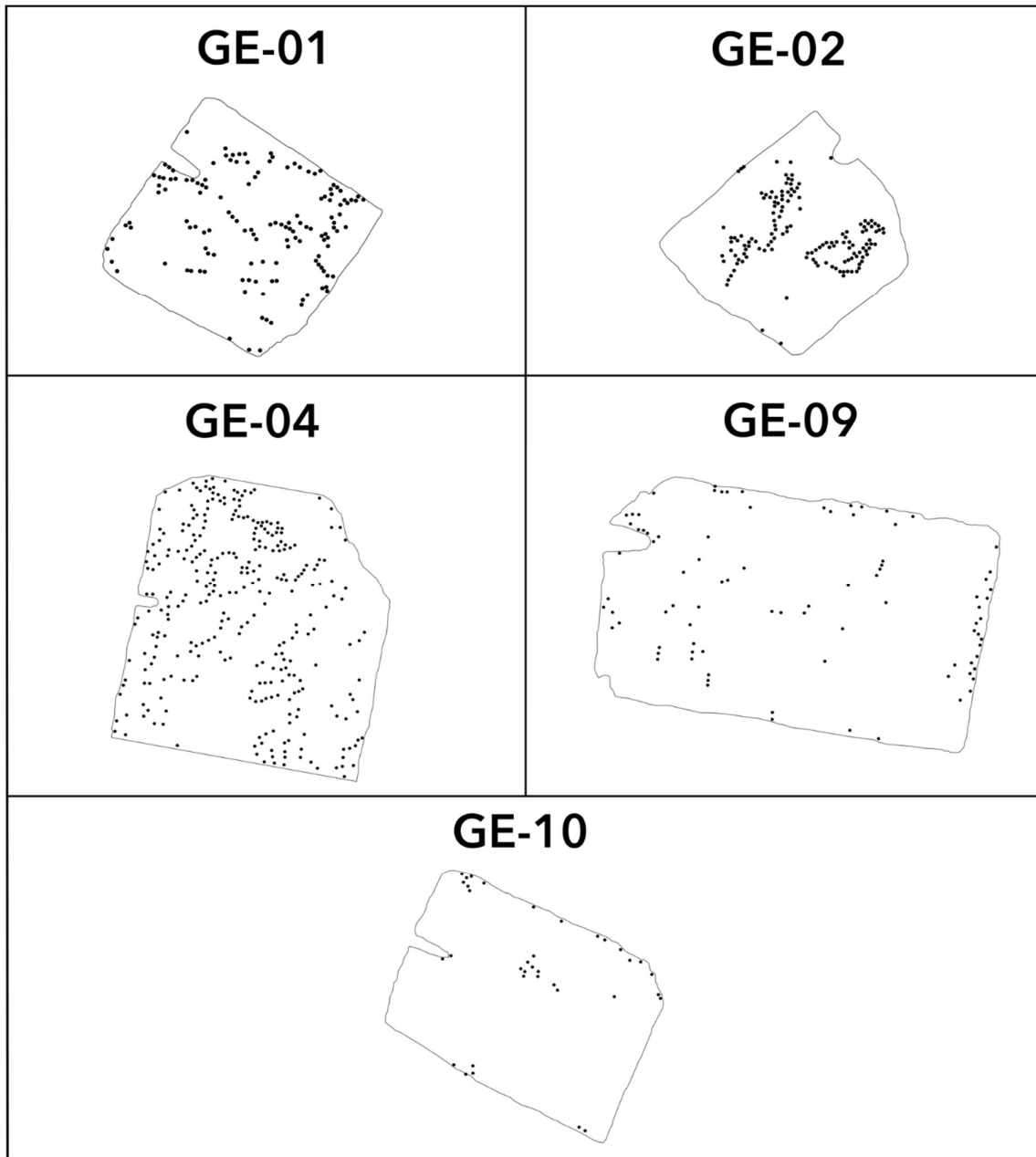


*Figure A.1: Spatial distribution of centroids of sphalerite grains in thin sections of samples from the Golden Eagle mine area and prospect site.*

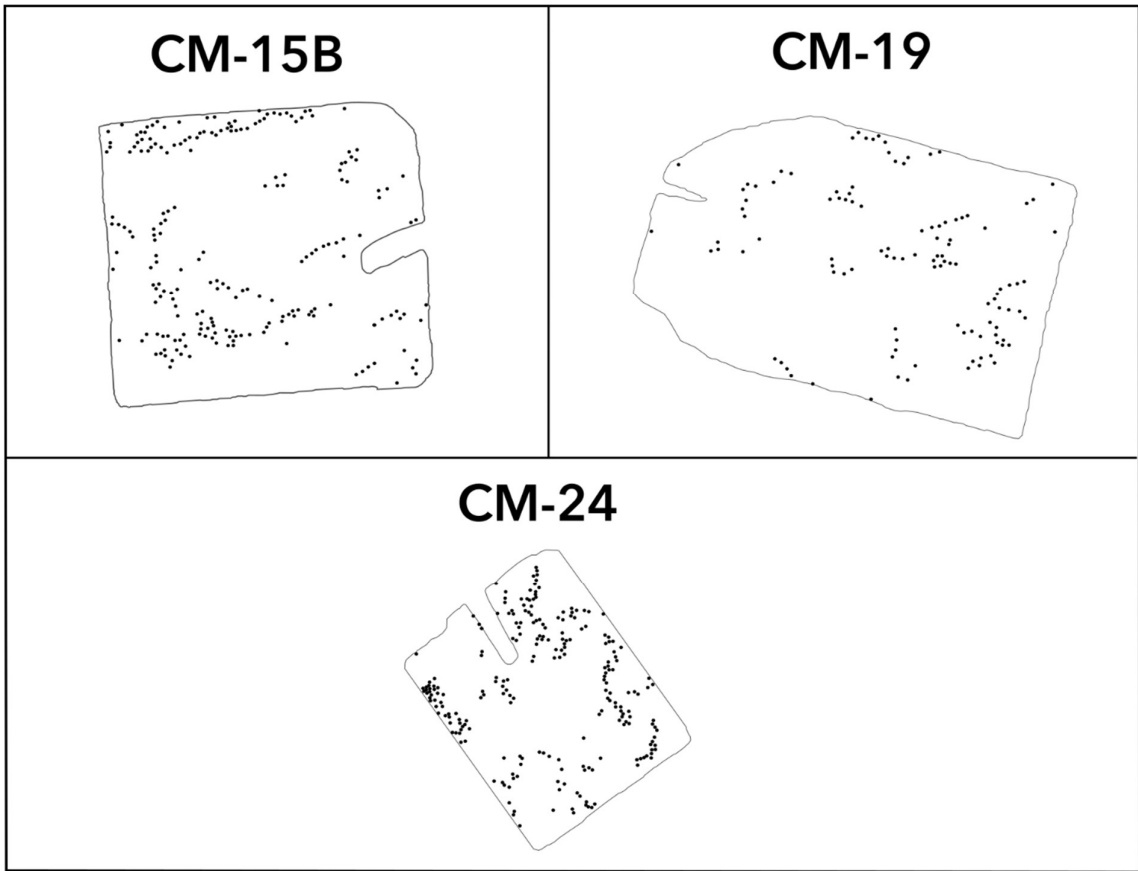


*Figure A.2: Spatial distribution of centroids of spherulite grains in thin sections of samples from the Champion Mine and prospect site.*

**APPENDIX B:**  
**SPATIAL DISTRIBUTION OF FRY POINTS PLOTTED FOR THIN SECTIONS OF**  
**SAMPLES FROM THE STUDY AREA**

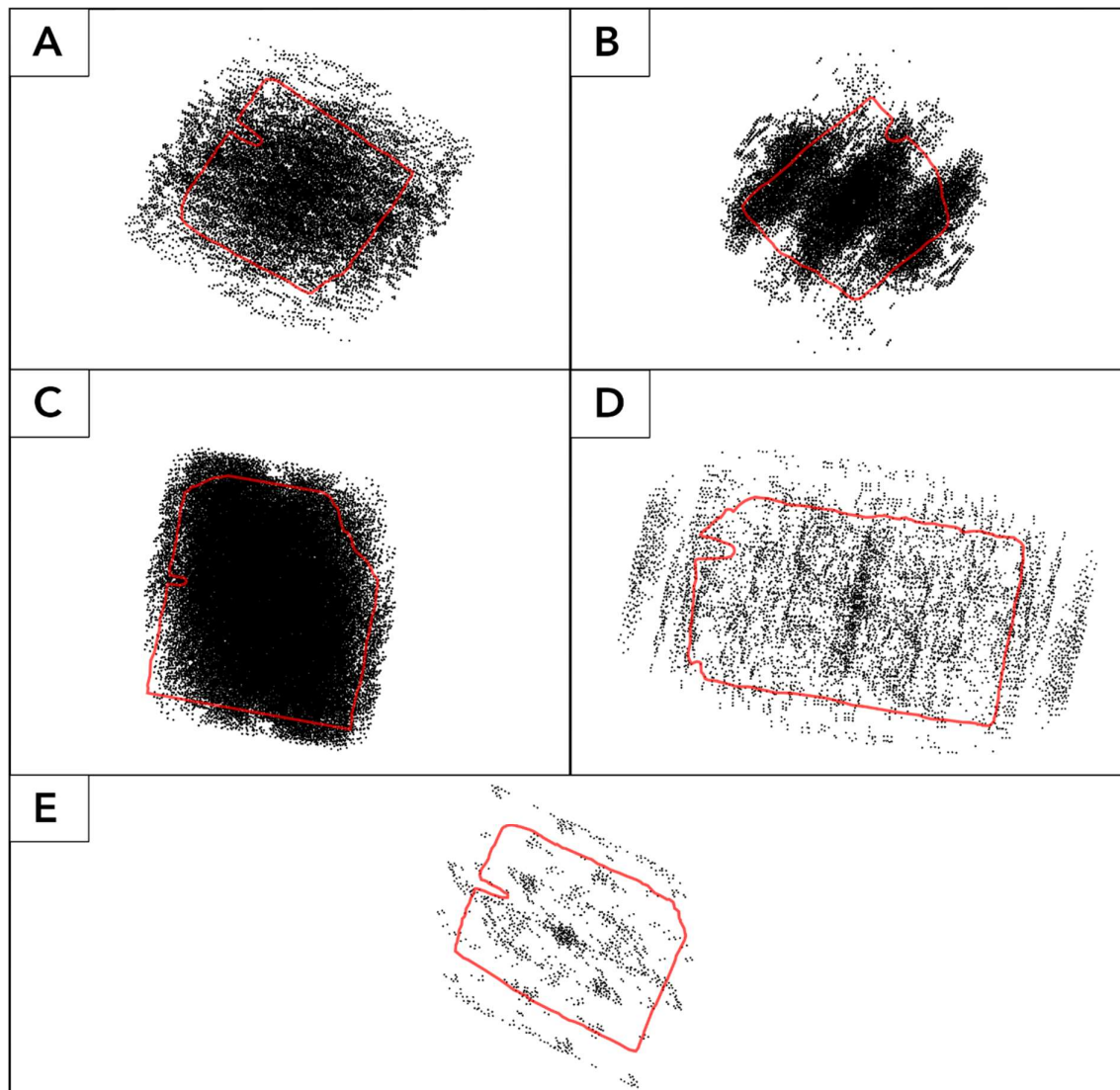


*Figure B.1. Spatial distribution of Fry points plotted for thin sections of samples from the Golden Eagle mine and prospect site. (A) GE-01, (B) GE-02, (C) GE-04, (D) GE-09 and (E) GE-10.*

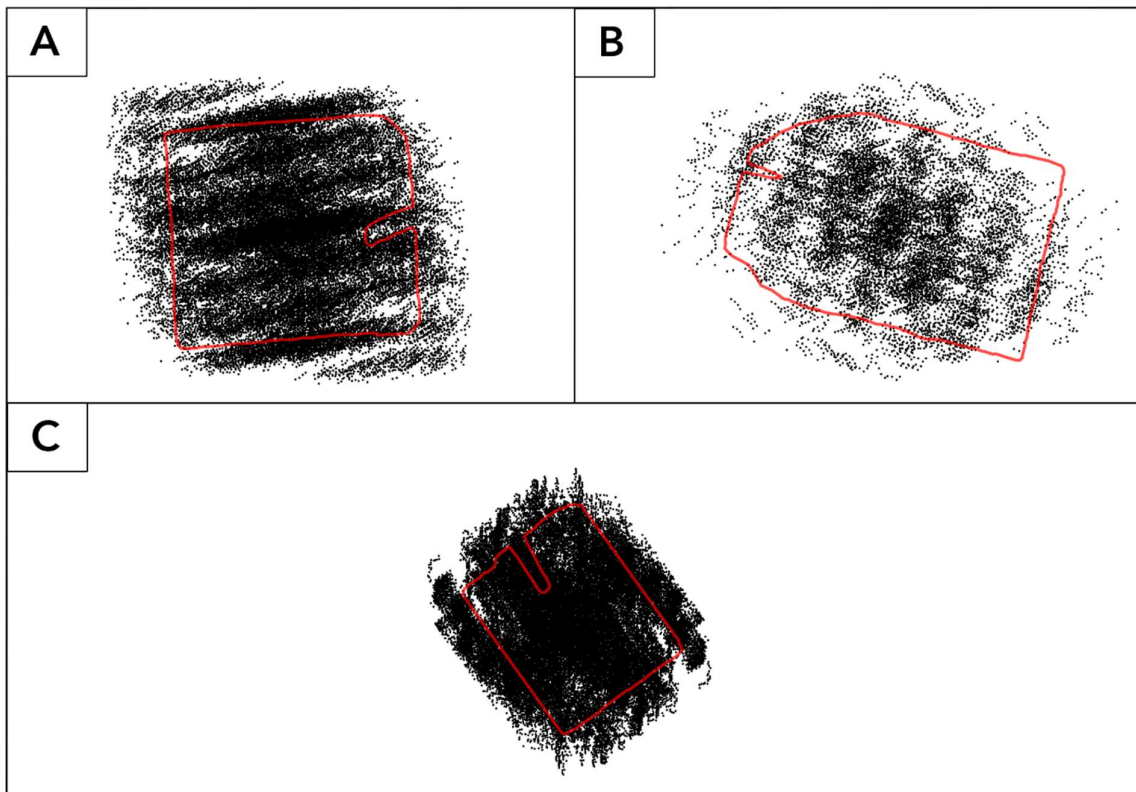
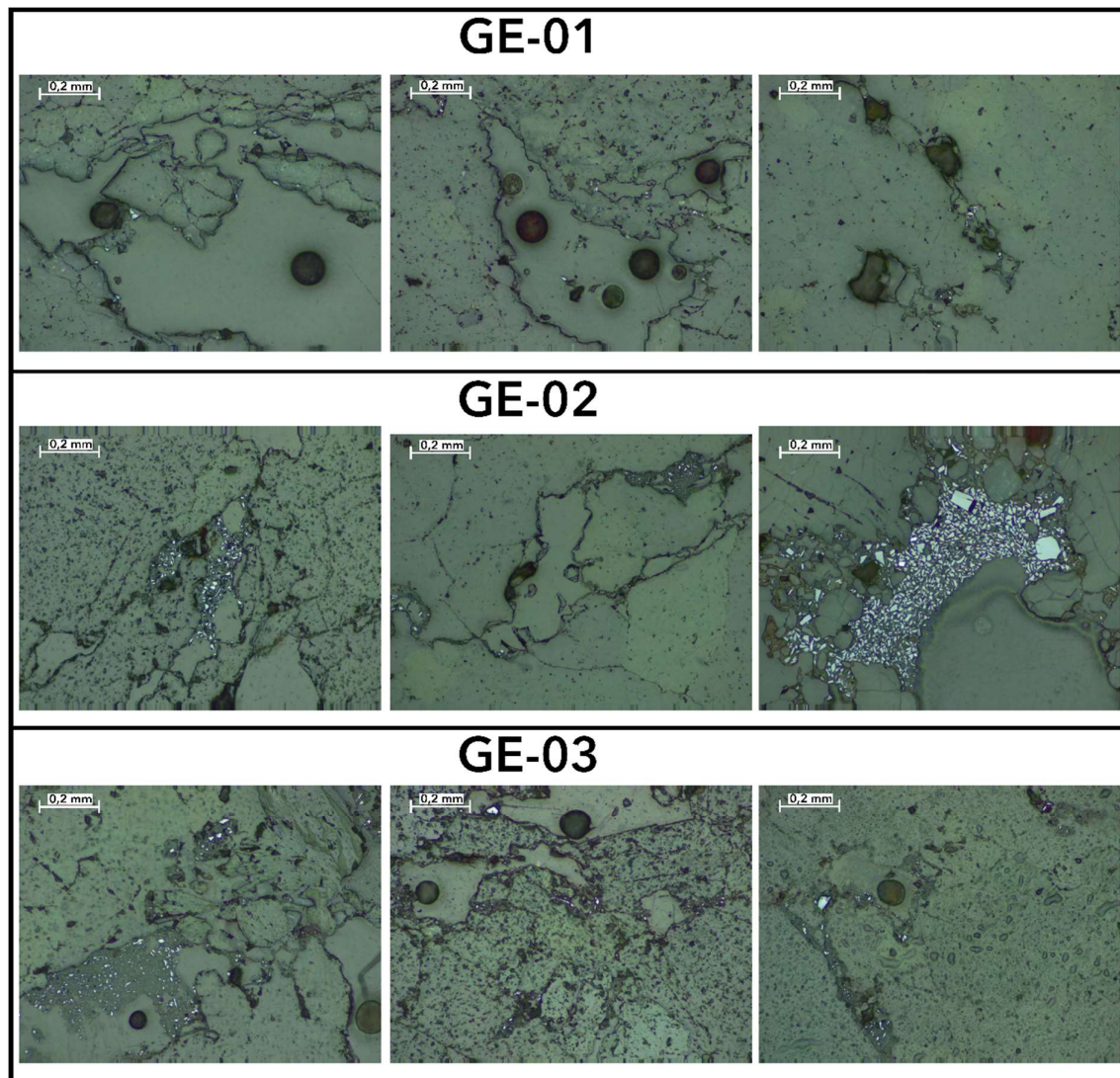
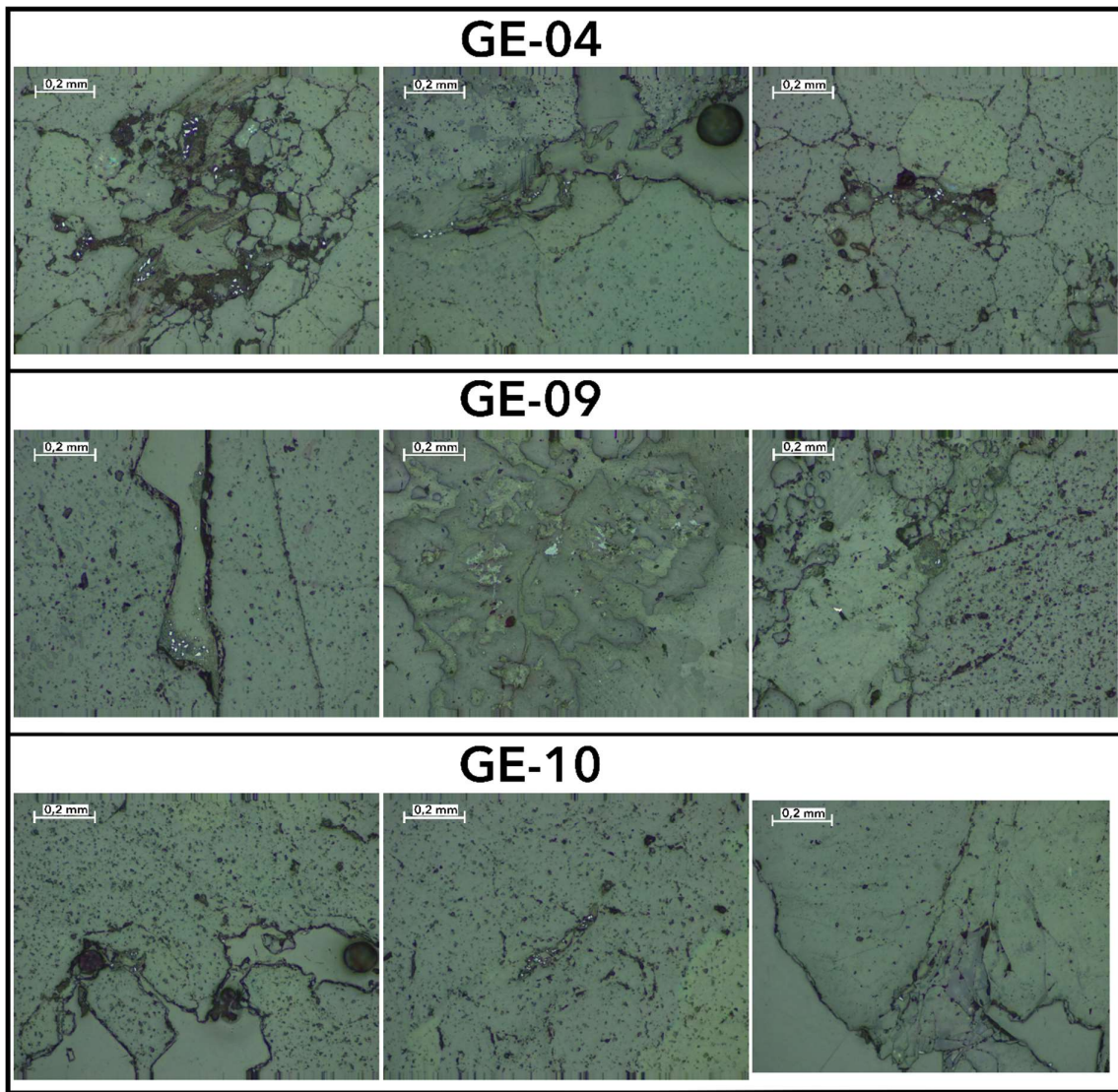


Figure B.1. Spatial distribution of Fry points plotted for thin sections of samples from the Champion Mine and prospect site. (A) CM-15B, (B) CM-19, (C) CM-24.

**APPENDIX C:**  
**ORIENTED PHOTOMICROGRAPHS OF THIN SECTIONS OF SAMPLES FROM THE**  
**STUDY AREA**



*Figure C.1: Oriented photomicrographs of thin sections of samples from the Golden Eagle mine area and prospect site. The light grey areas are occupied by sphalerite grains while the darker grey areas are occupied by gangue minerals comprising quartz, plagioclase feldspar, and minor biotite. North is parallel to the long edge of the page border all in images.*



*Figure C.2: Oriented photomicrographs of thin sections of samples from the Golden Eagle mine area and prospect site. The light grey areas are occupied by sphalerite grains while the darker grey areas are occupied by gangue minerals comprising quartz, plagioclase feldspar, and minor biotite. North is parallel to the long edge of the page border in all images.*

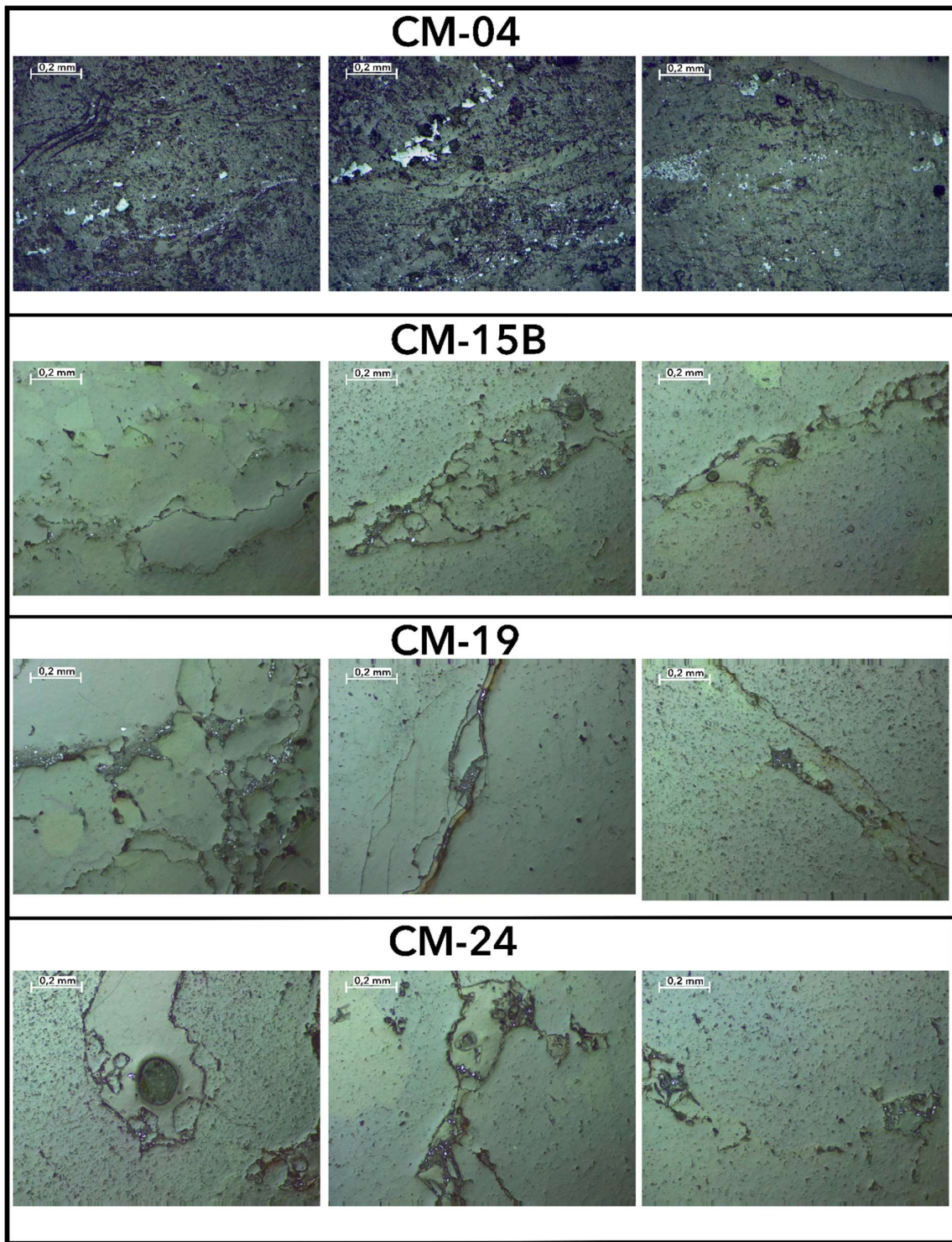
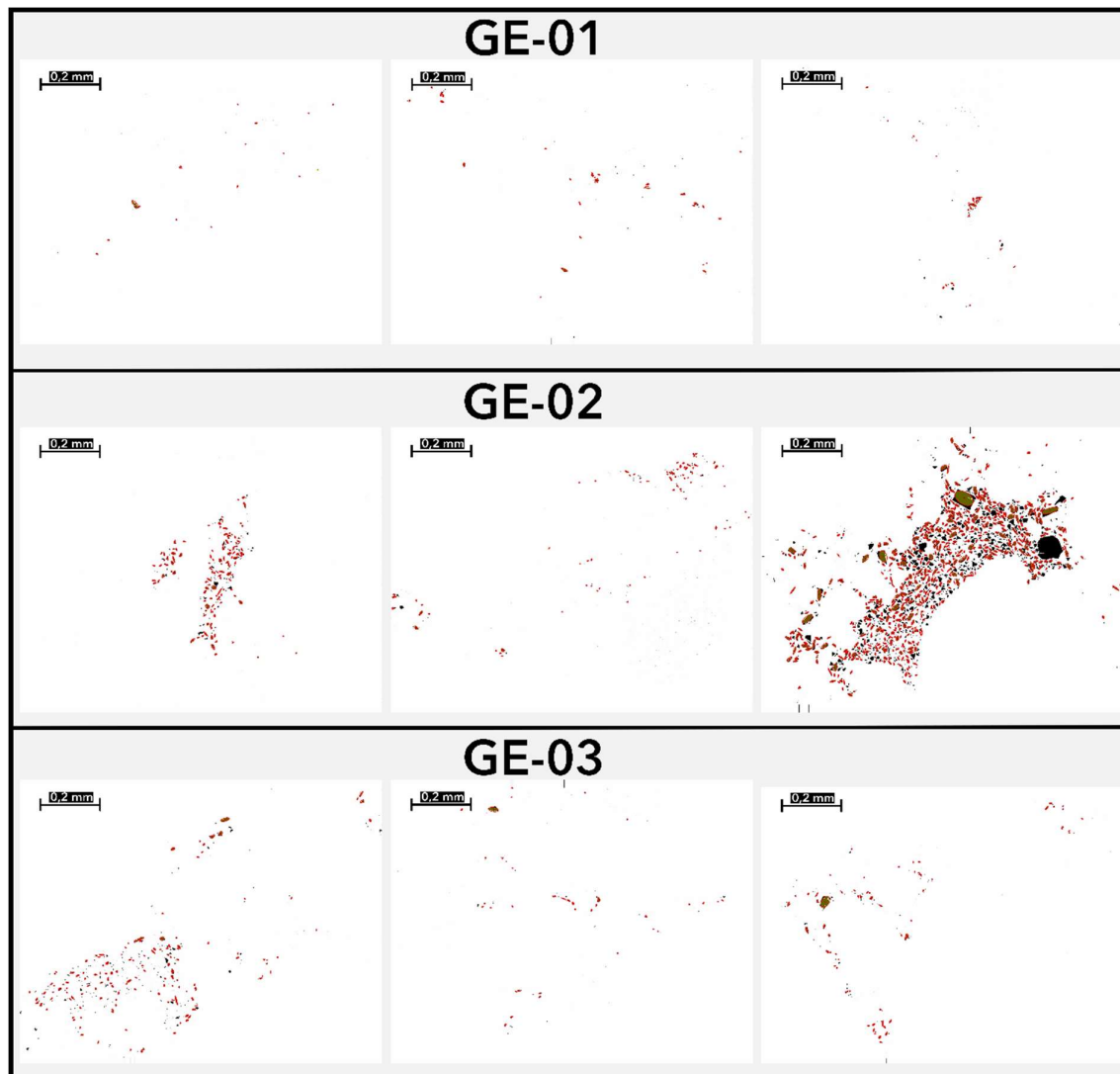


Figure C.3: Oriented photomicrographs of thin sections of samples from the Champion Mine area and prospect site. The light grey areas are occupied by sphalerite grains while the darker grey areas are occupied by gangue minerals comprising quartz, plagioclase feldspar, and minor biotite. North is parallel to the long edge of the page border in all images.



**APPENDIX D:**  
**BINARY IMAGES OF SPHALERITE GRAINS IN ORIENTED THIN SECTIONS OF**  
**SAMPLES FROM THE STUDY AREA FITTED WITH BEST-FIT ELLIPSES**



*Figure D.1: Binary images of sphalerite grains in oriented photomicrographs of thin sections of samples from the Golden Eagle mine area and prospect site fitted with best-fit ellipses.*

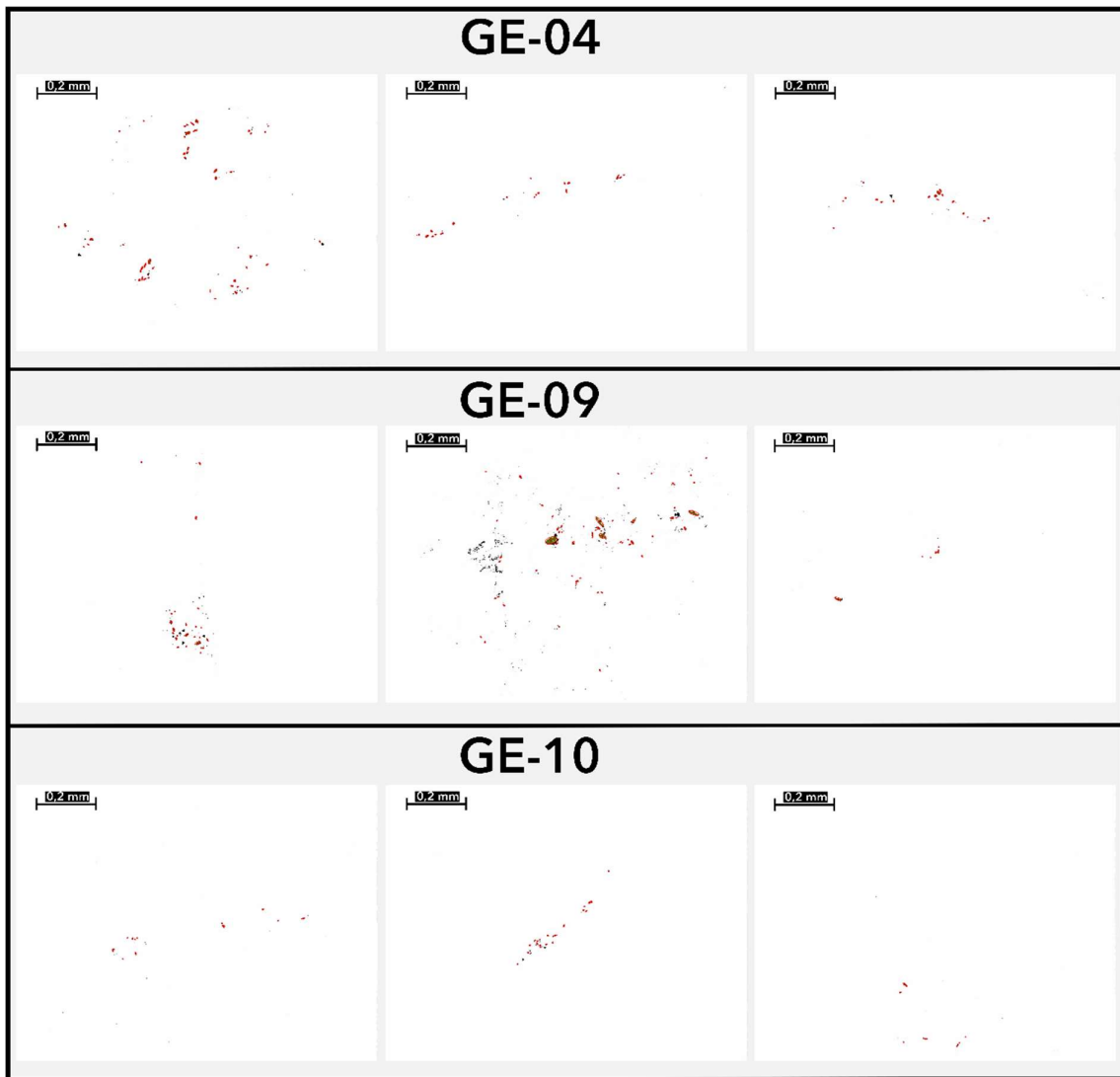


Figure D.2: Binary images of sphalerite grains in oriented photomicrographs of thin sections of samples from the Golden Eagle mine area and prospect site fitted with best-fit ellipses.

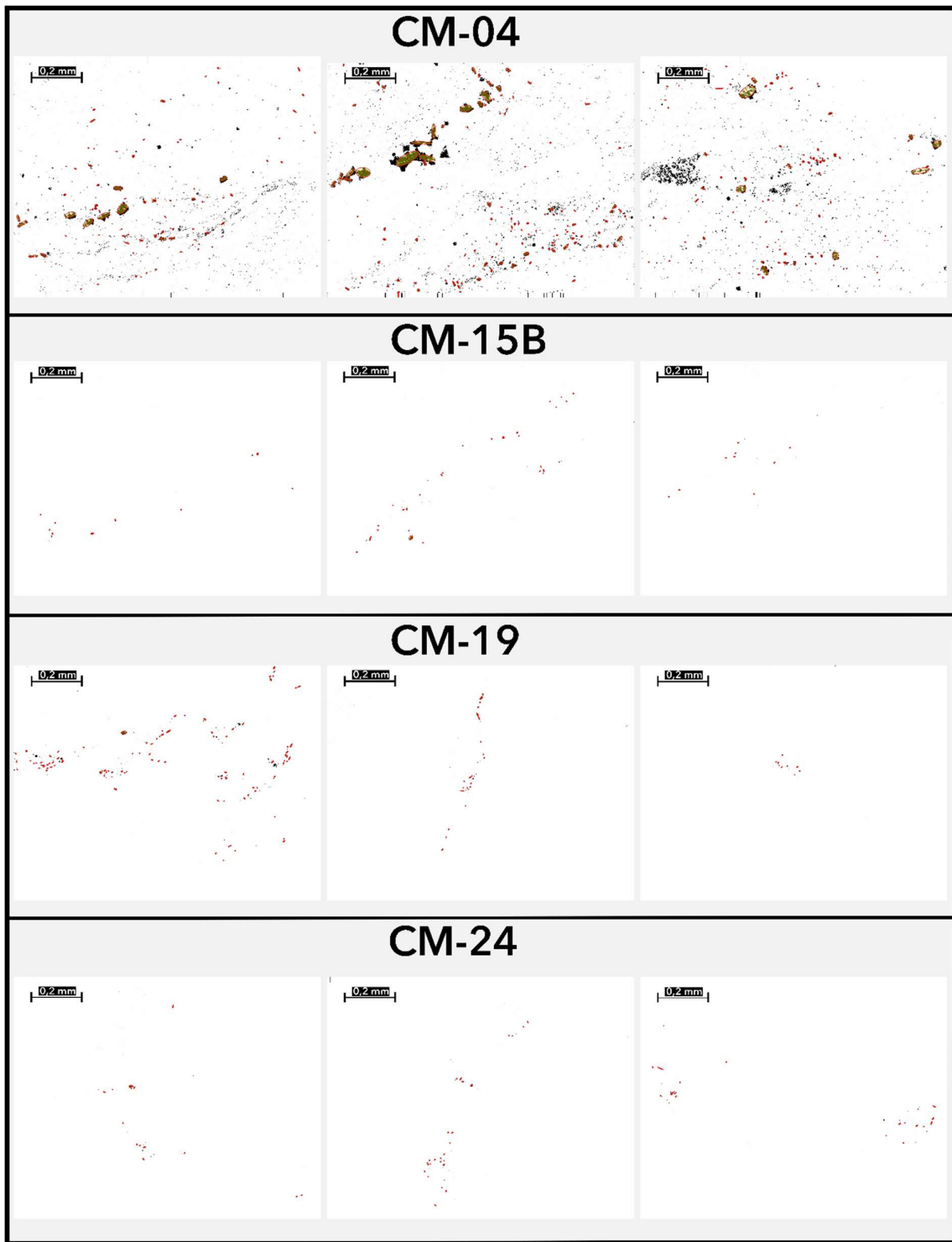


Figure D.3: Binary images of sphalerite grains in oriented photomicrographs of thin sections of samples from the Champion Mine area and prospect site fitted with best-fit ellipses.